Electronic structure of clusters of tetrel elements containing endohedral transition metal ions



Xiao Jin

St Cross College

University of Oxford

A thesis submitted for the degree of

Doctor of Philosophy

September 2018

For my grandmother, Tongqin Cao

Acknowledgements

I would like to express my sincere gratitude to my supervisor, Prof. John E. McGrady, who guided me all the way through my DPhil study. He has always been very supportive and inspiring. Thanks to his patient tutoring and professional insights, the last four years of my research life has been greatly enjoyable.

Words cannot express my gratitude to my parents who supported my study. They brought me to this world, raised me, were my first teachers, and kept being my friends. I admire them greatly for being such compassionate, responsible and open-minded individuals.

I would also like to thank Prof. Jose Goicoechea and his group for all the experimental collaboration works. Last but not least, special thanks to all the McGrady group members in the years of 2014-2018. They have all been kind and helpful, and working with them has been a very pleasant experience.

Abstract

This thesis presents a series of computational investigations into problems relating to the electronic structure of tetrel clusters containing one or more endohedral transition metals. The electronic properties of this class of cluster have been the focus of research for some time, driven in part by the diverse and typically highly symmetric structures that they adopt and also by the desire to miniaturise silicon-based electronic devices. Computational studies are of great importance in this field, particularly for the lighter tetrel clusters where structural information in the form of crystallographic data is entirely absent. Perhaps as a result of the absence of benchmarking data, many controversies have emerged in the literature, with different but apparently equally valid computational methodologies delivering very different conclusions on the structure of specific clusters. Our purpose in this thesis is to provide a deeper understanding of the factors that determine structural preference in this family of clusters, and hence shed some light on the reasons for the disagreements in the literature.

Declaration of Authorship

The work presented in this thesis is the original work of the author, except where references have been made to other sources. No part of this work has previously been submitted for any other degree.

Xiao Jin

Contents

1 Introduction **1**

1.1 Overview 1

1.2 Experimental structural identification 3

1.3 Theoretical studies 10

1.4 Introduction to this DPhil study 23

2 Theory and Methodology **25**

2.1 Wavefunctions and the Schrödinger equation 25

2.2 *Ab initio* methods and related concepts 29

2.2.1 Born-Oppenheimer approximation 29

2.2.2 The Hartree-Fock approximation 31

2.2.3 Correlated Methods 38

2.2.4 Basis sets 55

3 Clusters containing a single transition metal: functional dependency **65**

3.1 Introduction 65

3.2 Computational methods 66

3.3 DFT study of $[M@Si_{14}]^z$ clusters 67

3.3.1 Overview of the potential energy surface 67

3.3.2 Electronic structures of isomer A, B and C 74

3.3.3 Relationship between the two bonding paradigms and possible sources of functional dependency 83

3.4 Post Hartree-Fock calculations 89

3.4.1 CCSD(T) results 89

3.4.2 CASSCF and CASPT2 results 92

3.5 From $[M@Si_{14}]^z$ to other endohedral clusters with a single metal . . . 95

4 Structures of endohedral clusters containing two transition metal atoms 100
4.1 Introduction . . . 100
4.2 Experimental work on the $[Co_2@Ge_{16}]^z$ family . . . 103
4.3 Computational details . . . 104
4.4 Result and discussions . . . 105
4.4.1 Structural identification of the $[Co_2@Ge_{16}]^z$ cluster . . . 105
4.4.2 Electronic structure of the $[Co_2@Ge_{16}]^z$ clusters . . . 107
4.4.3 Extensions to other polymetallic clusters and some thoughts on cluster growth mechanisms . . . 112

5 Electronic structure and electron transport properties of adsorbed WSi_{12} clusters on a Si(111) surface 118
5.1 Introduction . . . 118
5.2 Computational methods . . . 122
5.2.1 Gas-phase studies . . . 122
5.2.2 Surface studies . . . 122
5.2.3 Electron transport properties . . . 122
5.3 Results and discussion . . . 124
5.3.1 Electronic structure of $W@Si_{12}$ . . . 124
5.3.2 Structures of the Si(111) surfaces . . . 125
5.3.3 Structure of the cluster-surface system: WSi_{12} on Si(111) . . . 130
5.3.4 Electron transport pathways in the cluster-surface system: WSi_{12} on Si(111) . . . 137
5.4 Summary . . . 152

Summary 154

References 156

List of Publications 172

List of Figures

1.1 Ground-state structures in the literature; those with blue labels are not confirmed by crystal data 5
1.2 Structural relationship between idealized *closo*, *nido* and *arachno* boranes. Adapted from Rudolph's 1976 paper[60–62] 13
1.3 Theoretical predictions of equilibrium structures for $[M@Ge_{10}]^z$ clusters (top) and $[M@Ge_{12}]^z$ clusters (bottom). The numbers inside the blocks represent the charge number z of the cluster[37, 39, 40, 63–84] . . . 15
1.4 Theoretical predictions of equilibrium structures for $[M@Si_{12}]^z$ clusters (top) and $[M@Si_{16}]^z$ clusters (bottom). The numbers inside the blocks represent the charge number z of the cluster. 'FK' stands for Frank-Kasper polyhedron[5, 9, 44, 46, 48, 49, 51, 77, 78, 88–95, 97–120] 19

3.1 Structures of $M@Si_{14}$ isomers 68
3.2 Relative energies of the neutral $M@Si_{14}$ isomers A to F 69
3.3 Relative energies of isomers A, B and C for the 62-valence-electron $[M@Si_{14}]^z$ clusters 73
3.4 Kohn-Sham orbitals for isomer A of $Cr@Si_{14}$ 77
3.5 Kohn-Sham orbitals for isomer B of $Cr@Si_{14}$ (left), and the isolobal relationship between $Cr@Si_{14}$, *arachno*-$[Si_{14}]^{6-}$ and *closo*-$[Si_{16}]^{2-}$ (right) 79
3.6 Kohn-Sham orbitals for isomer C of $Fe@Si_{14}$ 81
3.7 Schematic representation of the fullerene-like and Wade's rules routes to accommodating electron deficiency in 14-vertex clusters. The numbers below each band indicate the number of orbitals 85
3.8 Schematic Walsh diagram for the $^2B_2$ state of Ag_3 along with sketches for the orbitals $3b_2$ and $3a_1$ 87
3.9 Natural CASSCF(14,15) active space for $^1A_1'$ ground state of $Cr@Si_{14}$ isomer A. Orbitals in the box are included in the (10, 10) active space 92

3.10 Natural CASSCF(14,15) active space for the $^1A_1'$ ground state of $Cr@Si_{14}$ isomer B. Orbitals in the box are included in the (10, 10) active space 94
3.11 Theoretical predictions of equilibrium structures for $[M@Si_{14}]^z$ clusters. The numbers inside the blocks represent the charge number z of the cluster[44, 46–48, 88–99, 101–103, 107, 109–112, 119, 123, 124, 196, 199, 200] . . . 96
3.12 Structures of $Ti@Si_{16}$ isomers considered in this study 99

4.1 A selection of $M_2@Si_n$ structures reported in computational studies . 101
4.2 Schematic pictures of the experimentally characterised $M_2@E_n$ clusters 102
4.3 ESI-MS mass envelope corresponding to $[Co_2@Ge_{16}]^{1-}$ provided in Goicoechea's study[37]: experimental (black trace) and simulated (red) 104
4.4 The lowest lying optimised structures of $[Co_2@Ge_{16}]^z$, z = 0-4 106
4.5 Thermal ellipsoid plot of $[Co_2@Ge_{16}]^{4-}$ at two different sites (drawn at 50% probability level) provided in the study of Sun Zhongming *et al.* 108
4.6 Kohn-Sham diagrams for D_{2h}-symmetric $[Co_2@Ge_{16}]^z$, z = 4, 2, 0 and D_{5h}-symmetric $[Co@Ge_{10}]^{3-}$. The contour plots emphasise the close relation between the mono- and bimetallic structures 109
4.7 Orbitals corresponding to 'lone-pairs' on the bisecting germanium atoms in $[Co_2@Ge_{16}]^{4-}$ 115
4.8 The structures of four rhodium stannides in different sizes and charges 116

5.1 Schematic picture of proposed structures of (a) a $\sqrt{7}$ ring cluster (b) a $\sqrt{19}$ ring cluster and (c) absorbed $CrSi_{12}$. Metal atoms, surface silicon atoms and additional silicon atoms are shown as yellow, light blue and blue balls, respectively 120
5.2 Unit cell settings 123
5.3 Structure of the isolated $W@Si_{12}$ cluster and the Kohn-Sham orbitals 125
5.4 (a)The unreconstructed Si(111) surface, surface reconstruction models due to Haneman (b) and Pandey (c). The energy of the unreconstructed surface is set to zero for the surface systems. Lifted surface Si atoms and atoms forming π bond chains are presented by dark blue balls 127
5.5 7×7 reconstructed Si(111). Different atom layers are presented in different colours. The dashed line encloses the unit cell 129

5.6 Geometries of 7×7 reconstructed Si(111) surface-bound clusters. Adatoms of the surface are highlighted by dark blue balls 132
5.7 Geometries of surface-bound clusters. Structure 1r is taken as the zero of energy for the cluster-surface systems. Cluster Si atoms are in darker blue and the metal atom is in yellow 133
5.8 Schematic picture of surface-absorbed W@Si_{12}. Approximate positions of surface valences are indicated by yellow circles 135
5.9 Kohn-Sham orbitals of the W@Si_{12} cluster and partial density of states of surface-absorbed W@Si_{12} (structure 1h, 1r and 2h) 138
5.10 Optimised geometry of 'hard-landed' clusters 139
5.11 The model of the full device (top) and the relationship between tip-surface distance and total energy of the system (bottom) 140
5.12 Zero-bias transmission spectra of structure 1h using a 'pressed' gold tip (red line), and a 'stretched' gold tip (blue line) 143
5.13 From left to right: Kohn-Sham orbitals of W@Si_{12} cluster, zero-bias transmission spectrum of surface-absorbed W@Si_{12} (structure 1h) and corresponding MPSH eigenstates 145
5.14 Projected device density of states where the projection is made onto all device atoms (left), the cluster plus the surface silicon bonded directly to W atom (middle), and the W atom only (right) 147
5.15 Zero-bias transmission spectra of structure 1h (blue line) and zero-bias transmission spectrum of structure 1r (dark grey line) along with MPSH eigenstates which contribute to the transmission channels of three major peaks 148
5.16 Spatial profile for the transmission spectra of surface models 1h and 1s. The dashed line on the left is a reference line, where the tip is placed far from the cluster 151

Chapter 1

Introduction

1.1 Overview

The miniaturisation of silicon-based electronic devices that has driven the electronics industry for the past 50 years is now approaching a bottleneck because further reduction in the size of a transistor is extremely challenging. Current transistor technology is based on 14 nm gates, which corresponds to the length of a chain of ~70 Si atoms, with reasonable prospects of reducing this to 10 nm in the near future. Below this limit, however, quantum tunnelling is likely to limit the ability of silicon-based materials to function as transistors, although Intel has proposed that a switch to InGaAs may offer opportunities on the sub-10 nm scale. As these silicon components approach the truly molecular scale, chemists have been encouraged to develop a deeper understanding of the fundamental chemistry of the tetrel elements, with the ultimate goal of developing novel materials that could be put into practical use in fabricating smaller transistors. As part of this concerted drive to develop the chemistry of the tetrels, clusters that encapsulate metal atoms/ions have been attracting a great deal of attention from both physicists and chemists, in part because they can be regarded as the simplest models for metal impurities

inside semiconducting materials. The structural chemistry of such clusters may shed light on the 'gettering' process[1] where dispersed metallic impurities inside bulk semiconducting material are released, migrated and captured at purposely-introduced defect sites, ultimately forming islands of metal silicide. Moreover, metal encapsulating tetrel clusters may serve as potential building blocks for nano devices[2], which is another important reason for the field's popularity.

Beck[3, 4] was one of the early pioneers in the field of experimental cluster science, and he was the first to produce metal encapsulating tetrel clusters. He generated gas-phase $M@Si_n$ clusters using a laser vaporised Si wafer and characterised them using Mass Spectrometry (MS). Those early experiments have encouraged other researchers to join the search for stable $M@E_n$ (E = Si-Pb) clusters using similar methods but different reactants[5–18]. In all of these studies, clusters with certain stoichiometries exhibit prominent peaks in MS, indicating that they have exceptional stability in a relative sense. The identification of the structures of these magic clusters and the reasons behind their special stability have been the topic of many papers and recent reviews[19–21] . Experimental work aimed at elucidating structure can be broadly divided into two disciplines: (1) gas-phase spectroscopy and (2) condensed-phase diffraction studies. Whilst X-ray crystallography data is clearly the most informative, crystals have only been isolated for a few anionic clusters of the heavier tetrel species: no silicon-based cluster has yet been characterised in this way. In gas-phase spectroscopic studies, structural information must be inferred by comparison to experimental precedents or to computed properties such as ionisation energies or vibrational frequencies. As a result, a large body of computational work has been reported, either complementing directly the experimental work or with the aim of understanding the nature of the bonding. It is clear from this substantial body of literature that the metal encapsulating tetrel clusters have complex electronic structures, and unfortunately, the results of the

computational analysis are sometimes highly dependent on the chosen methodology. Due to all these difficulties, our understanding of these systems is still rather incomplete, and that lack of understanding provides the motivation for this thesis. In this chapter, I will first present a brief summary of the past findings in this field, both experimental and computational. I will then introduce the key goals of this DPhil work.

1.2 Experimental structural identification

As noted above, the earliest studies in the field were the MS experiments, where a range of $[ME_n]^z$ with different n was generated and detected. The mere observation of a peak in the MS does not, however, provide a precise description of the structure of the cluster and nor does it offer definitive evidence that the metal is encapsulated inside the E_n cluster rather than attached to the surface. In Beck's original study[3, 4], $[MSi_n]^z$ clusters were generated in a supersonic beam from the interaction between vaporised silicon wafer and metal atoms. The formation of clusters was detected using time-of-flight mass spectrometry and the results show that the most abundant stoichiometry, which is later referred to by some researchers as the 'magic number' stoichiometry, is different for clusters with different metals, M. For group VI metal silicon clusters, for example, the most abundant species are MSi_{15} and MSi_{16} while for Cu, $CuSi_{10}$ is the dominant species. Beck's work is extended by many other groups, including Gao[6] who showed that $[CoGe_{10}]^-$ is the dominant species in MS spectra of $[CoGe_n]^-$. Neukermans and Lievens[15] also showed that $[AlPb_{10}]^+$ and $[AlPb_{12}]^+$ are uniquely stable among the $[AlPb_n]^+$ family, and similar patterns have been observed across a wide range of metal and tetrel elements. Hiura *et al*[5] took an alternative approach to the generation of MSi_n clusters by allowing the reaction to happen inside a quadrupole ion trap, us-

ing SiH_4 as reactant instead of Si atoms. Unlike Beck's study, the $[WSi_nH_x]^+$ series of clusters terminated at n = 12 and no larger clusters like WSi_{15} or WSi_{16} were detected. Hiura suggested that it was the higher reactivity of vaporised silicon atoms used in Beck's experiment that resulted in the formation of $M@Si_n$ cluster with a larger n. More importantly, in Hiura's study, not only did the envelope of $[WSi_nH_x]^+$ terminate at n = 12, but when n = 12, the cluster was devoid of hydrogen (x = 0). The interpretation of this observation is that the metal atom in $W@Si_{12}$ is completely encapsulated in the silicon cage, binding to all 12 silicon atoms such that it saturates their valence. The value of n at which the $M@Si_n$ series terminates is also regarded as 'magic' in the sense of the cluster stability, and Hiura's experiments confirmed that this number is also dependent on the choice of central metal. Hiura's experimental data also provoked a discussion on the structure of the 'magic' WSi_{12} cluster. The author's original structural prediction based on DFT calculations was that WSi_{12} adopts a W-encapsulating basket-like C_{2v}-symmetric structure, but a note added in proof identified a more stable hexagonal prismatic D_{6h} structure (Figure 1.1 12D) that will be discussed later, but this did not alter the essential conclusion that the metal atom is fully encapsulated by the cluster. Nakajima[13] proposed a method to examine whether or not the metal atom is encapsulated experimentally based on the fact that a transition metal atom is reactive towards H_2O molecules while pure $[E_n]^z$ clusters are much more inert. Low reactivity toward H_2O can therefore be interpreted as the indicator of a fully encapsulated metal atom. Using water adsorption reactivity as the indicator in this way, Nakajima determined the minimum cage atom number n for fully endohedral encapsulation in $[Tb@Si_n]^-$[13] and $[M@E_n]^z$ (M = group III, IV, V transition metals; z = -1, 0, 1; E = Si, Ge) clusters[8, 10, 12]. The results showed that the threshold number n for $[MGe_n]^{-/0/+}$ is always smaller than that for $[MSi_n]^{-/0/+}$, consistent with the greater size of Ge *vs* Si , In a similar way, Janssens *et al.*[17] used Ar physisorption

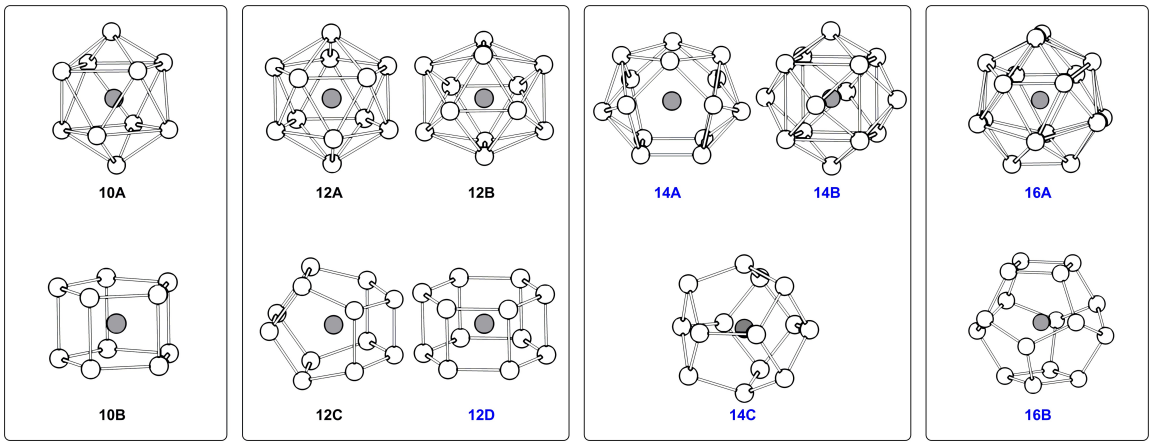


Figure 1.1: Ground-state structures in the literature; those with blue labels are not confirmed by crystal data

as a structural probe to investigate the threshold size of endohedral $[M_m@Si_n]^+$ (M = Ti-Cr, Co, Cu; m = 1,2). These small molecule binding experiments provide circumstantial evidence for the gross structure of the cluster (endohedral or not), and can therefore be viewed as the first step towards structural characterisation. For greater insight, however, we need to turn to diffraction and spectroscopy.

For heavier tetrel element clusters, there has been a concerted effort from a number of groups to synthesise clusters in solution and characterise them by X-ray crystallography. A wide range of anionic $[M@Pb_n]^z$ and $[M@Sn_n]^z$ clusters have been synthesised, and the majority crystallise in perfect or distorted deltahedral shapes. For example, Eichhorn[22, 23] characterised $[M@Pb_{12}]^{2-}$ (M = Ni, Pd, Pt), and showed that all three are icosahedral (Figure 1.1 12A). Later, the $[Ir@Sn_{12}]^{3-}$ and $[Rh@Pb_{12}]^{3-}$ clusters crystallised by Fässler[24] and Xu[25], respectively, were revealed to adopt the same icosahedral structure. The $[Mn@Pb_{12}]^{3-}$ cluster, crystallised by Goichoechea's group[26], is the only known $M@Pb/Sn_{12}$ cluster that is not strictly icosahedral: it adopts a D_{2h}-symmetric structure (Figure 1.1 12B), which can be viewed as a heavily distorted icosahedron compressed/elongated along two orthogonal 2-fold rotation axes of the I_h point group. Smaller endohedral clusters such as the D_{4d}-symmetric bicapped square antiprismatic $[Ni@Pb_{10}]^{2-}$ have

also been synthesized (Figure 1.1 10A)[27]. $[Fe@Sn_{10}]^{3-}$, in contrast, is assigned as a distorted bicapped square antiprismatic cluster[28]. Fässler[29, 30] has also obtained crystal data for a range of M@Pb/Sn_9 clusters including $[Cu@Sn_9]^{3-}$ and $[Cu@Pb_9]^{3-}$, both of which are found to be distorted tricapped trigonal prisms with approximate C_{2v} symmetry. $[Ni@Sn_9]^{4-}$ and $[Co@Sn_9]^{5-}$ clusters, on the other hand, crystallise in two different forms, an almost ideal C_{4v}-symmetric monocapped square antiprism and a tricapped trigonal prism with two of its edges parallel to the 3-fold rotation axis elongated. Moving to systems containing two transition metal atoms, $[M_2E_n]^z$, Eichhorn has reported both $[Ni_2@Sn_{17}]^{4-}$[31] and $[Pt_2@Sn_{17}]^{4-}$[32], while Fässler and Wang have characterised $[Co_2@Sn_{17}]^{5-}$[33] and $[Pd_2@Sn_{18}]^{4-}$[34], respectively. The $[Ni_2@Sn_{17}]^{4-}$ and $[Co_2@Sn_{17}]^{5-}$ clusters share a similar structure, both resembling a fusion of two tricapped trigonal prismatic M@Sn_9 subunits sharing a common vertex, but in $[Pt_2@Sn_{17}]^{4-}$ the two metals are surrounded by a single contiguous ellipsoidal Sn_{17} cage, with no bridging Sn atom. The D_{3d}-symmetric $[Pd_2@Sn_{18}]^{4-}$ cluster is structurally very similar to $[Pt_2@Sn_{17}]^{4-}$, with the cage extended by one Sn atom. A common feature of all the metal encapsulating heavy tetrel clusters mentioned above is that they have Pb/Sn cages with triangular faces, which is a characteristic feature of electron deficient clusters.

There are also a few crystallised lighter tetrel clusters containing endohedral transition metals. Sevov and Goicoechea showed that the $[Pd_2@Ge_{18}]^{4-}$ cluster adopts the same D_{3d}-symmetric structure as $[Pd_2@Sn_{18}]^{4-}$[35]. The same group also showed that the $[Ni_3(Ge_9)_2]^{4-}$ cluster contains a linear trimer of nickel atoms enclosed in two tricapped trigonal prismatic Ge_9 cages[36]. However, the deltahedral architectures of $[Pd_2@Ge_{18}]^{4-}$ and $[Ni_3(Ge_9)_2]^{4-}$ clusters are rather rare in germanium cluster chemistry, and the majority of other examples have more open geometries based on square or pentagonal faces. A particularly interesting example is

the recently characterised $[Co_2@Ge_{16}]^{4-}$ [37, 38], which has been shown to crystallise as a mixture of two distinct isomers. The first, with C_{2h} symmetry, can be viewed as a deltahedral cluster containing two coupled distorted *arachno*-$Co@Ge_{10}$ units. The alternative D_{2h}-symmetric isomer is distinctively different: all of its vertices are 3-connected, and it can be viewed as a fusion of two D_{5h}-symmetric pentagonal prismatic $Co@Ge_{10}$ clusters. In fact, $[Co@Ge_{10}]^{3-}$ is found to adopt precisely such a D_{5h}-symmetric structure (Figure 1.1 10B)[39], as does $[Fe@Ge_{10}]^{3-}$ [40]. Clusters with 3-connected vertices are often described as 'fullerene-like' due to their structural resemblance to fullerenes. Similar 'fullerene-like' structures are also found to be stable for a small number of twelve-vertex species containing Ge, including $[Ru@Ge_{12}]^{3-}$[41], $[V@Ge_8As_4]^{3-}$ and $[Nb@Ge_8As_6]^{3-}$[42], all of which adopt a D_{2d}-symmetric bicapped pentagonal prismatic geometry (Figure 1.1 12C). Here we use quotation marks around the term 'fullerene-like' because the clusters with structural characteristics of fullerene don't always resemble fullerene in their electronic structures. Some of these clusters are much more saturated and should be better named as 'fullerane-like' clusters but right now we will just use the term 'fullerene-like' for brevity. Detailed discussions concerning this issue will be carried out in later sections.

Based on the patterns established in the series Pb → Sn → Ge, we might anticipate that fullerene-like structures would become increasingly dominant over their deltahedral counterparts as we move up to Si. For silicon species, however, there is no crystal data available to confirm this, and structural information must instead be inferred from gas phase spectroscopy. Unlike crystal data, one cannot construct the precise structure directly from these gas phase spectra but it is possible to compare experimental data with computed spectroscopic data for candidate structures and look for a match. For example, in Bowen's photoelectron spectra (PES) study[43], the vertical detachment energy of $[Cr@Si_{12}]^-$ was measured at 3.18 eV,

which matches well with the theoretical value of 3.11 eV calculated by Khanna[44] *et al*. for the D_{6h}-symmetric hexagonal prismatic (Figure 1.1 12D) cluster. This observation therefore supports Hiura's note added in proof where he proposed a similar structure for W@Si_{12}. Lau's X-ray absorption spectrum of $[V@Si_{16}]^+$[45] featured a double peak structure indicating that the cluster has tetrahedral symmetry, confirming the structural prediction made by Kumar *et al.*[46] (Figure 1.1 16A). Nakajima's PES study on $[Ti@E_{16}]^-$ (E = Si, Ge, Sn, Pb) is consistent with the same highly symmetric structure[9]. These three examples represent successful cases of structural determination by comparison to electronic absorption spectroscopy. The vibrational signature of a molecule offers an alternative experimental probe, and the group of Janssens, Lievens and coworkers have pioneered this approach in the context of cluster chemistry. For example, in their infrared multiple photon dissociation (IR-MPD) spectroscopy experiment on $[Mn@Si_n]^+$[47] and $[V@Si_n]^+$[48] systems, resonant absorption of photons by the cluster results in local heating and evaporation of weakly bound Xe atoms. The IR-MPD depletion spectra are then constructed by recording the ion intensities of the cluster-xenon complexes as a function of photon energy using the Free Electron Laser for Infared eXperiments (FELIX) facility. IR absorption spectra can then be reconstructed from the depletion spectra and compared with theoretical predictions. Although for many systems the match between the experimental IR and the theoretical model is not conclusive, the most likely candidate structures have been proposed in many cases. As an example of the information content of these experiments, the authors proposed that $[V@Si_{16}]^+$ is very likely to be fluxional as a result of the rapid interchange of atomic positions between a T and a T_d-symmetric deltahedral geometry proposed by Kumar[46, 49].

Kanayama's group have taken a different approach to characterisation clusters by depositing them on surfaces. For example, the X-ray absorption fine structure

(XAFS) and X-ray absorption near-edge structure (XANES) spectra of WSi_n films showed that the film contains WSi_n (n = 8 or 12) cluster units, among which the twelve-vertex species should be endohedral[50]. Moreover, the calculated XANES spectra for hexagonal prismatic $W@Si_{12}$ cluster, with W-Si distances of 2.58 Å, is a convincing match for the experimental XANES spectra. In a separate study, $[TaSi_{10-13}H_x]^+$ clusters were synthesised and deposited onto Si(111)-(7×7) surfaces and scanning tunnelling microscopy was used to reveal the structure of the deposited clusters[51]. The clusters appear as bright dots on the silicon surface, and a comparison of the measured cluster heights with calculated cluster diameters, allowed the author to infer that the clusters preserved their Ta-encapsulating structures on the surface. A further interesting feature of this experiment is that a small fraction of the clusters exhibited a 'double stripe' shape in the STM image, which the authors interpreted as $[TaSi_{12}H_x]^+$ and $[TaSi_{13}H_x]^+$ clusters (both have a hexagonal prismatic base) that had landed onto the surface with a rectangular face rather than a hexagonal face. This experimental data, and its interpretation, provides the motivation for the work described in Chapter 5.

In summary, although no crystal data is available for the metal encapsulating silicon clusters, spectroscopic measurements appear to confirm the existence of a fullerene-like D_{6h}-symmetric hexagonal prismatic structure for group VI transition metals (Cr, Mo, W). In contrast, a highly symmetric deltahedral structure has been identified for early transition metals encapsulated in a Si_{16} cage. Thus, just like for the germanium cluster family, both 'fullerene-like' structures and deltahedron structures are found for the silicon cluster family.

1.3 Theoretical studies

The previous paragraphs have highlighted the point that the structures of different metal encapsulating tetrel element clusters are very diverse. Deltahedra dominate the structural landscape for $M@Sn_n$ and $M@Pb_n$ clusters while all the crystallised $M@Ge_n$ clusters are 'fullerene-like' in the sense that they have 3-connected vertices and pentagonal faces. As for silicon clusters, the lack of crystal data leads to a more open debate on what the structures are, and the origins of the stability of specific geometries have been explored in many theoretical studies. Perhaps the most important point to emerge from the papers reviewed in this section is that there is no single bonding model that can account for all known $M@E_n$ clusters: depending on the degree of mixing of metal- and cage-based orbitals, a spectrum of different bond types emerges.

There is some evidence to support the idea that the stability of the late transition metal encapsulating Sn/Pb clusters owes as much to the intrinsic stability of the empty Sn/Pb clusters themselves as it does to any subtle aspects of the metal-cluster interaction. On the most superficial level, the encapsulation of a late transition metal changes the structure of $[Sn/Pb_{10}]^{2-}$ and $[Sn/Pb_{12}]^{2-}$ cluster to a negligible extent. In Eichhorn's studies[22, 23], $[Pd@Pb_{12}]^{2-}$ and $[Pt@Pb_{12}]^{2-}$ have very similar structures: both clusters are nearly perfectly I_h symmetric (Figure 1.1 12A), and the bond lengths are almost identical to those in $[Pb_{12}]^{2-}$ according to Eichhorn's DFT calculation. Furthermore, the calculated metric parameters of the empty $[Pb_{10}]^{2-}$ ion from DFT are very close to the calculated and experimentally observed Pb-Pb distances in $[Ni@Pb_{10}]^{2-}$, which adopts a bicapped square anitprismatic structure (Figure 1.1 10A)[27]. The crystal structure for the *closo* $[Pb_{10}]^{2-}$ from Fässler[52] also matches almost perfectly with Eichhorn's prediction. Although neither has been crystallographically characterised, Wang and

coworkers[53, 54] provided PES spectra to show that both $[Pb_{12}]^{2-}$ and $[Sn_{12}]^{2-}$ exist and are icosahedral, while $[Sn_{12}]^{-}$ and $[Pb_{12}]^{-}$ are C_{5v} symmetric due to Jahn-Teller distortions. Wang and coworkers also examined the PES of a series of $[M@Sn_{12}]^{-}$[55] with different central metals and suggested that both $[Cu@Sn_{12}]^{-}$ and $[Au@Sn_{12}]^{-}$ are icosahedral. A few years later, $[Ir@Sn_{12}]^{3-}$ and $[Rh@Pb_{12}]^{3-}$, which are isolobal with $[Pd@Pb_{12}]^{2-}$, $[Pt@Pb_{12}]^{-}$, $[Cu@Sn_{12}]^{-}$ and $[Au@Sn_{12}]^{-}$ were crystallised by Fässler[24] and Xu[25], respectively. Both are almost perfectly I_h symmetric. Nguyen's CCSD(T) calculations on $[Cu/Ag/Au@Sn_{10}]^{-}$ and $Zn@Sn_{12}$ clusters [56, 57] confirmed that the D_{4d}-symmetric structure found for $[Pb_{10}]^{2-}$ is the most stable structure for $[Cu/Ag/Au@Sn_{10}]^{-}$, and the icosahedral structure for $[Pb_{12}]^{2-}$ is the ground-state structure of $Zn@Sn_{12}$. All of the work mentioned above seems to be consistent with the idea that a specific valence electron count is associated with the special stability of $[M@Pb/Sn_n]^z$ (n = 10, 12), and that this stability can be traced back to the stability of $[Pb/Sn_n]^{2-}$ (n = 10, 12). On this matter, several different electron counting models have been proposed. Nguyen in their CCSD(T) papers mentioned that $Zn@Sn_{12}$ satisfies the close electronic shell model (which has electrons that fill exactly $1S^2 1P^6 1D^{10} 1F^6 2S^2 1F^8 2P^6 1G^{10}$ orbitals), and is therefore exceptionally stable[57]. $Zn@Sn_{12}$ and $M@E_{10}$ also satisfy Hirsch's $2(N+1)^2$ π electron counting rule (N being zero or any positive integer number), according to which their π shells are filled so that they exhibit spherical aromaticity. Lievens *et al.*[14] support the idea of cage aromaticity based on calculated nucleus-independent chemical shifts (NICS) for $[E_n]^{2-}$ and $M@E_n$ (E = Si-Pb, n = 5-12). They showed that $[E_{10}]^{2-}$ (E= Si-Pb) and $[E_{12}]^{2-}$ (E= Sn, Pb) clusters all have negative NICS values, at the centres of the cages, a traditional indicator of aromaticity. Another perspective on electron counting, mentioned by Eichhorn[22], refers to Teo's proposal for icosahedral clusters[58]: the number of $[Pt@Pb_{12}]^{2-}$ cluster's skeletal electron pairs is 18, which suggests that this cluster is a typical

electron-rich icosahedral cluster. Last but not least, the $M@E_{10}$ and $M@E_{12}$ (E= Sn,Pb) clusters obey a more general and widely accepted skeletal electron counting rule, Wade's rules. The 4n+2 total valence electron count (n being the number of vertices), is precisely that required for a *closo* architecture. The high stability of the 4n+2 *closo* count also leads to remarkably low oxidation states: Fässler's natural charge calculation on $[Ir@Sn_{12}]^{3-}$, for example, led to its formulation as $Ir^{-}@Sn_{12}^{2-}$[24]. Schafer's magnetic response data[18] and Jena's DFT calculation[59] also suggest that $Mn@Sn_{12}$ should be $Mn^{2+}@Sn_{12}^{2-}$. It seems that the researchers are in consensus on the number of valence electron count on $E_{10/12}$ (E = Sn, Pb) cage. What is less clear is the role of the central metal. In the late transition metal encapsulating clusters mentioned above, the central metal seems to be of little or no importance in structural determination, other than providing the cage with one or two electrons from its valence n*s* shell to helps the cage reach its favoured *closo* electron count electron count. However, the distorted structures of $[Mn@Pb_{12}]^{3-}$ and $[Fe@Sn_{10}]^{3-}$, determined by Goicoechea and coworkers[26, 28] suggest a rather more important role for the metal *d* electrons for all $[M@Pb/Sn_n]^z$ clusters. Moving gradually left towards the center of the periodic table, metal *d* orbitals become higher in energy and the metal *d* component in the frontier orbitals increases. The partial occupation of these *d* orbitals then drives significant distortions from perfect *closo* structures when the 4n+2 electron count is not met. Through DFT calculations, Goicoechea and McGrady showed that the highest lying occupied orbital (HOMO) of the I_h-symmetric $[Ni@Pb_{12}]^{2-}$ is an h_g orbital which has a dominant contribution from the Pb 6*p* orbitals[26]. An I_h-symmetric $[Mn@Pb_{12}]^{3-}$ ion would have a partially filled h_g orbital with a dominant Mn 3*d* character, with the unpaired electrons localized largely on the Mn center rather than over the 12 cage Pb atoms. The small HOMO-LUMO gap provides the driving force for a significant distortion. The $[Fe@Sn_{10}]^{3-}$ cluster presents a similar case, in which case

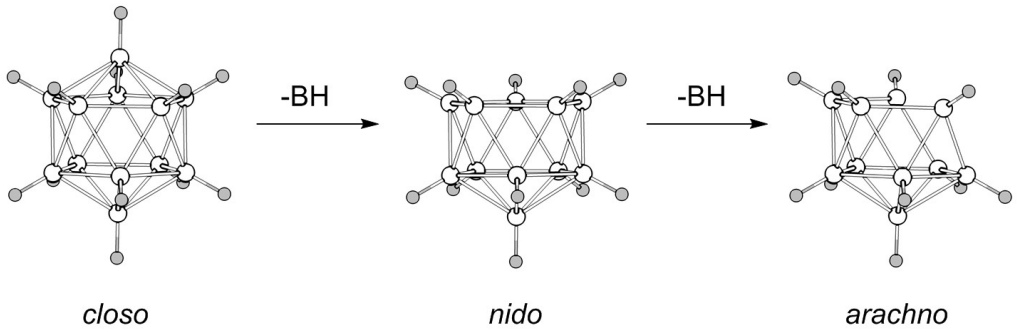


Figure 1.2: Structural relationship between idealized *closo*, *nido* and *arachno* boranes. Adapted from Rudolph's 1976 paper[60–62]

the partially-filled metal *d* orbitals are high enough in energy to become the main contributors to the frontier orbitals, driving the distortion away from the high-symmetry limit. In these circumstances, the metal *d* electrons certainly cannot be considered inert − they play a defining role in the determination of the cluster's structure.

The number of computational studies on metal encapsulating germanium clusters far exceeds the number of computational studies on the heavier tetrel analogues described above. This is perhaps because it was not until 2009 that the first $M@Ge_n$ cluster was characterised using single crystal X-ray diffraction, and before that point computational studies were the major source of structural information. Quite a few groups have explored growth patterns in $M@Ge_n$ clusters[63–75], covering a wide range of different transition metals and stoichiometries. By plotting the averaged binding energy, embedding energy, HOMO-LUMO gap and other indicators of stability against the cluster size, these studies shed light on various problems, including the determination of threshold size and 'magic' stoichiometry. More importantly, the potential energy surface was explored thoroughly and a number of stable isomers were identified for different $M@Ge_n$ clusters. Among these structures, there are deltahedral structures, *e.g.* the same I_h-symmetric structure found for $[E_{12}]^{2-}$ (E = Sn, Pb)[75], and some more open cage structures with

3-connected vertices. (including a distorted pentagonal prismatic structure for $Au@Ge_{10}$[67], a distorted hexagonal prismatic structure for $W@Ge_{12}$[63] and a D_{2d} bicapped pentagonal prismatic structure for $Ni@Ge_{12}$[64]) As we have mentioned in previous sections, deltahedral structures appear to be relatively disfavoured for $M@Ge_n$ clusters, and all the $M@Ge_n$ clusters that have been characterised since 2009 belong to the so-called fullerene-like family. To understand the reasons for this, the electronic structure of the $M@Ge_{10}$ and $M@Ge_{12}$ groups has been explored in depth. In Figure 1.3, the ground-state structures of $[M@Ge_{10}]^z$ and $[M@Ge_{12}]^z$ clusters, that have been predicted by a number of different groups, are summarised. Different structures are indicated by different colours, and the numbers inside the blocks represent the charge number z of the cluster. If the charge number is in red, then the corresponding cluster with that charge number has a highly symmetric structure (no distortion). If no number is present inside a given block, then the only studied cluster is the neutral cluster. Within the block, if different colours are applied (for clusters with the same charge number z), the $[M@Ge_n]^z$ cluster has been studied by multiple groups and conflicting claims, for the equilibrium structure have been made. For example, the manganese box in the $[M@Ge_{10}]^z$ figure is coloured half green and half orange, and there is not any number written in the box. This means there are controversies on the ground-state structure of $Mn@Ge_{10}$: some authors found it to be a deltahedral (either D_{4d}, C_{3v} symmetric or distorted slightly from these two symmetries) while others found a ground-state structure that is neither deltahedral, nor 3-connected D_{5h} symmetric.

The range of colours in Figures 1.3 reflects the complexity of the structural landscape. As shown in the figure, the D_{5h} structure (Figure 1.1 10B) for $[M@Ge_{10}]^z$ and the D_{2d} structure (Figure 1.1 12C) for $[M@Ge_{12}]^z$, both of which are observed in experiments, are relatively more prevalent for electron rich species, where the sum of the valence electron count on the metal atom and the negative charge is close to



Figure 1.3: Theoretical predictions of equilibrium structures for $[M@Ge_{10}]^z$ clusters (top) and $[M@Ge_{12}]^z$ clusters (bottom). The numbers inside the blocks represent the charge number z of the cluster[37, 39, 40, 63–84]

10, but also where the metal *d* electrons are not too contracted. Despite the common 'fullerene-like' cluster title, these two structures seem to be quite different from the D_{6h} structure (Figure 1.1 12D), which is stabilised at the left hand side of the periodic table for $[M@Ge_{12}]^z$. In his paper focusing on the characterisation of $[Co@Ge_{10}]^{3-}$, Fässler[39] described the Ge_{10} cage as an analogue to pentaprismane $C_{10}H_{10}$. Similarly, Goicoechea[40] compared the $[Fe@Ge_{10}]^{3-}$ cluster to $[SnR]_5$ (R = 2,6-$Et_2C_6H_3$), an electron precise 'three-connected' cluster which conforms to the 5n rule, according to which the number of valence electrons on each vertex atom is five, three of which contribute to 2-centre-2-electron bonds with adjacent cage atoms and the other two constitute a lone pair at each vertex. Furthermore, Goicoechea and McGrady[41] showed in their study of the $[Ru@Ge_{12}]^{3-}$ cluster that in the D_{2d}-symmetric cluster, all metal *d* electrons are involved in bonding. Together with 3 external charges and 48 valence electrons from the Ge cage, there are 59 valence electrons in total compared to a 5n count of 60. The one electron missing from the 5n electron count (n is the number of vertices), the so called single 'hole', is localised in an orbital with $2a_2$ symmetry, which is an orbital localised entirely on the cage. Goicoechea and McGrady's symmetry analysis[77] showed that the n lone pair orbitals and 3n/2 bonding orbitals of a D_{2d}-symmetric $M@Ge_{12}$ cluster span an orbital set of $6a_1 + 2a_2 + 3b_1 + 5b_2 + 7e$, precisely the symmetries of the filled orbitals in 60-electron $[Rh@Ge_{12}]^{3-}$. In the same paper, the authors noted that the D_{2d} structure would distort to a S_4-symmetric structure and then further to a C_2-symmetric structure through rotating one of E_6 unit within the E_{12} cluster (the E_{12} cluster can be regarded as two E_6 units being perpendicular to each other, sandwiching one metal atom) relative to the other about a common conserved C_2 axis, going from 59-electron $[Ru@Ge_{12}]^{3-}$ to 58-electron $Pd@Ge_{12}$, then 57-electron $Co@Ge_{12}$. The driving force of this distortion is an increase in effectiveness of shared electron density between the metal and the cage. The limit of the distortion

is a 90° rotation of one of the E_6 units relative to the other, which leads to the D_{6h} hexagonal prismatic structure. The authors also showed that the hexagonal prismatic structure favours 54-56 electron counts, but did not address the origin of the stability of the related D_{6d} hexagonal antiprismatic structure that dominates the structural landscape on the far left. As for the deltahedra, although so far there are no reports of crystallised clusters of this type, theoretical studies shows that they are still of relatively high stability, especially for the late transition metal encapsulating clusters with small charges. Again, the stability of these endohedral cluster may simply reflect the intrinsic stability of empty germanium cages: King[85, 86] reported that the D_{4d}-symmetric *closo* structure is the global minimum for $[Ge_{10}]^{2-}$ while the I_h *closo* structure, albeit not being the global minimum for $[Ge_{12}]^{2-}$, lies only 5.6 kcal/mol above the global minimum, which is a C_{2v}–symmetric structure with concave faces. Very recently, $[Ge_{10}]^{2-}$ was confirmed to adopt the predicted D_{4d}-symmetric geometry by Fässler and co-workers[87], who synthesised the cluster in solution phase and obtained its crystal structure. However, the deltahedral structures are relatively less stable for germanium clusters comparing to tin or lead, due to the differences in the elements' nature. King[86] has argued that the icosahedral structure of $[Ge_{12}]^{2-}$ is relatively disfavoured because germanium is more prone to sp mixing comparing to tin and lead. The lone pair electrons in tin or lead clusters have dominant s character, and the large s-p separation means that they remain perfectly inert, just like the B-H bonding electrons in boranes. On the other hand, in germanium clusters, partial depopulation of the external lone pairs can lead to the formation of π bonds around the surface of the cage, 'particularly in concavities or even at high degree vertices of relatively low curvature' as King stated. This indicates that the deltahedra actually become less stable relative to fullerene-like isomers even when the E_n cage is empty. Another possible factor that would tip the balance of this structural competition towards a more 'open'

structure for $[M@Ge_n]^z$ clusters is simply size: King[79] noted that open structures, like the hexagonal prism, are more capable of accommodating large central metal atoms. For tin and lead, the cage is large enough no matter the structure it adopts, while for germanium, it is possible that only the open structures can accommodate large metal atoms. It is difficult to quantify how important this size factor is, but it is indisputable that while the deltahedra are reported to be the most stable structures for many first row transition metal $[M@Ge_{10/12}]^z$ clusters, $Hf@Ge_{10}$ is the only cluster of a third row element that has been claimed to favour a deltahedral structure .

Although $M@Si_n$ clusters were the first of the $M@E_n$ family to be studied experimentally, the absence of crystallographic data still hinders progress in this field. The wealth of gas-phase data has, however, motivated a very large number of computational studies. As was the case for the germanium clusters, many computational studies have focused on the growth patterns of the $[M@Si_n]^z$ clusters and the identification of 'magic' stabilities[78, 88–103]. Together with work focusing on one specific stoichiometry or structure, these more wide-ranging studies have built up a structural prediction landscape for the $[M@Si_n]^z$ cluster family. In Figure 1.4, we summarise the results of computational studies relating to the $[M@Si_{12/16}]^z$ families.

The pattern of the predicted structural landscape of $[M@Si_{12}]^z$ clusters bears some resemblance to that of $[M@Ge_{12}]^z$, with the major difference that the I_h-symmetric structure is never competitive enough to become the ground-state structure. The destabilisation of deltahedral structures is apparent for $[M@Si_{10}]^z$ clusters as well, where the pentagonal prismatic cage is stable for the majority of the mid to late transition metals[91, 94, 95, 97, 103, 111, 115], and no stable D_{4d} deltahedral structure was reported for any metal. This is not surprising if we see the structural landscape of Si as a continuation from heavier tetrel $[M@E_n]^z$ clusters: on

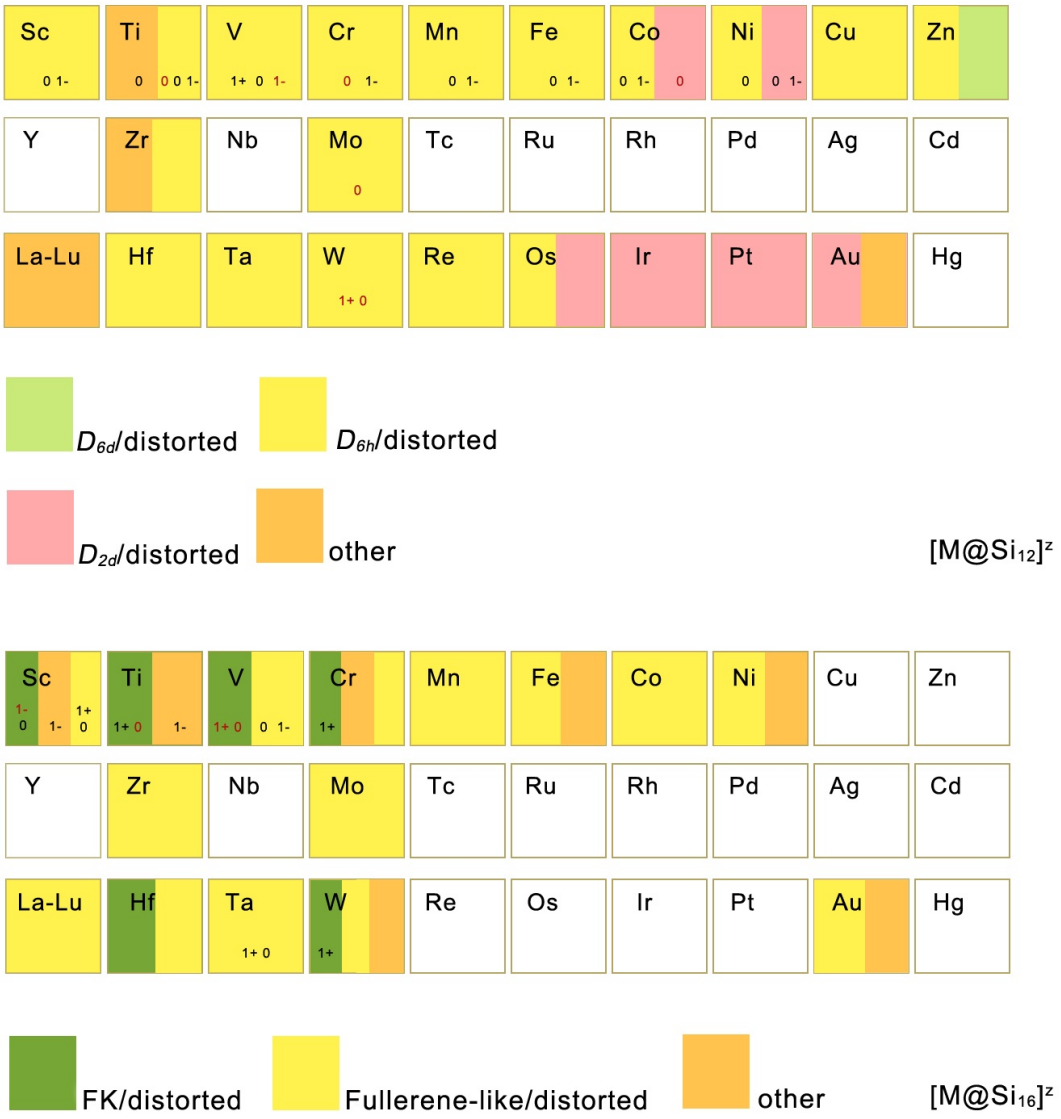


Figure 1.4: Theoretical predictions of equilibrium structures for $[M@Si_{12}]^z$ clusters (top) and $[M@Si_{16}]^z$ clusters (bottom). The numbers inside the blocks represent the charge number z of the cluster. 'FK' stands for Frank-Kasper polyhedron[5, 9, 44, 46, 48, 49, 51, 77, 78, 88–95, 97–120]

one hand, sp mixing in Si becomes yet more significant so that the tendency to form cage π bonds becomes stronger, and on the other hand, Si_n clusters are smaller. If the increasing capability of sp mixing and size effect are the reasons for fullerene-like structures to be stabilized over deltahedron-like structures in the case of metal encapsulating germanium clusters, the same arguments should hold true for the silicon clusters as well. The hexagonal prismatic structure first proposed by Hiura[5] dominates the structural landscape for M@Si_{12}, and despite the absence of a crystal structure, the combination of PES and infra-red spectroscopic experiments note previously offers compelling evidence that this is indeed the case. The reason for its stability has, however, been controversial. In the original report of Hiura, the author suggested that the stability could be rationalised in term of an 18-electron rule: each silicon atom donates one electron to the metal, so that together with the 6 d electrons from itself, the central metal has 18 valence electrons. In this model, three valence electrons are left on each cage silicon atom, and they each participate in the formation of one cage Si-Si bond. If this is the case, however, all four valence electrons at Si would be oriented inwards towards the cage centre, which should be a rather unstable situation. The Jellium model has also been applied to this M@Si_{12} system in attempt to explain the clusters' special stability: Khanna suggested that within the Jellium framework, 18-electron $1s^2 1p^6 1d^{10}$ and 20-electron $1s^2 1p^6 1d^{10} 2s^2$ configurations can account for the high dissociation energies of hexagonal prismatic Cr@Si_{12} and Fe@Si_{12}[104]. Molecular orbital analysis, however, offers a more refined picture. In a later study by Khanna[110], the authors showed that the metal d_{z^2} orbital is in fact unoccupied in the hexagonal prismatic Cr@Si_{12} and because no silicon atom is aligned along the principal (6-fold) axis, the crystal field-like splitting of the d orbitals resembles the splitting in a square-planar environment and the central metal is therefore stable with 16 valence electrons.

For the M@Si_{16} clusters, a fullerene-like open structure with D_{4d} symmetry (Figure 1.1 16B) has been assigned as the ground-state structure for a wide range of metals, but interestingly, a stable deltahedral structure has been identified for very early transition metal encapsulating species. The most stable structure for $[Sc@Si_{16}]^-$, Ti@Si_{16}, and $[V@Si_{16}]^+$ is calculated to be a compact Frank-Kasper (FK) structure with T_d (or T, if distorted) symmetry (Figure 1.1 16A) by many researchers[9, 46, 48, 49, 105–109]. In almost all of these studies, the FK structure is reported to have an exceptionally large HOMO-LUMO gap which is typically taken as an indicator of stability. Furthermore, as we have mentioned in an earlier paragraph, Lau's experimental X-ray absorption data[45] shows that $[V@Si_{16}]^+$ has tetrahedral symmetry, thus confirming the theoretical prediction. Based on the high connectivity of the vertices, one might want to draw analogies between the FK structure and the deltahedral structures found for Sn/Pb clusters and also for late transition metal encapsulating germanium clusters. This must, however, be done with caution because in the Ti@Si_{16} cluster, unlike in deltahedral $[M@Ge_n]^z$ clusters' scenario, the *d* orbitals of the central metal participate in cage bonding. The Ti atom provides four valence electrons, and so Ti@Si_{16} would have a total valence electron count of 68 = 4n +4, two more than anticipated for a typical *closo* structure according to Wade's rules. A 4n + 4 count is usually associated with a *nido* geometry, seemingly inconsistent with the very high tetrahedral symmetry. This deviation could be rationalised if we look into the detailed classification of the deltahedral clusters made by Johnston and Mingos[121]. According to their analysis the FK structured M@E_{16} clusters should belong to the C_3 Polar deltahedra, which usually have n or n+2 skeletal electron pairs instead of n+1. The jellium model also offers a few possible explanations for the special stability of the FK structure. According to Khanna[105], the the FK cluster can be viewed as 'a silicon cage encapsulating a nearly free electron gas'. Each silicon atom that bonds to the

metal contributes one electron, while the central metal contributes all of its *d* electrons to the electron gas, as a result of which the $Ti@Si_{16}$ cluster free electron count is 20, a stable configuration within the jellium construct. Kumar[122] also pointed out that the 68 electrons would fill exactly up to the 2*d* shell of a spherical polyhedron. Palagin[108], who studied $[Ti/V/CrSi_{16}]^+$ argued that the special stability is not restricted to clusters with exactly 68 valence electrons, but also extends to near-spherical polyhedral with a valence-electron count close to 68. The jellium model can also be related to the idea of 'spherical aromaticity'. Lau[45] showed that for $[V@Si_{16}]^+$, which is isovalent with $Ti@Si_{16}$, the total valence electron count is 68, where 18 electrons are in π states, and 50 electrons are in σ states. Both π states and σ states follow the $2(N+1)^2$ rule of spherical aromaticity therefore by this definition the cluster is aromatic. The NICS value calculated by Chen and Lievens[14] for the FK structured $[Si_{16}]^{4-}$ cage is negative, which strengthens the argument that the FK $[Si_{16}]^{4-}$ cage is aromatic. However, in the same study, it was shown that the D_{4d} symmetry fullerene-like structured $[Si_{16}]^{4-}$ cage also has a negative NICS value.

The problem of having several competing structures of similar energy is compounded in the $[M@Si_{14}]^z$ family. In Hiura's original paper, the $[Hf@Si_{14}H_x]^+$ clusters were the upper limit[5], suggesting that 14 is a 'magic number' at least for Hf encapsulating clusters. Subsequent work on the $M@Si_{14}$ family has raised a large number of controversies, and the results often depend critically on the chosen computational methodology. The contradictions are captured by the story of the group VI and group VIII transition metal clusters, where two structures prove to have similar stabilities. For group VI metals, the first structure is a C_{2v}-symmetric *arachno-* like cluster (Figure 1.1 14A) proposed as the equilibrium structure of $Cr@Si_{14}$ by Kumar and Kawazoe[102, 123] using the PW91 functional, and also by Khanna[88, 110] using PBE. The other is a D_{3h}-symmetric fullerene-like struc-

ture (Figure 1.1 14C) first predicted by Hiura from a topological[119] point of view, and later supported by He's calculation[124] using B3LYP. While the fullerene-like D_{3h}-symmetric structure is still one of the most stable structures for Fe@Si_{14}, as calculated by Mpourmpakis *et al*.[111] and He[124] using B3LYP, the C_{2v}-symmetric *arachno*- structure is no longer a preferred structure. Instead, a spherically arranged O_h-symmetric structure (Figure 1.1 14B) was proposed by Kumar and Kawazoe[46] using the PW91 functional, and later reproduced by Wang[99] and Khanna[112] using PBE. It appears that the B3LYP functional always favors the fullerene-like structure over the structures with more deltahedron characters. The origin of these patterns and the search for a unifying model for the structure of the M@Si_{14} family is the subject of Chapter 3.

1.4 Introduction to this DPhil study

This DPhil study aims to deepen our understanding of the electronic structure of small metal-encapsulating tetrel clusters. Chapter 2 prepares us with the basic knowledge of computational methods applied in this study. In Chapter 3, I will report the results of our investigation on the $[M@Si_{14}]^z$ clusters. The functional dependency issue found in the literature has inspired us to look deeply into this series of clusters, the ultimate goal being to establish why one functional favors one type of structure over another. Along the way, we establish the quite different patterns of bonding in these different isomers and show that the 'fullerene-like' and the 'deltahedral type' clusters can actually be related through the 'electron precise' structure. In fact, they are two solutions to the same problem of dealing with electron deficiency, and they happen to be of almost equal stability for metal encapsulating silicon clusters. In Chapter 4, I will be presenting the results of a collaborative project with Professor Goicoechea's group in Oxford on $[Co_2@Ge_{16}]^z$

clusters. The aim here is to explore the electronic structure of $[M_2@E_n]^z$ clusters and compare them to the $[M@E_n]^z$ precursors. This part of the DPhil study expands our knowledge to larger metal encapsulating clusters and, hopefully, will shed some light on the topic of cluster growth. The last chapter focuses on surface deposited $M@Si_n$ clusters. Our work is inspired by Kanayama's STM study of $TaSi_n$ clusters deposited on Si(111) surface. We used DFT calculations to explore how the structure of cluster is affected by its deposition on a silicon surface, and also how the deposition of such cluster might affect the surface reconstruction process. In addition, an STM simulation will be presented to show how our DFT can help interpreting STM results.

As mentioned at the very beginning of this chapter, metal encapsulating tetrel clusters can be regarded as the simplest models for metal impurities inside bulk semiconducting materials. During the gettering process, where metal ions diffuse through and eventually are removed from silicon wafers, the metal atom could encounter different environments that resemble the $M@E_n$ clusters, their bimetallic analogues or even clusters with more metal centres. Thus, the importance of expanding our knowledge of isolated single metal encapsulating clusters and their behaviour on surfaces is not merely of academic interest, but may also inform work focusing on the gettering process. We hope, ultimately, this DPhil work may inspire the search for innovative materials for semiconducting material-based devices and become a small stepping stone to the improvement of the performance of semiconducting material based devices.

Chapter 2

Theory and Methodology

In this chapter, basic concepts of quantum chemistry[125] and a brief introduction on the computational methods[126–128] employed in this thesis are given. We first look at the wavefunction description of the quantum state of particles, to gain a better understanding of the subjects of quantum chemistry in general. Then we show how the calculations are carried out in practice using different methods, and what approximations are made that we should be aware of. This chapter not only sets up a foundation for my entire DPhil study, it also provides some necessary technical details we will come back to in later chapters, when making sense of our computational results.

2.1 Wavefunctions and the Schrödinger equation

The motion of a classical mechanical particle can be described by a function $\vec{r}(t)$ which gives the particle's changing position in time. In quantum mechanics, however, the position of a particle is not well-defined unless the particle is undergoing an observation or measurement of its position. The seemingly peculiar behaviour of a quantum mechanical particle can still be described by one function, the wavefunction, $\Psi(t)$. This function is a complex valued distribution evolving over time

and is called a wavefunction because it is the solution to an equation that has the mathematical form of a wave-equation. Wavefunctions are most frequently seen in the form $\Psi(\mathbf{r}, t)$, which is a function of the particle's coordinates in position space. Born's statistical interpretation of the function is that for a normalised one particle wavefunction $\Psi(\mathbf{r}, t)$, $\Psi^*(\mathbf{r}, t)\Psi(\mathbf{r}, t)\mathrm{d}^3\mathbf{r}$ gives the probability of finding the particle in the infinitesimal volume $\mathrm{d}^3\mathbf{r}$ at position $\mathbf{r}$ at time t. In other words, if a particle is described by a normalised wavefunction Ψ, $|\Psi|^2$ is the probability density of finding the particle at a certain time. Following this interpretation, physical meaningful particle states should be normalisable vectors (or functions) in Hilbert space, L2. It is worth noting that a wavefunction Ψ can also be represented in forms other than $\Psi(\mathbf{r}, t)$, for example, through its Fourier transform into momentum space. The corresponding $\Psi(\mathbf{p}, t)$ is a different representation of the wavefunction that encodes the same physical information.

The wavefunction described in the previous paragraphs shows a spatial dependence. However, elementary particles in quantum mechanics also possess an intrinsic angular momentum, typically named 'spin', which resembles spin angular momentum in classical mechanics. It is independent of the particle's motion in space and cannot be decomposed into extrinsic angular momenta of constituent particles. The observable 'spin' of an elementary particle in quantum mechanics is fundamentally different from spin angular momentum in classical mechanics despite the name. It is quantised, being either integer (bosons) or half-integer (fermions). The existence of 'spin' was first demonstrated by the Stern-Gerlach experiment, and was incorporated into nonrelativistic theory by the *ad hoc* inclusion of a spin function to the final form of wavefunction. Spin quantisation subsequently emerged as a natural consequence of the inclusion of relativity in quantum mechanics, and this leads naturally to the 'Pauli exclusion principle' which states that the total wavefunction of a system of fermions should be antisymmetric with

respect to the exchange of two identical particles.

In quantum mechanics, each observable Q can be associated with a Hermitian operator $\widehat{Q}$ that acts on the wavefunction. If, and only if, the wavefunction is an eigenfunction of the operator, a measurement of the observable Q on the system is certain to return one value λ, the corresponding eigenvalue of the eigenfunction. Mathematically, the above measurement could be written in an integration form: assuming $\widehat{Q}$ is a time-independent operator, the measurement of observable Q on system $\varphi(\mathbf{r},t)$, returning value λ, can be written as:

$$\frac{\int_{-\infty}^{+\infty} \mathrm{d}^3\mathbf{r}\, \varphi^*(\mathbf{r},t)\widehat{Q}\varphi(\mathbf{r},t)}{\int_{-\infty}^{+\infty} \mathrm{d}^3\mathbf{r}\, \varphi^*(\mathbf{r},t)\varphi(\mathbf{r},t)} = \lambda$$

The equation above is also quite often presented in its bra-ket (or Dirac) notation:

$$\frac{\langle\varphi|\widehat{Q}|\varphi\rangle}{\langle\varphi|\varphi\rangle} = \lambda$$

where the wavefunction is in its vector form and the operator in its matrix form. The eigenvectors (or eigenfunctions) of operator $\widehat{Q}$ constitute a complete set and can be chosen to be orthogonal. When $\varphi(\mathbf{r},t)$ is not an eigenfunction of $\widehat{Q}$, the expectation value $\frac{\int_{-\infty}^{+\infty} \mathrm{d}^3\mathbf{r}\, \varphi^*(\mathbf{r},t)\widehat{Q}\varphi(\mathbf{r},t)}{\int_{-\infty}^{+\infty} \mathrm{d}^3\mathbf{r}\, \varphi^*(\mathbf{r},t)\varphi(\mathbf{r},t)}$ gives a average value of the observable. Taking a normalised wavefunction $\Phi(\mathbf{r},t)$ as an example, one can construct an arbitrary wavefunction $\Phi(\mathbf{r},t)$ using a linear combination of the eigenfunctions of $\widehat{Q}$: $\Phi(\mathbf{r},t) = c_1\phi_1 + c_2\phi_2 + c_3\phi_3 \ldots$ The measurement Q then has the probability c_1^2 returning λ_1, c_2^2 returning λ_2, c_3^2 returning λ_3 *etc*, λ_1, λ_2, λ_3 being the corresponding eigenvalues for eigenfunctions ϕ_1, ϕ_2, ϕ_3. $\lambda = c_1^2\lambda_1 + c_2^2\lambda_2 + c_3^2\lambda_3 \ldots$

In classical mechanics, Newton's laws of motion relate the motion of a particle to the total force the particle is subjected to. Given the position of a particle at a particular time, $\vec{r}(0)$, and the total force, $\vec{F}(\mathbf{r},t)$, Newton's law of motion gives $\vec{r}(t)$ of the particle at anytime. The analogue of Newton's law of motion in quantum

mechanics is the Schrödinger equation[129]. Albeit in a form quite different, the Schrödinger equation predicts the value of the wavefunction $\Psi(\mathbf{r},t)$ at any time if the wavefunction at a particular time, $\Psi(\mathbf{r},0)$, and the potential, $V(\mathbf{r},t)$, is known. The Schrödinger equation is a first order differential equation in time, with a rather simple form:

$$i\hbar\frac{\partial\Psi(\mathbf{r},t)}{\partial t} = [-\frac{\hbar^2}{2m}\nabla^2 + V(\mathbf{r},t)]\Psi(\mathbf{r},t)$$

where $-\frac{\hbar^2}{2m}\nabla^2$ is the non-relativistic kinetic operator. The sum of kinetic and potential energy operators, $[-\frac{\hbar^2}{2m}\nabla^2 + V(\mathbf{r},t)]$ is known as the Hamiltonian operator $\widehat{H}$. When the potential V is time independent, $\widehat{H}$ is also time independent, in which case, the first order differential equation can be separated into time and spatial components.

$$\Psi(\mathbf{r},t) = e^{-iEt/\hbar}\,\psi(\mathbf{r})$$

The solution $\Psi(\mathbf{r},t)$ is a product function of a time dependent, space independent part, $e^{-iEt/\hbar}$, and a space dependent, time independent part, $\psi(\mathbf{r})$. $\Psi(\mathbf{r},t)$ is a called a stationary state of energy E, $E \in \mathbb{R}$. It is 'stationary' in the sense that its probability density $|\Psi^2(\mathbf{r},t)|$ does not change in time. Factoring out the time dependent part when substituting $\Psi(\mathbf{r},t) = e^{-iEt/\hbar}\,\psi(\mathbf{r})$ back into the time-dependent Schrödinger equation leads to:

$$\big[-\frac{\hbar^2}{2m}\nabla^2 + V(\mathbf{r})\big]\psi(\mathbf{r}) = E\psi(\mathbf{r})$$

This second order differential equation in space provides complete information on the particle spatial distribution $\psi(\mathbf{r})$. The solutions for ψ are eigenfunctions of operator $\widehat{H}$, each corresponds to an eigenvalue E. The eigenfunctions are called the energy eigenstates. The smallest eigenvalue, E_0, and its corresponding eigenstate(s) ψ_0 are called the ground-state energy and ground state(s), respectively.

A very important theorem in quantum chemistry is the variation principle,

which states that the expectation value of the Hamiltonian of any normalised particle wavefunction, $\Phi(\mathbf{r}, t)$, is an upper bound to the exact ground-state energy, E_0.

$$\langle \Phi(\mathbf{r}, t) | \widehat{H} | \Phi(\mathbf{r}, t) \rangle \geq E_0$$

The identity holds only when $\Phi(\mathbf{r}, t)$ is identical to the ground state ψ_0. Thus the best approximation to the ground-state wavefunction is that which delivers the lowest energy.

2.2 *Ab initio* methods and related concepts

2.2.1 Born-Oppenheimer approximation

The primary objective of quantum chemistry is to deduce the electronic structures of atomic and molecular systems. This necessarily involves finding solutions to the time independent Schrödinger equation for systems containing nuclei and electrons. Within self-contained systems, nuclei and electrons evolve in the electronic field created by each other, and so quantum chemistry seeks solutions of conserved systems with correlated particles. The complete Hamiltonian for such a system is given by the following expression:

$$\begin{aligned} \widehat{H}_{\mathrm{e}} &= \widehat{T}_{\mathrm{e}} + \widehat{T}_{\mathrm{n}} + \widehat{V}_{\mathrm{ne}} + \widehat{V}_{\mathrm{ee}} + \widehat{V}_{\mathrm{nn}} \\ &= -\sum_{i=1}^{N} \frac{1}{2} \nabla_i^2 - \sum_{A=1}^{M} \frac{1}{2} \nabla_A^2 - \sum_{i=1}^{N} \sum_{A=1}^{M} \frac{Z_A}{r_{iA}} + \sum_{i=1}^{N} \sum_{j>i}^{N} \frac{1}{r_{ij}} + \sum_{A=1}^{M} \sum_{B>A}^{M} \frac{Z_A Z_B}{R_{AB}} \end{aligned}$$

where $-\sum_{i=1}^{N} \frac{1}{2} \nabla_i^2$ and $-\sum_{A=1}^{M} \frac{1}{2} \nabla_A^2$ are the kinetic energies of electrons and nuclei, respectively, and $\sum_{i=1}^{N} \sum_{j>i}^{N} \frac{1}{r_{ij}}$ and $\sum_{A=1}^{M} \sum_{B>A}^{M} \frac{Z_A Z_B}{R_{AB}}$ are the corresponding repulsions between electrons and between nuclei. The final term, $-\sum_{i=1}^{N} \sum_{A=1}^{M} \frac{Z_A}{r_{iA}}$, represents the coulomb attraction between electrons and nuclei. Unfortunately, ex-

act solutions to the Schrödinger equation for systems of 3 or more correlated particles are not available, and so we seek instead approximate solutions of increasingly complexity.

The first approximation introduced by quantum chemists is typically the Born-Oppenheimer (BO) approximation. The idea is that because the mass of nuclei is at least 1.8×10^3 greater than the mass of electrons, the electrons move much more rapidly than the nuclei. As a consequence the position of the nuclei can be considered as 'fixed' when solving the electronic Schrödinger equation. Essentially, the BO approximation decouples the movement of electrons with nuclei. In terms of the total Hamiltonian shown above, the BO approximation amounts to setting the kinetic energy of the nuclei ($\widehat{T}_{\mathrm{n}}$) to zero, and the nucleus-nucleus repulsion can be treated as a parameter that depends only on the distance, R_{AB}. The BO approximation therefore breaks down the problem of solving the wavefunction of a system where the motion of every particle is coupled into a two-step problem, where the first step is solving the electronic structure with moving electrons and fixed nuclei (the electronic Schrödinger equation):

$$\widehat{H}_{\mathrm{e}}\Psi_{\mathrm{e}}(\mathbf{r};\mathbf{R}) = E_{\mathrm{e}}(\mathbf{R})\Psi_{\mathrm{e}}(\mathbf{r};\mathbf{R})$$

$$\widehat{H}_{\mathrm{e}} = \widehat{T}_{\mathrm{e}} + \widehat{V}_{\mathrm{ne}} + \widehat{V}_{\mathrm{ee}} = -\sum_{i=1}^{N}\frac{1}{2}\nabla_i^2 - \sum_{i=1}^{N}\sum_{A=1}^{M}\frac{Z_A}{r_{iA}} + \sum_{i=1}^{N}\sum_{j>i}^{N}\frac{1}{r_{ij}}$$

and the second step is considering the motion of nuclei in the average field created by electrons. The electronic Schrödinger equation is given by $\Psi_{\mathrm{e}}(\mathbf{r};\mathbf{R})$ in the equation above. $\mathbf{R}$, the positions of the nuclei, is a fixed parameter. The electronic Hamiltonian $\widehat{H}_{\mathrm{e}}$ consists of three terms, all three acting only on electrons. The total energy of the fixed nuclei system is recovered by adding in a term the nuclear-

nuclear repulsion term:

$$E_{\text{tot}}(\mathbf{R}) = E_{\text{e}}(\mathbf{R}) + \sum_{A=1}^{M} \sum_{B>A}^{M} \frac{Z_A Z_B}{R_{AB}}$$

Repeatedly calculating $E_{\text{e}}(\mathbf{R})$ using $\widehat{H}_{\text{e}}\Psi_{\text{e}}(\mathbf{r};\mathbf{R}) = E_{\text{e}}(\mathbf{R})\Psi_{\text{e}}(\mathbf{r};\mathbf{R})$ when provided with a new set of nuclear position $\mathbf{R}$, and plotting $E_{\text{tot}}(\mathbf{R})$ against nuclei positions gives the so called potential energy surface (PES).

2.2.2 The Hartree-Fock approximation

Having decoupled the electrons from the nuclei, we next need to 'decouple' electrons from each other, at least to some extent, to generate multi-electron wavefunctions. Hartree[130] introduced the idea of treating electrons as independent particles, moving in the average electric field created by other electrons. Fock[131] extended Hartree's ideas by considering the Pauli Exclusion Principle, which demands that the wavefunction be antisymmetric with respect to exchange of any two identical particles. The method to which both contributed greatly is now widely known as the Hartree-Fock (HF) method.

The essence of the HF method is to construct the total electron wavefunction using a set of single electron wavefunctions as a way to reduce the N-electron electron wavefunction to a product of N 1-electron wavefunctions. One assumes that each electron occupy a 1-electron wavefunction (a molecular or atomic orbital). The single electron wavefunction χ_i is expressed as a product of spatial and spin components,

$$\chi_i = \psi_i(\mathbf{r})\alpha(\omega) \text{ or } \psi_i(\mathbf{r})\beta(\omega)$$

$\alpha(\omega)$ and $\beta(\omega)$ are both eigenfunctions of the operator $\widehat{S}_z$, corresponding to eigenvalues $\frac{\hbar}{2}$ and $-\frac{\hbar}{2}$ respectively. Then the total electron wavefunction is then constructed using a set of orthonomal spin-orbitals as a Slater determinant, which

ensures adherence to the Pauli Exclusion Principle. For a system with N electrons:

$$\Psi_{\text{etot}} = |\chi_a(1)\chi_b(2)\dots\chi_k(N)\rangle = \frac{1}{\sqrt{N!}}\begin{vmatrix} \chi_a(1) & \chi_b(1) & \cdots & \chi_k(1) \\ \chi_a(2) & \chi_b(2) & \cdots & \chi_k(2) \\ \vdots & \vdots & \ddots & \vdots \\ \chi_a(N) & \chi_b(N) & \cdots & \chi_k(N) \end{vmatrix}$$

The expression depicts a state where the electrons occupy single electron spin orbitals $\chi_a, \chi_b, \dots, \chi_k$, where $\langle\chi_i|\chi_j\rangle = \delta_{ij}$. The time independent Schrödinger equation for the HF method is then:

$$\widehat{H}_{\text{e}}\Psi_{\text{etot}} = \widehat{H}_{\text{e}}|\chi_a(1)\chi_b(2)\dots\chi_k(N)\rangle = E_{\text{etot}}\Psi_{\text{etot}}$$

From now on we drop the subscript e for the sake of brevity. As noted previously, the variation principle tells us that the expectation value of the Hamiltonian acting on a trial wavefunction will always be greater than or equal to the ground-state energy, so the best approximation to the true ground state is the determinant that delivers the lowest expectation value of the energy. Under the HF approximation, we arrive at the HF energy ground state by minimizing $E_{\text{tot}} = \langle\Psi_{\text{tot}}|\mathbf{H}|\Psi_{\text{tot}}\rangle$ subject to the constraint restriction $\langle\chi_i|\chi_j\rangle = \delta_{ij}$. Using Lagrange's method of undetermined multipliers, and doing unitary transformation between the single-electron spin orbitals themselves, we can show that this problem is equivalent to obtaining the eigenfunctions of the Fock operater where

$$\widehat{f}(1)\chi_i(1) = \varepsilon_i\chi_i(1)$$

$$\widehat{f}(1) = \widehat{h}(1) + \sum_{j=1}^{N}\widehat{J}_j(1) - \widehat{K}_j(1)$$

$$\widehat{h}(1) = -\frac{1}{2}\nabla_1^2 - \sum_A \frac{Z_A}{r_{1A}}$$

$$\widehat{J}_j(1)\chi_i(1) = \Big[\int \mathrm{d}\vec{r}_2\, \chi_j^*(2)\frac{1}{r_{12}}\chi_j(2)\Big]\chi_i(1)$$

$$\widehat{K}_j(1)\chi_i(1) = \Big[\int \mathrm{d}\vec{r}_2\, \chi_j^*(2)\frac{1}{r_{12}}\chi_i(2)\Big]\chi_j(1)$$

For an N-electron system, the N eigenfunctions with lowest eigenvalues would be the 'filled molecular orbitals' that construct ground state Ψ_0 while the remainder would be considered 'unoccupied orbitals' or 'virtual orbitals'. The total energy can be expressed as

$$E_{\text{tot}} = \langle \Psi_{\text{tot}} | \mathbf{H} | \Psi_{\text{tot}} \rangle = \sum_{i=a}^{k} \langle \chi_i | \mathbf{h} | \chi_i \rangle + \sum_{i=a}^{k}\sum_{j=a}^{k} [\chi_i\chi_i|\chi_j\chi_j] - [\chi_i\chi_j|\chi_j\chi_i]$$

The first term is the summation of one-electron terms which contain 1-electron kinetic terms ($\widehat{T}_e$) and 1-electron attractions toward the nuclei ($\widehat{V}_{\text{ne}}$). The second term is the sum of so called Coulomb and Exchange terms,

$$\begin{aligned}[\chi_i\chi_i|\chi_j\chi_j] &= \int \mathrm{d}\vec{r}_1\mathrm{d}\vec{r}_2\mathrm{d}\omega_1\mathrm{d}\omega_2\chi_i^*(1)\chi_i(1)\frac{1}{r_{12}}\chi_j^*(2)\chi_j(2) \\ &= \langle \chi_i(1)|\mathbf{J}_j(1)|\chi_i(1)\rangle\end{aligned}$$

$$\begin{aligned}[\chi_i\chi_j|\chi_j\chi_i] &= \int \mathrm{d}\vec{r}_1\mathrm{d}\vec{r}_2\mathrm{d}\omega_1\mathrm{d}\omega_2\chi_i^*(1)\chi_j(1)\frac{1}{r_{12}}\chi_j^*(2)\chi_i(2) \\ &= \langle \chi_i(1)|\mathbf{K}_j(1)|\chi_i(1)\rangle\end{aligned}$$

which together reflect the electron-electron potential under the HF approximation.

In practice, to solve the eigenfunction problem for the Fock operator, a set of known orbital functions is introduced as basis to construct the molecular orbitals $\{\chi_i\}$, whose coefficients can be varied to yield the lowest energy. The idea of using a basis set was first introduced by Roothaan[132] and we will further discuss the topic of different types of basis in common use in a later section. For now we

regard the basis a set of predetermined functions that can be used to describe the molecular orbitals well enough. Consider the case where we use restricted spin orbitals $\chi_i(\mathbf{x}) = \begin{cases} \psi_r(\mathbf{r})\alpha(\omega) \\ \psi_r(\mathbf{r})\beta(\omega) \end{cases}$ where a pair of spin up and spin down electrons always share the same spatial function. We could simplify the Fock eigenfunction problem by integrating over spin to solving the spatial integral-differential equation $\widehat{f}_s(1)\psi_i(1) = \varepsilon_i\psi_i(1)$ where

$$\widehat{f}_s(1) = \widehat{h}(1) + \sum_{j=1}^{N/2} 2\widehat{J}_{sj}(1) - \widehat{K}_{sj}(1)$$

$$|\mathbf{J}_{sj}(1)|\psi_i(1)\rangle = \Big[\int \mathrm{d}\vec{r}_2\, \chi_j^*(2)\frac{1}{r_{12}}\chi_j(2)\Big]\psi_i(1)$$

$$|\mathbf{K}_{sj}(1)|\psi_i(1)\rangle = \Big[\int \mathrm{d}\vec{r}_2\, \chi_j^*(2)\frac{1}{r_{12}}\chi_i(2)\Big]\psi_j(1)$$

As the set of known basis functions $\{\phi_\nu(\vec{r})|\nu = 1, 2, \ldots, K\}$ expand the spatial molecular orbitals $\{\psi_i\}$:

$$\psi_i = \sum_{\nu=1}^{k} C_{\nu i}\phi_\nu$$

the equation to solve becomes:

$$\widehat{f}_s(1)\sum_{\nu=1}^{k} C_{\nu i}\phi_\nu(1) = \varepsilon_i \sum_{\nu=1}^{k} C_{\nu i}\phi_\nu(1)$$

Left multiplying the equation above by $\phi_\mu^*(1)$ and integrating generates a matrix equation which can be written in the compact form:

$$\mathbf{FC} = \mathbf{SC}\varepsilon$$

F is the Fock matrix with elements

$$\begin{aligned} F_{\mu\nu} &= \int \mathrm{d}\vec{r}_1\, \phi_\mu^*(1)\widehat{f}(1)\phi_\nu(1) \\ &= \int \mathrm{d}\vec{r}_1\, \phi_\mu^*(1)\widehat{h}(1)\phi_\nu(1) + \sum_{j=1}^{N/2} \int \mathrm{d}\vec{r}_1\, \phi_\mu^*(1)[2\widehat{J}_{sj}(1) - \widehat{K}_{sj}(1)]\phi_\nu(1) \\ &= \int \mathrm{d}\vec{r}_1\, \phi_\mu^*(1)\widehat{h}(1)\phi_\nu(1) + \sum_{j=1}^{N/2} \sum_{\lambda\sigma} C_{\lambda j} C_{\sigma j}^* [2(\mu\nu|\sigma\lambda) - (\mu\lambda|\sigma\nu)] \end{aligned}$$

$(\mu\nu|\sigma\lambda)$ and $(\mu\lambda|\sigma\nu)$ have the same form as $[ij|kl]$ only instead of being integrals of spin orbitals $\chi_i, \chi_j, \chi_k, \chi_l$ they are integrals of spatial orbitals. Noticing that the electron density $\rho(\mathbf{r}) = 2\sum_i^{N/2} |\psi_i(\mathbf{r})|^2 = \sum_{\mu\nu} \left[2\sum_{i=1}^{N/2} C_{\mu j} C_{\nu j}^*\right] \phi_\mu(\mathbf{r}) \phi_\nu^*(\mathbf{r})$, we can define a density matrix **P** with elements $P_{\lambda\sigma} = 2\sum_j^{N/2} C_{\lambda j} C_{\sigma j}^*$, such that $F_{\mu\nu}$ can be written as $\int \mathrm{d}\vec{r}_1\, \phi_\mu^*(1)\widehat{h}(1)\phi_\nu(1) + \sum_{\lambda\sigma} P_{\lambda\sigma}[(\mu\nu|\sigma\lambda) - \frac{1}{2}(\mu\lambda|\sigma\nu)]$. Splitting **F** into 1- and 2-electron terms, we get two matrices $\mathbf{H}^{core}$ and **G**. **S** is is the overlap matrix with elements

$$S_{\mu\nu} = \int \mathrm{d}\vec{r}_1\, \phi_\mu^*(1)\phi_\nu(1)$$

C is the square matrix of the coefficients $C_{\mu i}$, μ and i both range from 1 to K. Its i^{th} column describes the molecular orbital ψ_i. ε is a diagonal matrix where $\varepsilon_{\mu\nu} = \varepsilon_i$ when $\mu = \nu$ and 0 elsewhere. Because **G**, and therefore **F**, depends on **C** through $P_{\lambda\sigma}$ in the above equation, the equation $\mathbf{FC} = \mathbf{SC}\varepsilon$ can only be solved iteratively. The self-consistent field (SCF) method, the most commonly used technique, is summarised below.

1. Specify the system: obtain a set of nuclei coordinates $\{R_A\}$, a set of atomic numbers $\{Z_A\}$ for the nuclei and the number of electrons N. Specify the basis set to use for the calculation $\{\phi_\mu\}$.

2. Calculate **S**, $\mathbf{H}^{\mathbf{core}}$ and all two electron integrals $(\mu\nu\,|\,\sigma\lambda)$.

3. Guess a density matrix **P**

4. Use **P** and all the $(\mu\nu \mid \sigma\lambda)$ to construct **G**. Construct **F** using **G** and $\mathbf{H}^{\mathbf{core}}$.

5. Diagonalise **F** to obtain **C** and ε.

6. Form a new **P** from **C**.

7. Compare new **P** with **P**, if their difference is within the preset criteria call the calculation converged and exit the cycle, if not use the new **P** and enter step 5 to continue the calculation.

In cases where an unrestricted set of spin orbitals is used, spatial orbitals of electrons with different spins are described differently, and treated separately when calculating **G**. Ultimately we need to calculate two sets of eigenvalue problems

$$\mathbf{F}^{\alpha}\mathbf{C}^{\alpha} = \mathbf{S}\mathbf{C}^{\alpha}\varepsilon^{\alpha}$$
$$\mathbf{F}^{\beta}\mathbf{C}^{\beta} = \mathbf{S}\mathbf{C}^{\beta}\varepsilon^{\beta}$$

The unrestricted HF ansatz frees the electrons from the restriction of having to share some same spatial orbitals so that it allows electrons to avoid each other more effectively, and produces a system ground state with lower energy than the restricted ground state for open-shell systems. The problem with the unrestricted HF method is that, unlike restricted HF, the unrestricted HF solutions are neither eigenstates of the squared spin operator $\widehat{S}^2$ nor can they be spin adapted. This is problematic because the exact eigenfunctions of the Hamiltonian under a nonrelativistic treatment should be eigenfunctions of $\widehat{S}^2$ because this operator commutes with the Hamiltonian. Nevertheless, they are used extensively in the treatment of open-shell systems. The energy calculated by the HF method using an infinitely large basis set is called the 'Hartree-Fock limit', which must, through the variation principle, be greater than or equal to the system's true electron ground-state energy.

While from a mathematical point of view it is clear that inaccuracy rises in HF approximation because the exact Hamiltonian is forced to act on an approximate wavefunction, physically it is not immediately obvious what is lacking in the single determinant wavefunction. Noting that the single determinant wavefunctions we solve are true eigenfunctions of a set of single electron operators $\widehat{f}$, we can see the key assumption is that electrons can be treated as particles that moves in an average field created by other particles. In other words, the electrons lack 'correlation' with each other. Conventionally, the energy difference between a system's true ground-state energy and the system's HF limit is named 'correlation energy'. The HF limit is not always a useful reference point (in DFT, for example), and so in practice, the term 'correlation' is often used in a qualitative sense to describe the extent to which electrons avoid each other above and beyond the mean-field approximation. We have stated earlier that for some systems the unrestricted HF solution has a lower energy ground state than the restricted alternative, in such cases the difference between a system's true ground-state energy and its restricted HF limit includes not only the error induced by 'average field approximation' but also the error induced by adding extra restriction on spin orbitals. Nevertheless it is not very meaningful to talk about the two error sources separately as mathematically both contributes to the inaccuracy in the description of the total wavefunction. From now on we follow this convention of naming the difference between energy obtained using exact wavefunction and energy obtained using a HF single determinant (restricted or not) the 'correlation energy' and do not alternate to distinguish the exact physical meaning behind the name unless necessary. With this clarified we could end this section with a brief comment on the effect of lack of 'correlation' in Hartree-Fock. As we can see in Hartree-Fock approximation the electrons are not completely decoupled: as long as the determinant is anti-symmetric, the electrons with same spin component cannot occupy the same spatial orbital

and thus in effect 'avoid' each other. For electrons with different spin components, however, the Pauli principle does not help directly, and the electrons 'avoid' each other only due to the effect of classical Coulomb repulsion, this is where HF does not handle well enough. Under HF approximation, due to the lack of 'correlation' the electrons are closer to each other than they should be in reality. This can be demonstrated by calculations on the distribution function and mean value of the interelectronic separation $f(r_{12})$ and $\langle r_{12} \rangle$ for simple electronic systems. An example is given by Coulson and Neilson[133] where they defined the size of the 'Coulomb hole' in ground-state helium atom (two electrons having opposite spin). Not only is the $\langle r_{12} \rangle$ of a HF (restricted) determinant smaller than $\langle r_{12} \rangle$ of any other wavefunctions with different amounts of correlation, but also, the distribution curve $f(r_{12})$ of a HF determinant shifts towards the region of a larger r_{12} as a whole.

2.2.3 Correlated Methods

Configuration Interaction (CI)

Although electron correlation, as defined in the previous section, is typically small in an absolute sense compared to the HF energy, changes in correlation energy often account for a large part of the differences in energy in a reaction. Moreover, an explicit treatment of electron correlation can be essential for even a qualitative description of some systems, such as biradicals. The most straightforward approach to include electron correlation is to use a better wavefunction than the HF approximation (a single Slater determinant). Mathematically we can see that any arbitrary antisymmetric wavefunction of N variables can be exactly expanded in terms of all unique determinants $|\chi_1 \chi_2 \ldots \chi_N\rangle$ formed from a complete set of 1-electron wavefunctions $\{\chi_i\}$ Assuming that we have a complete set of basis function to con-

struct a complete set of 1-electron spin orbitals $\{\chi_i\}$, the HF method gives us one N variable determinant $|\chi_1\chi_2\ldots\chi_N\rangle$ as ground state for an N electron system and a set of unoccupied spin orbitals $\{\chi_{N+1}, \chi_{N+2}, \ldots\}$. We can then define a unique set of determinants by exchanging one or more of the occupied spin orbitals of the HF ground-state determinant $|\chi_1\chi_2\ldots\chi_N\rangle$ with unoccupied spin orbitals from $\{\chi_{N+1}, \chi_{N+2}, \ldots\}$. Each of these excited determinants is also antisymmetric with respect to electron exchange, so we can expand any arbitrary N electron wavefunction $|\Phi\rangle$ in terms of the HF ground-state determinant and all its single excitation, double excitation…N-tuple excitation states:

$$|\Phi\rangle = c_0|\Psi_0\rangle + \sum_S c_S\tau_S|\Psi_0\rangle + \sum_D c_D\tau_D|\Psi_0\rangle + \sum_T c_T\tau_T|\Psi_0\rangle + \ldots + \sum_N c_N\tau_N|\Psi_0\rangle$$

τ is the excitation operator in second quantisation. The HF method described above is simply the limit where all coefficients other than c_0 are zero. Though the equation above terminates with the N-electron excited terms, the arbitrary wavefunction is indeed expanded into infinite number of terms, for the number of unoccupied orbitals is infinite given an infinite basis set. Each of the terms denotes a specific electron configuration, thus the expansion process is called 'configuration interaction' (CI). By applying the linear variational method, we can get the true ground state with the best set of coefficients $\{c\}$. This reduces to the problem of finding the eigenvalues of the matrix $\langle\Phi|\mathbf{H}|\Phi\rangle$ which can be expanded in a

Hermitian block matrix form (only the upper triangle is shown):

$$\begin{bmatrix} \langle \Psi_0|\mathbf{H}|\Psi_0\rangle & 0 & \langle \Psi_0|\mathbf{H}|\mathrm{D}\rangle & 0 & 0 & \cdots \\ & \langle \mathrm{S}|\mathbf{H}|\mathrm{S}\rangle & \langle \mathrm{S}|\mathbf{H}|\mathrm{D}\rangle & \langle \mathrm{S}|\mathbf{H}|\mathrm{T}\rangle & 0 & \cdots \\ & & \langle \mathrm{D}|\mathbf{H}|\mathrm{D}\rangle & \langle \mathrm{D}|\mathbf{H}|\mathrm{T}\rangle & 0 & \cdots \\ & & & \langle \mathrm{T}|\mathbf{H}|\mathrm{T}\rangle & \langle \mathrm{T}|\mathbf{H}|\mathrm{Q}\rangle & \cdots \\ & & & & \langle \mathrm{Q}|\mathbf{H}|\mathrm{Q}\rangle & \cdots \\ & & & & & \ddots \end{bmatrix}$$

$|S\rangle$, $|D\rangle$, $|T\rangle$, $|Q\rangle$ are simplifications for singly, doubly, triply and quadruply excited states. Note that all matrix elements of the Hamiltonian between two determinants which differ by 3 or more spin orbitals are zero because the Hamiltonian contains only 1-electron and 2-electron operators. Also the block $\langle \Psi_0|\mathbf{H}|S\rangle$ has only zero elements due to Brillouin's theorem which states that the HF ground state does not mix directly with single excitations. This matrix is named the 'Full CI' matrix: in the limit of an infinite basis set and an infinitely large expansion of single determinants, it must yield the exact ground-state energy, although this situation is clearly not realisable in any chemically realistic situation.

At the present time, full CI calculations are limited to very small systems because of the huge cost involved. For a system where the total number of spin orbitals is M, and N of them are occupied. The total number of n electron excited state determinants is given by $\frac{N!}{n!(N-n)!} \cdot \frac{M-N!}{n!(M-N-n)!}$. This number expands rapidly as we increase M and N, so that full CI rapidly becomes impractical. As a compromise we have to truncate our CI expansion, and this truncation defines a series of related approximate methods. The easiest way to limit the length of the expansion is to include only configurations that differ from the HF ground state determinant by no more than a certain number m of spin orbitals (m$\ll$N). Since the doubly excitation states mix directly with the HF ground state, one would expect

that they play the most important role in recovering the correlation energy. This is to some extent true for systems where c_0 is much larger than any other coefficents, in other words, the HF ground state is the dominant configuration in the CI expansion. Following this idea, the least costly CI method, DCI, where the wavefunction is expanded using the HF ground state and only the doubly excited states, was introduced. Singly-excited configurations are essential for calculating excited states, and they also have a strong influence on one-electron properties, but they do not mix directly with the HF ground state (indirect mixing via the doubly-excited states is possible but contributes little to the energy correction). The cost of their inclusion is however relatively minor (as there are fewer singly-excited states than doubles) so they are often included in the CI Singles and Doubles (SDCI method). These and other truncated CI methods all suffer from a significant error when the systems of interest becomes larger, which is they are not size consistent (nor size extensive, which is a stronger requirement). A calculation on a simple system of two noninteracting H_2 molecules serves to illustrate this point well. DCI limits the expansion of the trial wavefunction to only double excitations, so that the possibility of both H_2 molecules being simultaneously doubly excited (*i.e.* a quadruple excitation) is excluded. This excluded quadruple excitation term is exactly what is needed to yield an energy twice as large as the energy of a single H_2 molecule. As one would expect, the lack of size consistency limits the application of truncated CI methods greatly.

The Coupled Cluster Approximation (CCA)

There are methods where size consistency is ensured at the expense of some other properties of the full CI method. One of the most successful and widely applied methods is the coupled-cluster (CC) approximation[134]. The central idea of the CC

theory is that the full CI expansion can be expressed in another format:

$$|\Phi\rangle = e^{\mathbf{T}}|\Psi_0\rangle$$

$$\mathbf{T} = \mathbf{T}_1 + \mathbf{T}_2 + \cdots + \mathbf{T}_N$$

where $\mathbf{T}_i = \sum c_i \tau_i$, i being the number of electrons excited from ground state Ψ_0. N is the total number of electron in the system. Taylor expansion of the exponential function gives:

$$e^{\mathbf{T}} = 1 + \mathbf{T} + \frac{\mathbf{T}^2}{2!} + \frac{\mathbf{T}^3}{3!} + \ldots$$

so the singly, doubly, triply... excitation terms in CC expansion can be written as: $\mathbf{T}_1$, $\mathbf{T}_2 + \frac{\mathbf{T}_1^2}{2!}$, and $\mathbf{T}_3 + \mathbf{T}_2\mathbf{T}_1 + \frac{\mathbf{T}_1^3}{3!}$ ... After the Taylor expansion, all terms with total excitation number larger than N would be zero. The truncation in the CC method is realised by truncating the operator $\mathbf{T}$. For example the CCD method would be an approximate method where $\mathbf{T} = \mathbf{T}_2$ instead of $(\mathbf{T}_1 + \mathbf{T}_2 + \ldots + \mathbf{T}_N)$. In this case

$$|\Phi\rangle = e^{\mathbf{T}_2}|\Psi_0\rangle = \left(1 + \mathbf{T}_2 + \frac{\mathbf{T}_2^2}{2!} + \frac{\mathbf{T}_2^3}{3!} + \ldots\right)|\Psi_0\rangle$$

Notice now not only is the double excitation included, some of the quadruple, hextuple... excitations are included through $\mathbf{T}_2$, solving the size consistency problem. Again imagine we have two two-electron systems A and B. First we treat them separately using CCD:

$$\widehat{H}_A\Phi_A = \widehat{H}_A\, e^{\widehat{\mathrm{T}}_A}\,\Phi_A = \widehat{H}_A(1 + \widehat{\mathrm{T}}_{2A})\Phi_{0A} = E_A\Phi_A$$
$$\widehat{H}_B\,\Phi_B = \widehat{H}_B\, e^{\widehat{\mathrm{T}}_B}\,\Phi_B = \widehat{H}_B\,(1 + \widehat{\mathrm{T}}_{2B})\Phi_{0B} = E_B\,\Phi_B$$

Then we write out the CCD expansion for the system including non-interacting A and B:

$$\widehat{H}_{AB}\,\Phi_{AB} = \widehat{H}_{AB}\,e^{\widehat{\mathrm{T}}_{AB}}\,\Phi_{AB} = \widehat{H}_{AB}\Big(1 + \widehat{\mathrm{T}}_{2AB} + \frac{\widehat{\mathrm{T}}_{2AB}^2}{2!}\Big)\Phi_{0AB} = E_{AB}\Phi_{AB}$$

Because A and B are well separated, we can treat $\widehat{H}_{AB}$ as $\widehat{H}_A + \widehat{H}_B$, and Φ_{0AB} as $\Phi_{0A}\Phi_{0B}$. Also, $(1+\widehat{T}_{2A})(1+\widehat{T}_{2B})$ has exactly the same terms as $\Big(1 + \widehat{\mathrm{T}}_{2AB} + \frac{\widehat{\mathrm{T}}_{2AB}^2}{2!}\Big)$, because the electrons in system A will not be excited to orbitals in system B and *vice versa*. Thus,

$$\begin{aligned}
\widehat{H}_{AB}\Phi_{AB} &= \widehat{H}_{AB}\,e^{\widehat{\mathrm{T}}_{AB}}\,\Phi_{AB} \\
&= (\widehat{H}_A + \widehat{H}_B)\,e^{\widehat{\mathrm{T}}_A}e^{\widehat{\mathrm{T}}_B}\,\Phi_{0A}\Phi_{0B} \\
&= (\widehat{H}_A + \widehat{H}_B)\Phi_A\Phi_B = (E_A + E_B)\Phi_A\Phi_B
\end{aligned}$$

can be obtained through optimising the set of coefficient $\{c_{iAB}\}$.

The coefficients are determined by iteratively solving a set of CC equations generated via a projection scheme:

$$\begin{aligned}
\langle\Psi_0|e^{-\mathbf{T}}\mathbf{H}e^{\mathbf{T}}|\Psi_0\rangle &= E_{cc} \\
\langle\Psi_i|e^{-\mathbf{T}}\mathbf{H}e^{\mathbf{T}}|\Psi_0\rangle &= 0
\end{aligned}$$

where Ψ_0 is the HF ground-state determinant and $\{\Psi_i\}$ is the group of excited determinants which are included in the CC expansion for Φ. The E_{cc} calculated using the optimised coefficients in $\mathbf{T}$ is the final coupled-cluster energy. In the whole process intermediate normalisation is applied; that is $\langle\Phi|\Psi_0\rangle = 1$. The CC method is a very elegant way of incorporating electron correlation while retaining size consistency (and size extensivity, for it has proper multiplicative behaviour), but it is not a variational method, which means the energy calculated might be lower than the true ground state. In practice being non-variational is less of an

issue compared to losing size consistency, and as a result truncated CCA methods are much more popular than truncated CI.

Perturbation theory

Another non-variational but size consistent method including electron correlation is the Perturbation Theory method. The essence of this method is to describe a more complicated system as a simple system plus a series of small corrections. According to Rayleigh-Schrödinger perturbation theory[135], a general operator $\widehat{A}$ for a physical observable can be written as:

$$\widehat{A} = \widehat{A}^{(0)} + \lambda \widehat{V}$$

where $\widehat{A}^{(0)}$ is an operator for which we can solve the eigenvalue problem exactly and $\widehat{V}$ is the perturbation operator which acts as a correction. λ is a parameter in the range of 0 to 1. The eigenvalue problem for the more complicated system is now:

$$(\widehat{A}^{(0)} + \lambda \widehat{V})\Psi = a\Psi$$

The ground state Ψ_0 and corresponding eigenvalue a_0 is then expanded through Taylor expansion in λ at $\lambda = 0$:

$$\Psi_0 = \Psi_0^{(0)} + \lambda \Psi_0^{'(0)}|_{\lambda=0} + \frac{1}{2!}\lambda^2 \Psi_0^{''(0)}|_{\lambda=0} + \frac{1}{3!}\lambda^3 \Psi_0^{'''(0)}|_{\lambda=0} + \dots$$
$$a_0 = a_0^{(0)} + \lambda a_0^{'(0)}|_{\lambda=0} + \frac{1}{2!}\lambda^2 a_0^{''(0)}|_{\lambda=0} + \frac{1}{3!}\lambda^3 a_0^{'''(0)}|_{\lambda=0} + \dots$$

which can be abbreviated as:

$$\Psi_0 = \Psi_0^{(0)} + \lambda \Psi_0^{(1)} + \lambda^2 \Psi_0^{(2)} + \lambda^3 \Psi_0^{(3)} + \dots$$
$$a_0 = a_0^{(0)} + \lambda a_0^{(1)} + \lambda^2 a_0^{(2)} + \lambda^3 a_0^{(3)} + \dots$$

$a_0^{(0)}$ and Ψ_0 are the lowest lying eigenvalue and the corresponding eigenfunction of operator $\widehat{A}^{(0)}$. The n$^{\text{th}}$ term in the expansion of Ψ_0 (a_0) is the n$^{\text{th}}$ order correction for the eigenfunction (eigenvalue). Also, because the eigenfunctions for the HF equation $\widehat{A}^{(0)}\Psi^{(0)} = a^{(0)}\Psi^{(0)}$ are here assumed to form a complete set $\{\Psi_i^{(0)}\}$, any arbitrary $\Psi_0^{(n)}$ can be written in a linear combination

$$\Psi_0^{(n)} = \sum c_i \Psi_i^{(0)}$$

We now expand $(\widehat{A}^{(0)} + \lambda\widehat{V})\Psi_0 = a\Psi_0$ as

$$\begin{aligned}
&(\widehat{A}^{(0)} + \lambda\widehat{V})(\Psi_0^{(0)} + \lambda\Psi_0^{(1)} + \lambda^2\Psi_0^{(2)} + \lambda^3\Psi_0^{(3)} + \ldots) \\
=&(a_0^{(0)} + \lambda a_0^{(1)} + \lambda^2 a_0^{(2)} + \lambda^3 a_0^{(3)} + \ldots)(\Psi_0^{(0)} + \lambda\Psi_0^{(1)} + \lambda^2\Psi_0^{(2)} + \lambda^3\Psi_0^{(3)} + \ldots)
\end{aligned}$$

Because the equation stands for any λ between 0 and 1, the coefficient for all λ^n must be the same on the left and right hand side of the equation,

$$\begin{aligned}
\widehat{A}^{(0)}\Psi_0^{(0)} &= a_0^{(0)}\Psi_0^{(0)} \\
\widehat{A}^{(0)}\Psi_0^{(1)} + \widehat{V}\Psi_0^{(0)} &= a_0^{(0)}\Psi_0^{(1)} + a_0^{(1)}\Psi_0^{(0)} \\
\widehat{A}^{(0)}\Psi_0^{(2)} + \widehat{V}\Psi_0^{(1)} &= a_0^{(0)}\Psi_0^{(2)} + a_0^{(1)}\Psi_0^{(1)} + a_0^{(2)}\Psi_0^{(0)} \\
&\ldots \\
\widehat{A}^{(0)}\Psi_0^{(n)} + \widehat{V}\Psi_0^{(n-1)} &= a_0^{(0)}\Psi_0^{(n)} + a_0^{(1)}\Psi_0^{(n-1)} + \ldots + a_0^{(n)}\Psi_0^{(0)}
\end{aligned}$$

Imposing intermediate normalisation, we have

$$\langle\Psi_0|\Psi_0^{(0)}\rangle = 1$$

and since we have normalised $\Psi_0^{(0)}$, we also have

$$\langle\Psi_0^{(n)}|\Psi_0^{(0)}\rangle = 0\,(n \neq 0)$$

Multiply the first equation by $\Psi_0^{*(n)}$ $(n \neq 0)$ and integrating gives

$$\langle \Psi_0^{(n)} | \widehat{A}^{(0)} | \Psi_0^{(0)} \rangle = 0$$

Noticing

$$\langle \Psi_0^{(n)} | \widehat{A}^{(0)} | \Psi_0^{(0)} \rangle = \langle \Psi_0^{(0)} | \widehat{A}^{(0)} | \Psi_0^{(n)} \rangle$$

multiplying the second equation by $\Psi_0^{*(0)}$ and integrating gives

$$\langle \Psi_0^{(0)} | \widehat{V}^{(0)} | \Psi_0^{(0)} \rangle = a_0^{(1)}$$

Multiplying the second equation by $\Psi_j^{(0)}$, expanding $\Psi_0^{(1)}$ as $\sum c_{i1} \Psi_{i1}^{(0)}$ and integrating over all space gives

$$c_{j1} = \frac{\langle \Psi_{j1}^{(0)} | \widehat{V} | \Psi_0^{(0)} \rangle}{a_0^{(0)} - a_{j1}^{(0)}}$$

By doing similar operations on the third equation and plugging in the $a_0^{(1)}$ and $\Psi_0^{(1)}$ we have just obtained, we should be able to determine the second-order corrections. Recursively, one could ultimately determine all the n^{th}-order corrections and solve the perturbation problem.

Møller and Plesset described the eigen energy problem using perturbation theory and the treatment they proposed is now referred to by their names, the Møller-Plesset or MPn method[136], where n is the order at which the perturbation expansion equation is truncated. In the MPn approach, the zero-order Hamiltonian operator is defined as

$$\widehat{H}^{(0)} = \sum_{i=1}^{n} \widehat{f}_i$$

n being the number of basis functions. $\Psi^{(0)}$ are the HF eigenstates.

$$\widehat{V} = \sum_{i}^{k} \sum_{j>i}^{k} \frac{1}{r_{ij}} - \sum_{i}^{k} \sum_{j}^{k} (\mathbf{J}_{ij} - \frac{1}{2}\mathbf{K}_{ij})$$

where k is the highest lying occupied orbital. The first order corrected energy is the HF energy. MPn methods with n>1 recovers more electron correlation as n increases.

One can apply perturbation theory within or on top of other computational methods. For example in coupled cluster method, one can first include a few electron excitation terms in the CI expansion, and then correct the result, estimating the effect of the missing excitations terms using perturbation theory. The most successful and commonly applied method in this category is the CCSD(T) method, where singly and doubly excited configurations are fully included, and a singles-triples coupling term is added in to make amends for the absence of triply excitation corrections.

Multiconfiguration self-consistent-field (MCSCF)

Perturbation theory works best when the divergence from the reference wavefunction $\Psi_0^{(0)}$ is small, because only then is the Taylor expansion that underpins it valid. This leads to the conclusion that MPn methods which use the HF ground state as their reference are unable to give reliable results if the true ground state cannot be described qualitatively correctly by single determinant. Truncated CI methods and truncated coupled-cluster methods, especially those that truncate at double excitations, suffer from the same problem: if the underlying single determinant HF description does not give a qualitatively correct description of the electron distribution in the ground state, single and double excitations using the orbitals of this HF ground state will fail to capture much of the electron correlation. Systems

where the coefficient of the HF ground-state determinant does not dominate the CI expansion are generally referred to as having 'multi-configurational character'. Systems with degenerate or near degenerate ground states often fall into this category. Consider a HF close-shell singlet with near degenerate frontier orbitals, 1 and 2, which contain two electrons. HF theory presents two possible solutions, where the two electrons occupy either orbital 1 or orbital 2. The HF algorithm optimises the shapes of the occupied orbitals, and so the form of the lower lying orbitals depends on the identity of the orbital, 1 or 2, which is chosen to be occupied. In CISD or CCSD we could use the optimised HF ground-state determinant where orbital 1 is filled as Ψ_0 and construct a doubly excitation determinant Ψ_1^2 by swapping orbital 1 with the unoccupied orbital 2. One would expect the inclusion of this doubly excited term to play an important role in correcting the wavefunction but because the shape of orbital 2 is sub-optimal, the ability of this doubly excited term to capture the electron correlation is limited. To treat orbital 1 and 2 on an equal footing, we can construct a two-configuration wavefunction

$$|\Phi\rangle = c_1|\Psi^1\rangle + c_2|\Psi^2\rangle$$

where in $|\Psi^1\rangle$ orbital 1 is occupied and in $|\Psi^2\rangle$, orbital 2 is occupied. During the optimisation process, not only are the coefficients c_1 and c_2 defining the weights of these two configurations optimised, so too are the 1-electron orbitals that are used to construct the determinants. This approach is known as the 'multiconfiguration self-consistent-field' (MCSCF) approach. Generally it has the form of

$$|\Phi_{\text{MCSCF}}\rangle = \sum_i c_i|\Psi_i\rangle$$

Where the total wavefunction is expressed as a weighted sum of all configurations considered. The main difficulty lies in finding the best set of configurations to in-

clude. In a 'complete active space' (CAS) scheme for an n-electron system, we construct all the configurations by allowing any number $n'(n' \leq n)$ of electrons to be excited from the occupied orbitals to the virtual orbitals that constitute the active space. A (4,4) active space, for example, would include 4 electrons and 4 orbitals. To reduce the computational cost, it is possible to introduce a 'restricted active spaces' (RAS), from which (or into which) only a small number of electrons can be excited. Orbitals in the inactive space are allowed to relax but forced to be fully occupied or completely empty. Frozen orbitals, in contrast, maintain both their occupation and orbital shape throughout the calculation. The method used to optimise the total wavefunction expanded in different configurations constructed by specifying CAS (or RAS) is typically called *Complete Active Space Self Consistent Field*, CASSCF[137] (or RASSCF). Conventionally, the part of electron correlation that can be well captured by perturbation theory (MPn) is given the name 'dynamic correlation', as distinct from the 'non-dynamic correlation' or 'static-correlation' which is related to the existence of multi-configurational character in some specific systems. MCSCF methods capture this static-correlation much better than MPn and truncated CCA if the active space is well chosen, but MPn and truncated CCA do a better job in recovering 'dynamic correlation'. The boundary between these two types of correlation is vague, since both are introduced by the restrictions on the anti-symmetric function we use to represent the wavefunction and both would be fully included in full CI. Thus just as more 'static-correlation' can be recovered by incorporating more n-tuply excited terms in truncated CCA, more 'dynamic correlation' is included in by enlarging the active space of an MCSCF calculation. Convergence in either case is, however, very slow. An alternative approach is to apply the MPn method to an MCSCF wavefunction instead of a HF determinant at zeroth order, as is done in the CASPT2 or CASPT2N methodology of Roos and co-workers[138].

Density functional theory (DFT)

All the correlated methods discussed above can be traced back to the Hartree-Fock ansatz and can therefore be categorised as Post-HF methods. The advantage of these methods is that one can systematically improve the description of the wavefunction so that one approaches the 'exact energy', albeit at the expense of ever-larger computing costs which ensure that MCSCF soon become impractical for large active spaces. An alternative strategy is to use 'Density Functional Theory' (DFT) methods, which follow a distinctively different philosophy from the HF and post-HF methods. DFT has gained massive popularity mainly due to its high efficiency. Whilst often criticised for being 'not so *ab initio*', it is undeniable that DFT has become the technique of choice for the vast majority of computational inorganic chemists, especially when post HF calculations are too computationally demanding to be carried out. DFT methods have a solid theoretical foundation, starting from the paper by Hohenberg and Kohn[139] published in 1964 which marks the birth of 'density functional theory'. The first Hohenberg-Kohn theorem states that the external potential of a system is uniquely determined if the ground-state density is known. As the 'external potential' determines the Hamiltonian operator, the ground-state energy is necessarily a unique functional of the ground-state electron density. The second Hohenberg-Kohn theorem is a variational theorem which states that the energy of any arbitrary electron density of the system can be no lower than the true ground-state energy. Overall, the paper legitimized the use of electron density of a system as basic variable to find the ground-state energy. The appeal of using the density instead of the wavefunction as the central variable is immediately apparent: for systems with N electrons, a determinant depends on 3N variables while a density depends on only 3 spatial coordinates.

Before density functional theory was legitimised by Hohenberg and Kohn, there were many earlier attempts to use the electron density to approximate Hartree-

Fock theory. The total energy can be divided into a kinetic part and a potential part as usual:

$$E_{\text{tot}} = T + V_{\text{tot}}$$

The potential energy of an atomic or molecular system can be expressed using the electron density if we consider the system to behave classically:

$$V_{\text{tot}} = V_{\text{ne}} + V_{\text{ee}} = \sum_A \int \frac{Z_A}{|\mathbf{r} - \mathbf{R}_A|} \rho(\mathbf{r})\, \mathrm{d}\mathbf{r} + \frac{1}{2} \iint \frac{\rho(\mathbf{r})\rho(\mathbf{r}')}{|\mathbf{r} - \mathbf{r}'|}\, \mathrm{d}\mathbf{r}\mathrm{d}\mathbf{r}'$$

The first term describes the interaction between electrons and nuclei, and the second term describes the interaction between electrons. The above V_{tot} is, however, not exact: unlike HF theory where wavefunctions are restricted to be antisymmetric, we have no restrictions on the total electron density, nor do we have different treatments to electrons of different spin in our potential energy terms, thus electrons with different spins are not distinguished. Moreover, for a one-electron system V_{ee} is not necessarily zero, indicating the existence of an unphysical Coulomb interaction between an electron and itself. The problems call for a correction term. Aside from the correction term, we still need an expression for the kinetic energy. The first attempt to use the kinetic energy of the uniform electron gas was derived by Thomas and Fermi in 1927[140, 141],

$$T = \frac{3}{10}(3\pi^2)^{\frac{2}{3}} \int \rho^{\frac{5}{3}}(\mathbf{r})\, \mathrm{d}\mathbf{r}$$

However, using this kinetic energy term together with V_{tot} to calculate the total energy of a system, one gets an approximation that is too crude to give chemical meaningful results. Even when exchange effect is taken into consideration[142–144], the accuracy is far from ideal.

In 1965, Kohn and Sham[145] introduced a scheme to calculate the kinetic energy

in a way that resembles the calculation of kinetic energy in Hartree-Fock method. The essence of this method is to build up a fictitious system of non-interacting electrons which has the same ground-state electron density as the real system. The wavefunction of the fictitious system can be written as a Slater determinant constructed by one-electron spatial wavefunctions $\{\chi_i\}$. The total energy of the system is then

$$E[\rho(\mathbf{r})] = T_{\text{non-interacting}} + V_{\text{ne}} + V_{\text{ee}} + \Delta T + \Delta V_{\text{ee}}$$
$$= \sum_i^N \langle \chi_i | -\frac{1}{2}\nabla_i^2 | \chi_i \rangle + \sum_A \int \frac{Z_A}{|\mathbf{r} - \mathbf{R}_A|}\rho(\mathbf{r})\,\mathrm{d}\mathbf{r} + \frac{1}{2}\iint \frac{\rho(\mathbf{r})\rho(\mathbf{r}')}{|\mathbf{r} - \mathbf{r}'|}\,\mathrm{d}\mathbf{r}\mathrm{d}\mathbf{r}' + \Delta T + \Delta V_{\text{ee}}$$

$$\rho(\mathbf{r}) = \sum_i^N \langle \chi_i | \chi_i \rangle$$

Collecting the two correction terms ΔT and ΔV_{ee} together, we have the so-called 'exchange-correlation energy' term E_{xc}. Using a set of basis functions $\{\phi_\mu\}$, the problem of finding the ground-state energy and ground-state electron density becomes a problem of finding solutions for a secular equation

$$\mathbf{KC} = \mathbf{SC}\varepsilon$$

where

$$K_{\mu\nu} = \langle \phi_\mu | -\frac{1}{2}\nabla^2 - \sum_A \int \frac{Z_A}{|\mathbf{r} - \mathbf{R}_A|} + \int \frac{\rho(\mathbf{r}')}{|\mathbf{r} - \mathbf{r}'|}\,\mathrm{d}\mathbf{r}' + V_{\text{xc}} | \phi_\nu \rangle$$

$$V_{\text{xc}} = \frac{\delta E_{\text{xc}}}{\delta \rho}$$

The formalism for Kohn-Sham (KS) DFT bears a striking resemblance to Hartree-Fock although conceptually it is built upon a completely different base. HF is designed to be an approximate method, while for KS DFT, if we have the 'exact'

V_{xc}, we should get exact ground-state energy.

So far, however, the form of the exact V_{xc} term is unknown. Different V_{xc} terms have been proposed, mostly based on fitting to some particular simple electronic systems. One of the simplest formalism is the local density approximation (LDA). Under the LDA, E_{xc} is the spatial integration of $(\varepsilon_x + \varepsilon_c)$ calculated at all positions, where ε_x is the local exchange energy calculated at each point in space using the relation

$$\varepsilon_x = -\frac{3}{4}(\frac{3}{\pi})^{\frac{1}{3}} \int d^3\mathbf{r}\, \rho^{\frac{4}{3}}(\mathbf{r})$$

$\rho(\mathbf{r})$ is the 'local electron density'. The equation above calculates the exact exchange energy for the uniform electron gas system with electron density ρ, and can be extended to the spin-polarized regime in a straightforward fashion. ε_c is also a local functional of the density at a given point. It is designed to fit the 'correlation energy' of a set of uniform electron gas systems. Unlike the exchange energy, this 'correlation energy' is not analytical. It is obtained by subtracting the analytical exchange energy from the total E_{xc} calculated to high numerical accuracy. DFT methods using the spin-polarized formalism of ε_{xc} are sometimes regarded as local spin density (LSD) approximation methods. A step forward to increase accuracy is to calculate ε_x and ε_c at a given point using not only the local electron density, but also the gradient of density at that point. Functionals constructed in this manner are called the generalised gradient approximation (GGA) functionals. Most of the GGA functionals modify the expression for ε_x (or ε_c) by adding a correction term $\Delta\varepsilon_x\Big[\frac{|\nabla\rho(\mathbf{r})|}{\rho^{\frac{4}{3}}(\mathbf{r})}\Big]$ (or $\Delta\varepsilon_c\Big[\frac{|\nabla\rho(\mathbf{r})|}{\rho^{\frac{4}{3}}(\mathbf{r})}\Big]$) to the LDA exchange (or correlation) term and adopt the form

$$\varepsilon_x = \varepsilon_x^{LSD} + \Delta\varepsilon_x\Big[\frac{|\nabla\rho(\mathbf{r})|}{\rho^{\frac{4}{3}}(\mathbf{r})}\Big]$$

$$\varepsilon_c = \varepsilon_c^{LSD} + \Delta\varepsilon_c\Big[\frac{|\nabla\rho(\mathbf{r})|}{\rho^{\frac{4}{3}}(\mathbf{r})}\Big]$$

The GGA exchange functionals can be mainly divided into two groups. Exchange functionals such as the pioneering B functional developed by Becke[146], the CAM functional[147] and the O functional[148] belong to the first group, all of which have empirical parameters in the correction term optimised to fit to the energy of particular atomic systems. Exchange functionals in the second group have their correction terms constructed solely based on exact conditions. The popular PBE[149] functional belongs to the second group. Most of the correlation functionals are built in the form mentioned above including the widely used P86[150] and PW91[151]. These correlation functionals aim to reproduce the LDA correlation energy at the uniform electron gas limit. An exception is the LYP correlation[152] functional which, instead of correcting the LDA expression, adopts a completely different form which contains several empirical parameters fitted to the energy of helium atom. The next type of functional in the Taylor expansion series is the meta-GGA functional. While some meta-GGA exchange-correlation functionals further include a dependence on the second derivative of the density, others use the kinetic-energy density instead or use both the second derivative of the density and the kinetic-energy density for higher numerical stability. Another unique route to go down in functional design is to calculate the E_{xc} as

$$E_{\mathrm{xc_non-interacting}} + \Delta E_{\mathrm{xc}}$$

which resembles the idea of calculating the kinetic energy as $T_{\textit{non-interacting}} + \Delta T$. There will be no correlation energy or correction for kinetic energy if the system is non-interacting, thus $E_{\mathrm{xc_}\textit{non-interacting}}$ is just the exchange energy of the non-interacting system. It has exactly the same form as the HF exchange term except for the usage of KS orbitals instead of HF orbitals. ΔE_{xc} is constructed as $c(E_{\mathrm{xc}}^{DFT} - E_{\mathrm{x}}^{HF})$ where c is a constant percentage determined empirically. The final

form of E_{xc} includes one HF-style exchange term and other terms in LSD or GGA formalism, and is therefore described as a 'Hybrid functional'. The most popular hybrid functional to date is the B3LYP functional[153, 154]

$$E_{xc}^{B3LYP} = 0.8E_x^{LSD} + 0.2E_x^{HF} + 0.72\Delta E_x^{B} + 0.19E_c^{LSD} + 0.81E_c^{LYP}$$

which combines B exchange with non-interacting exchange calculated in HF fashion and uses LYP correlation functional.

All KS-DFT methods except those using hybrid functionals could avoid the two-electron-integral calculations by expanding the electron density in an 'auxiliary basis set' to evaluate Coulomb integrals and Exchange-correlation integrals. Using this approach would reduce the scaling of the method with respect to system size. As for hybrid functionals, calculation for E_x^{HF} is essentially the efficiency bottleneck of the methods. Nevertheless, all KS-DFT methods mentioned above scale no worse than N^4, N being the number of KS basis functions. The efficiency of KS-DFT is outstanding among all the correlated methods, and this feature has allowed it to reach its current pre-eminent position in computational inorganic chemistry.

2.2.4 Basis sets

Having introduced the commonly used computational methods, we emphasise the point that the HF method, along with all post HF methods and KS-DFT, share a common reliance on basis functions to expand the 1-electron wavefunctions (the orbitals). As we have discussed in earlier sections, a calculation using a complete basis set defines the accuracy limit of a method, but a complete basis set has an infinite number of independent basis functions which is, of course, not obtainable in practice. In fact, the quality of the chosen basis set directly determines the accuracy

of one's calculation.

Slater-type and Gaussian-type orbitals (STOs and GTOs)

Ideally one wants to describe the spin orbitals as accurately as possible using a number of basis functions. For chemists, the obvious first choice is to use a type of function which formally resembles atomic orbitals, the so-called Slater-type orbitals[155] (STOs):

$$\chi_{\zeta,n,l,m}(r,\Theta,\varphi) = NY_{l,m}(\Theta,\varphi)r^{n-1}e^{-\zeta r}$$

where n, l and m are the primary, azimuthal and magnetic quantum numbers of the orbital, N is the normalisation factor and $Y_{l,m}(\Theta,\varphi)$ is the spherical harmonic function. Aside from $R_{n,l}(r)$ being simplified as r^{n-1}, STOs have exactly the same form as electronic wavefunctions of hydrogen-like atoms. Using STOs to describe the spatial orbital and combining it with a spin component $\alpha(\omega)$ or $\beta(\omega)$, one gets a spin orbital. Replacing $R_{n,l}(r)$ by r^{n-1} means that a single STO has no radial nodes, and so a linear combination of STOs is used to represent atomic orbitals with radial nodes. The difficulty of applying STOs as a basis set lies in the evaluation of all the two electron integrals: these integrals cannot be expressed in a simple analytical form and as a result the calculations are very difficult to perform in general. In KS-DFT methods (except when using hybrid functionals), one can avoid the problem by using auxiliary functions of other forms to fit to the density, but in HF or post HF methods, the evaluation of two electron integrals is unavoidable. In the 1950's, Boys proposed the use of the alternative Gaussian-type orbitals[156] (GTOs) as basis functions. These can be written in the form:

$$\chi_{\zeta,n,l,m}(r,\Theta,\varphi) = NY_{l,m}(\Theta,\varphi)r^{2n-2-l}e^{-\zeta r^2}$$

GTOs have an r^2 dependence in the exponential rather than the r dependence of STOs, and as a result a single GTO describes a given atomic orbital less accurately than a single STO. In particular, GTOs decay too quickly away from the nucleus. Moreover, unlike STOs where the right-hand derivative of the function goes to a negative number when r approaches zero, the right-hand derivative of GTOs goes to zero, resulting in problematic behaviour of GTOs near the nucleus. Consequently, one would need to combine many more GTOs to describe an atomic orbital to a given accuracy. There are, however, some crucial advantages of GTOs over STOs as basis functions. The first is that they are separable in the x, y and z directions, and the other is that the product of two GTOs is also a GTO (the "Gaussian product theorem"). These two features make the evaluation of two electron integrals much easier for GTO-type basis sets, and this far outweighs the disadvantages GTOs have over STOs. Therefore, for HF and post HF methods, GTOs have become the standard choice of basis functions. In non-hybrid KS-DFT, in contrast, there is little advantage to using GTOs because the 2-electron integrals are not required, and so STOs or basis set of other types are sometimes preferred in commercial codes (the Amsterdam Density Functional package, for example).

Within a given type of basis set there is a hierarchy of levels of well-defined accuracy, gradually going towards a basis set limit. In STOs, the hierarchy is introduced by

1. Gradually adding the number of STOs of the same symmetry but different exponent ζ for each atomic orbital.

2. Gradually adding a number of sets of polarization functions.

The smallest basis set is called a minimal basis set or Single Zeta (SZ) basis set. It employs the minimum number of basis functions needed to describe an atom's core and valence orbitals. For example, it has only 5 STOs for second row elements:

2 s-functions to describe 1s and 2s orbitals, and one set of p-functions to describe the three 2p orbitals. Doubling the SZ basis set one would get the the Double Zeta (DZ) basis set, where four s-functions with different ζ would be used to describe 1s and 2s orbital, two sets of p-functions with different ζ would be used to describe 2p orbital, and so on... Extending this idea, there is Triple Zeta (TZ), Quadruple Zeta (QZ) and higher Zeta basis sets, where more and more functions of the same angular momenta but different ζ are used to describe each atomic orbital. The inclusion of more STOs with different ζ allows the orbitals to 'breath' to accommodate different electronic environments without changing symmetry, thus creating a more flexible description. On the other hand, to reach higher accuracy, the atomic orbitals should be allowed to be 'polarised', that is to break their symmetry in response to the environment that the atom finds itself. This is done by adding in 'polarisation functions', for example, a set of p-functions when describing an atomic s orbital, a set of d-functions to polarise atomic p orbitals *etc*. Basis set incorporating sets of polarisation functions are named Double/Triple/Quadruple...Zeta plus Polarisation (nZP) basis set. One can also add more sets of polarisation functions to increase the quality of the basis set, but should be careful when doing so because basis sets which are too heavily polarised can be unbalanced, introducing artefacts.

The hierarchy can be constructed in a similar way in GTOs basis sets. The main difference is that the matter is more complicated, for one need to consider how to 'contract' the GTOs basis sets. As mentioned earlier, single GTO does not reflect the nature of atomic orbitals well. In practice, one can use a set of GTOs to fit to some STOs, or more commonly, determine the exponents of the GTOs by minimising the energy of simple electronic systems such as atoms and small molecules. The functions involved in the energy minimisation are called 'primitive functions'. While a large number of primitive functions will be used to describe the energet-

ically more important core orbitals, these core orbitals are less important chemically. Thus, instead of allowing the coefficients of all the primitive functions to vary during the HF (or KS-DFT) variational process, the primitive GTOs can be combined into a smaller set of functions called contracted GTOs to describe the atomic orbitals, with the coefficients of the primitives in the contraction fixed to some pre-determined values. In this way, one can use a large number of primitive GTOs to gain a relatively good description of the core orbital while at the same avoiding the need to optimise the coefficient for every primitive GTOs during the variational process, which would expand the dimension of the Fock or Kohn-Sham matrix. The number of functions with different zetas within the nZP hierarchy in STOs here becomes the number of contracted GTOs used to describe an atomic orbital. There are two ways of contracting basis sets, the so-called 'segmented' contractions and the 'general' contractions. The former divides the primitive functions into disjoint sets, which means the primitive functions are each used once when building contracted functions. In the latter, all primitive functions on an atom are used in every contracted function, but with different contraction coefficients. In practice most general contracted basis sets leave the outermost primitive GTOs uncontracted but are still regarded as 'general contracted basis sets' for their heavily contracted nature. Segmented contracted basis sets are more efficient computationally when calculating the integrals. This is more important for the HF method where the computation of integrals is the bottle neck that controls the computing time. For post HF methods, the computation time and quality mainly depend on the number of 'atomic orbitals' used in the calculation, thus large, heavily contracted basis sets of general contraction type are usually preferred. Popular segmented contracted basis sets include Pople Style Basis Sets such as 6-31G(d,p) and Dunning-Huzinaga Basis Sets. Atomic Natural Orbital (ANO) Basis Sets and Correlation Consistent Basis Sets (cc-pVnZ) are widely applied general contracted

basis sets for post HF calculations. Accuracy can be further increased for specific systems by using augmented basis sets. The 'augmentation' involves including diffuse functions to provide a better description on the 'tail' of the wavefunctions or including a tight function to better describe the core region of the wavefunctions. Also, the contracted basis sets can be recontracted with another set of coefficients obtained from a relativistic calculation to incorporate scalar relativistic effects.

Plane wave basis set and pseudo-potential

Both STOs and GTOs are constructed with the aim of modelling atom-centred orbitals. In contrast, plane wave basis functions (such as those used in Chapter 5) take the form of 'near free electron' wavefunctions which are uniquely compatible with periodic system. Bloch's theorem[157] states that the eigenstates of an electron in a potential with translational symmetry (*e.g.* in a crystal) can be described by a Bloch wave:

$$\psi_{n,\mathbf{k}}(\mathbf{r}) = e^{i\mathbf{kr}} f_{n,\mathbf{k}}(\mathbf{r})$$

where $\mathbf{k}$ is a real vector in reciprocal space, n is the electron band index and $f_{n,\mathbf{k}}(\mathbf{r})$ has the property

$$f_{n,\mathbf{k}}(\mathbf{r}) = f_{n,\mathbf{k}}(\mathbf{r} + \mathbf{T})$$

$\mathbf{T}$ being any translational vector which leaves the Hamiltonian invariant. By taking advantage of the periodicity of the system, the Bloch theorem simplified the form of one-electron wavefunctions to a product of a part with the same periodicity as the potential, also known as the 'cell-periodic' part, and a part that controls the 'phase' $e^{i\mathbf{kr}}$. In practice, one can apply periodic conditions to a 'unit cell' to represent an infinite system. The cell-periodic part $f_{n,\mathbf{k}}(\mathbf{r})$ can be written as a linear

combination of plane waves

$$f_{n,\mathbf{k}}(\mathbf{r}) = \sum_{\mathbf{G}} c_{\mathbf{G}n\mathbf{k}} e^{i\mathbf{G}\mathbf{r}}$$

where $\mathbf{G}$ are reciprocal lattice vectors defined by

$$\mathbf{G} \cdot \mathbf{T} = 2\pi N, N \in \mathbb{Z}$$

Thus the wavefunction $\psi_{n,\mathbf{k}}(\mathbf{r})$ can be expanded as

$$\psi_{n,\mathbf{k}}(\mathbf{r}) = \sum_{\mathbf{G}} c_{\mathbf{G}n\mathbf{k}} e^{i(\mathbf{G}+\mathbf{k})\mathbf{r}}$$

It is obvious that all unique solutions of $\psi_{n,\mathbf{k}}(\mathbf{r})$ can be characterised by $\mathbf{k}$ within the first Brillouin zone, since the right hand side of the equation sums over all $\mathbf{G}$, and any $\mathbf{k}'$ outside of the first Brillouin zone can be expressed as $\mathbf{k}' = \mathbf{k} + \mathbf{g}$, where $\mathbf{k}$ is a vector inside first Brillouin zone and $\mathbf{g}$ is some reciprocal lattice vector.

Again, the use of an infinite basis set is only achievable in an ideal world: in reality, one has to define a finite basis using the following steps. First, instead of running an infinite number of $\mathbf{k}$ vectors, only a special set of k-points in the first Brillouin zone is sampled. Second, a cut-off value E_{cutoff} is set. For a specific $\mathbf{k}$, only plane wave basis functions with $\frac{\hbar}{2m}|\mathbf{G} + \mathbf{k}|^2 < E_{\text{cutoff}}$ are included. The cut-off value E_{cutoff} has the unit of energy and $\frac{\hbar}{2m}|\mathbf{G} + \mathbf{k}|^2$ can be viewed as the kinetic energy of plane wave $e^{i(\mathbf{G}+\mathbf{k})\mathbf{r}}$. The size of a plane wave basis set (the number of plane wave basis functions used) is thus determined by the cut-off value and the size of the 'unit cell' chosen to describe the periodic system, and not by the type or number of atoms in the unit cell, unlike STO or GTO basis sets. The contents of the unit cell determine the external periodic potential that the electrons are in.

Atomic orbitals usually oscillate rapidly in the vicinity of the nuclei and rather

smoothly on the outer region. The near-core oscillations of the valence orbitals are mostly caused by the fact that they have to be orthogonal to the core electrons and are not important to chemical bonding, but to precisely describe these rapid oscillations, the cut-off value would have to be very large in order to include plane waves with short wavelengths. Pseudo-potential methods are therefore usually employed in conjunction with plane wave basis sets. The essence of pseudo-potential methods is to replace the potential created by the 'bare nuclear charge' with some fictitious potential, so that under such potential, the electron in the 'pseudo orbital' behaves exactly like the true valence electron outside some pre-defined cut-off radius from the nuclei, but the wavefunction oscillates much less within the cut-off radius. The pseudo-potentials are designed in a way that the 'pseudo-orbitals' under the pseudo-potential have exactly the same energy eigenvalue as their corresponding valence orbitals from the 'all-electron' calculation, the same shape and amplitude as their corresponding valence orbitals outside the cut-off radius, and the same first and second derivatives as their corresponding valence orbitals at the cut-off radius. When a pseudo-potential is used, the nucleus and the core electrons can be viewed as a single ion-like entity which determines the external potential that the valence electrons 'feel'. There are two main consequences to the use of pseudo-potentials. The first is that no plane wave basis functions are required to expand the core electrons, which are effectively removed from the calculation. The second is the valence electron orbitals have no core-electron orbitals to be orthogonal to, so that the near-core rapid oscillation feature is gone. Therefore, it can give correct chemical information of the system at a much lower cost, as long as the cut-off radius is set to a reasonable value. The method applied in this study is the Projector Augmented Wave (PAW) method[158], which is a generalised pseudo-potential method. In this method, the valence all-electron wavefunction $|\psi\rangle$, which is the valence electron wavefunction under the external

potential created by bare nuclear charge, is linearly transformed to a pseudo wavefunction $|\tilde{\Psi}\rangle$ following

$$|\Psi\rangle = \widehat{\mathcal{T}}|\tilde{\Psi}\rangle = (1 + \sum_R \widehat{\mathcal{T}_R})|\tilde{\Psi}\rangle$$

$\widehat{\mathcal{T}_R}$ are atom-centered local operators. They are only non-zero within certain augmentation regions enclosing the atoms. The index R refers to different atomic sites. Within the augmentation regions Ω_R, the smooth pseudo wavefunction $|\tilde{\Psi}\rangle$ can be expanded into a series of pseudo partial wavefunctions.

$$|\tilde{\Psi}\rangle = \sum_i c_i |\tilde{\phi}_i\rangle$$

where

$$(1 + \widehat{\mathcal{T}_R})|\tilde{\phi}_i\rangle = |\phi_i\rangle$$

$|\phi_i\rangle$ are solutions of the radial Schrödinger equation for the isolated atom R.

$$c_i = \langle \tilde{p}_i | \tilde{\Psi} \rangle$$

The projectors $\langle \tilde{p}_i|$ are calculated as radial functions multiplied by spherical harmonics which satisfy:

$$\langle \tilde{p}_i | \tilde{\phi}_j \rangle = \delta_{ij}$$

The core electrons are formally retained in the PAW method. The core state is expanded as

$$|\psi^c\rangle = |\tilde{\psi}^c\rangle + |\phi^c\rangle - |\tilde{\phi}^c\rangle$$

where $|\tilde{\psi}^c\rangle$ is the nodeless pseudo core wavefunction, $|\phi^c\rangle$ is the all electron wavefunction for core electron and $|\tilde{\phi}^c\rangle$ is the pseudo partial wave. The latter two are expressed as products of a radial function and a spherical harmonic. The PAW

method allows us to obtain some physical quantities $\langle\Psi|\mathbf{A}|\Psi\rangle$ of the all electron wavefunction $|\Psi\rangle$ from the pseudo wavefunction $|\tilde{\Psi}\rangle$ by calculating $\langle\tilde{\Psi}|\mathcal{T}^{\dagger}\mathbf{A}\mathcal{T}|\tilde{\Psi}\rangle$. The essence of the PAW method is to decompose the wavefunction into auxiliary plane wavefunctions and atom-centered local partial wavefunctions which oscillate rapidly, and then treat them separately.

Chapter 3

Clusters containing a single transition metal: functional dependency

3.1 Introduction

The factors that control the structure of tetrel clusters that encapsulate a single transition metal atom will be the discussed in this chapter. In order to establish the foundation of this discussion, I will first report the results of our investigation into the $[M@Si_{14}]^z$ clusters, through which we will see how the 'fullerene-like' and 'deltahedral type' clusters are related to each other. As mentioned in Chapter 1, the severe functional dependency issue is what leads us to look into the $[M@Si_{14}]^z$ clusters. By examining how the relative stability of a few different isomers varies across the periodic table with three different functionals PBE, BLYP and B3LYP, we discovered that the strong functional dependency issue is not restricted to group VI and VIII transition metal encapsulating 14-vertex silicon clusters. In fact, the relative stability of 'fullerene-like' clusters is always systematically overestimated relative to the deltahedral type with LYP functionals such as BLYP and B3LYP. The origin of this phenomenon will be discussed following the results on the structures

of $[M@Si_{14}]^z$ clusters. Finally, we show how the story of $[M@Si_{14}]^z$ clusters fits into the broader context, and how our findings for the 14-vertex clusters hold true for single metal encapsulating tetrel clusters in general. Part of my research reported in this chapter have already been published in *Dalton Transactions*, volume 46, 2017. The paper can be found in the appendix for reference.

3.2 Computational methods

All DFT calculations described in this chapter were performed with the Amsterdam Density Functional package[159–161] (ADF2013.01) using the gradient-corrected (GGA) functional proposed by Becke, Lee, Yang and Parr[146, 152] (BLYP), Perdew, Burke and Ernzerhof[149] (PBE) and hybrid functional B3LYP[153, 154]. Basis set convergence tests were carried out, as a result of which, an all electron Slater-type ZORA basis set[162] of triple-ζ quality, extended with a single polarisation function (TZP), was used to describe all the metal atoms while a DZP basis set was used to describe Si. All structures were optimised using the gradient algorithm of Versluis and Ziegler[163]. The scalar relativistic zeroth-order regular approximation (ZORA) to the Dirac equation is used in all calculations[164–168]. The Conductor-like Screening Model[169–172] (COSMO) of solvation was applied to all DFT calculations with ϵ=78.4. Frequency calculations were performed numerically.

Coupled cluster single point calculations were performed with the ORCA 3.0.3 package[173, 174]. Dunning correlation-consistent polarised triple zeta basis sets (cc-pVTZ) were used to expand the orbitals[175, 176]. Aside from the standardised CCSD(T) calculation, we also used a newly-implemented local correlation method, Domain based local pair natural orbital (DLPNO) CCSD(T)[177, 178]. The idea behind the method is that because electron pair correlation energies decay very quickly with the distance between the centroids of the localised occupied or-

bitals, in an electronic system a large number of electron pairs are only 'weakly correlated' and their contribution to the CCSD correlation energy is negligible, and can be treated with perturbation theory instead. The method is said to be robust and able to recover 99.9% of the CCSD(T) correlation energy. The high efficiency of DLPNO-CCSD(T) allowed us to perform calculations with cc-pVTZ and cc-pVQZ basis sets and apply extrapolation technique to obtain the basis set limit energy. The extrapolation[179] is done with ORCA using the two-point extrapolation method where SCF energy and correlation energy are extrapolated separately.

The Molcas 8.0 program[180, 181] was used to carry out the CASSCF/CASPT2 calculations[137, 138] . Cholesky decomposition of the two-electron repulsion integrals was used with medium accuracy (threshold 1.0d-6). In CASPT2 calculations, an imaginary shift of 0.1 a.u. was applied to prevent intruder states. ANO-rcc type basis sets[182, 183] were used. The basis set is contracted to $[6s4p3d2f1g]$ on Cr and $[4s3p1d]$ on Si. In the PT2 process, the 'frozen deep core' scheme was used where only valence electrons (including Si $2p$ and Cr $3s$, $3p$) were correlated.

In both CCSD(T) and CASSCF/CASPT2 calculations, the geometry was taken from optimised DFT geometry using B3LYP functional.

3.3 DFT study of $[M@Si_{14}]^z$ clusters

3.3.1 Overview of the potential energy surface

We first calculated the relative energy of different isomers of neutral $M@Si_{14}$ clusters using three functionals that lie at the centre of the controversy in the literature: PBE, BLYP and B3LYP, to gain an overview of the potential energy surface. The structures considered are shown in Figure 3.1.

All isomers shown in Figure 3.1 have been reported in the literature. We have already briefly touched on the subject of the conflicting claims for isomers A, B

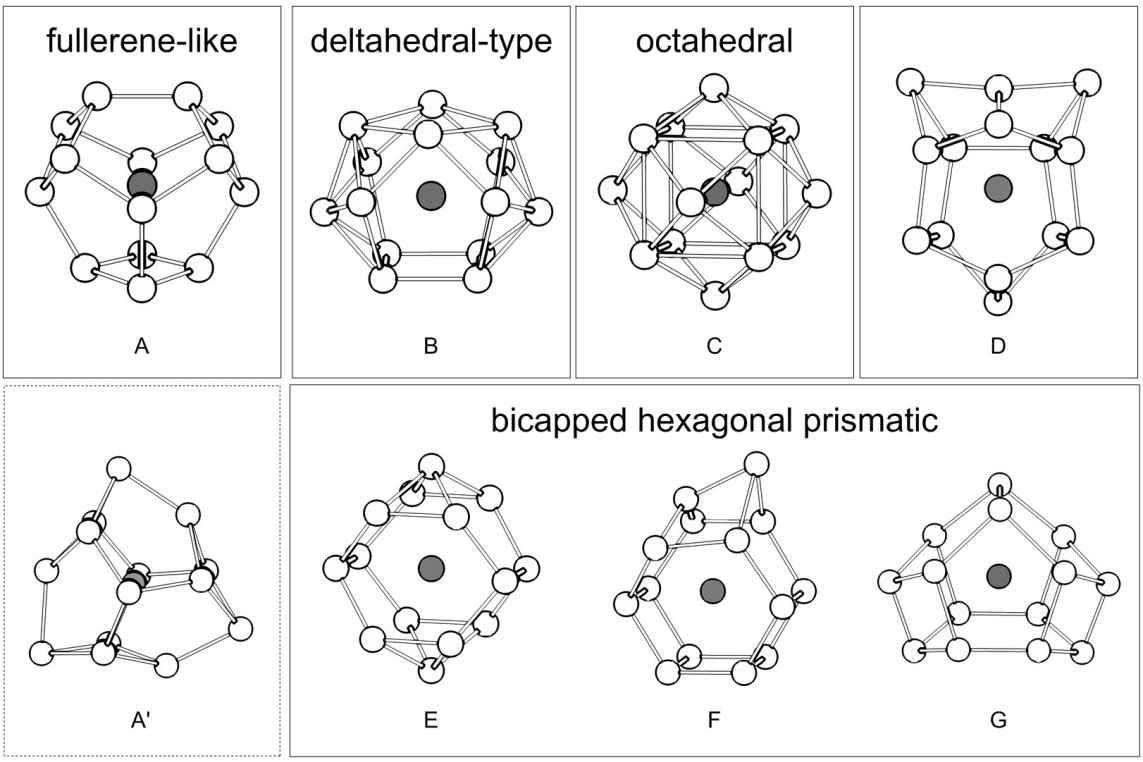


Figure 3.1: Structures of M@Si_{14} isomers

and C in Chapter 1. Both isomer A and B are reported to be the ground-state isomer for Cr@Si_{14}[110, 123, 124], while both isomer A and C are claimed to be the most stable isomer for $FeSi_{14}$[46, 99, 111, 112, 124] by different researchers, using different DFT functional. Isomer A' is the reported ground-state isomer for Zn@Si_{14} in Guo's study[94]. Isomer D is proposed to be the lowest lying isomer for Co@Si_{14} and Ni@Si_{14} by Wang[97] and He[124], respectively. Both the bicapped hexagonal prisms E and F are reported to be stable isomers for early transition metal encapsulating silicon clusters[107, 109, 124], while isomer G has been suggested by Lu[103] to be the most stable isomer for W@Si_{14}. Despite Lu's argument for isomer G, we have never found this isomer to be the global minimum in any of the systems studied here, thus the energy of this isomer is not plotted in any of the figures below. We have selected the energy of isomer C as our reference, which is shown as the green lines in all of the relative energy plots (Figure 3.2 and 3.3). Figure 3.2

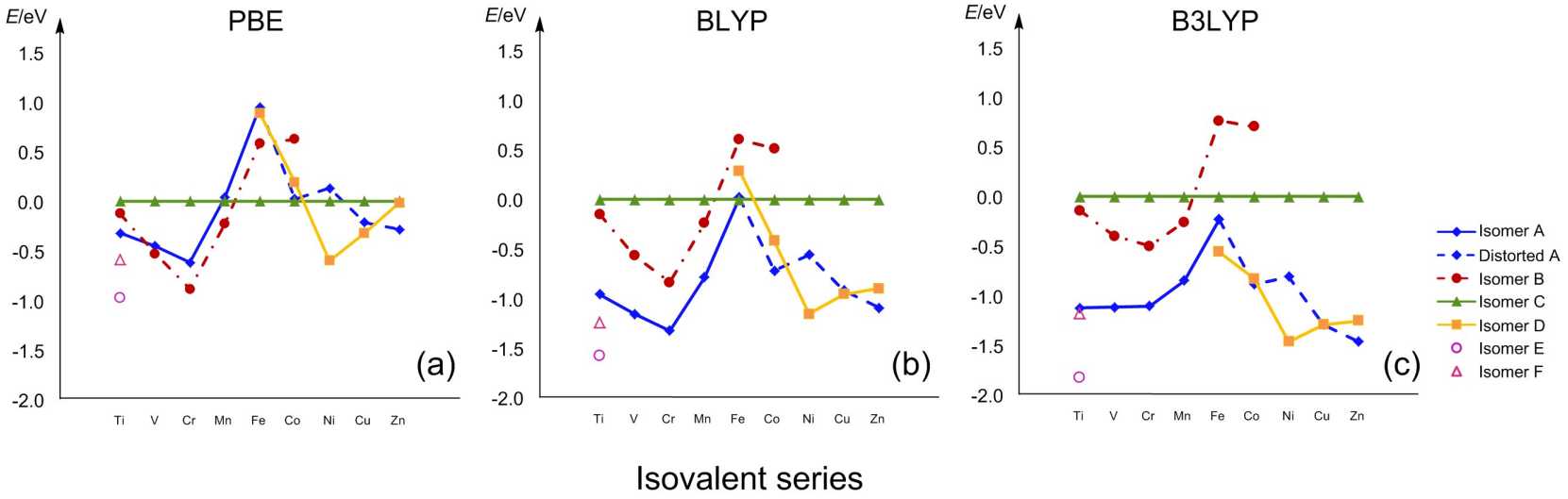


Figure 3.2: Relative energies of the neutral M@Si_{14} isomers A to F

illustrates how the relative energies of M@Si_{14} clusters containing a 1^{st} row transition metal vary when different functionals are applied. The structures are allowed to distort to reach true energy minima, and all points plotted in Figure 3.2 are checked to ensure that they have no imaginary frequencies, indicating that they are indeed minima on the potential energy surface. At first glance, the three plots, a-c, looks quite different. A closer inspection shows that the broad stability pattern are similar across all three plots, and only the lines are shifted up and down when different functionals are in use. Therefore, it is not unreasonable to assume that the stability trend should be explicable in terms of fundamental principles of chemical bonding, that are independent of functional. As shown in the figure, the bicapped hexagonal prismatic isomers E and F have the lowest lying energies for Ti@Si_{14}, which matches with Kumar's[109] and Torres's[107] findings. These two structures distort heavily and their relative energies increase rapidly as we move towards the right hand side of the periodic table. Even for V@Si_{14} , their structures are hardly recognisable as bicappped hexagonal prisms. From V@Si_{14} to Fe@Si_{14} , the energies of isomer A and isomer B lie almost parallel, both reaching a minimum around Cr@Si_{14}. The source of the conflicting claims in the literature for the equilibrium structure of Cr@Si_{14} is immediately apparent: the PBE functional recognises isomer B as the most stable isomer, while the B3LYP (and BLYP) functionals place isomer A below isomer B. Similarly, the Fe@Si_{14} cluster is problematic as it lies close to the intersection of the curves for isomers A and C. When the PBE functional is applied, isomer C is much lower in energy compared to isomer A for Fe@Si_{14} but switching to B3LYP reverses this order. Going further to the right hand side of the periodic table, isomer B starts to distort heavily into low symmetry isomers, but the relative energy of these distorted isomers remains high. As these isomers are not stable enough to compete for the ground state, the energy curve of (distorted) isomer B is not plotted beyond cobalt in the figure. Isomer A, on the other hand,

distorts systematically by compressing along the C_3 axis and gradually throwing silicon atoms out of the coordination sphere of the central metal. For $Cu@Si_{14}$ and $Zn@Si_{14}$, the structure of A becomes the highly distorted isomer A' in Figure 3.1, with near perfect C_{3h} symmetry, looking similar to a three-bladed fan. Isomer A' is the most stable isomer for $Zn@Si_{14}$ in our study, independent of functional choice. This result is in agreement with Guo's study[94] where BLYP was applied to study the structures of $M@Si_n$ (M = Sc-Zn, n= 8-16). The other stable isomer on the right hand side of the periodic table is isomer D. Both isomer A and isomer D have 3-connected vertices and a few silicon atoms outside the coordination sphere of the central metal. Although they are often close in energy, their relative energies vary little across the three plots, unlike the case of isomer A and isomer B. If we scrutinise the plots in Figure 3.2 and compare the results obtained by different functionals, we can make two obvious observations. The first one is that the shape of each curve for different isomers is broadly the same in PBE and BLYP but a little different in B3LYP. This is readily understandable if we look into the spin states of these plotted minima. It is a well-established finding that B3LYP and other hybrid functionals tends to stabilise systems with higher spin states compared to GGA functionals. Here, the differences in the shape of the curves can be explained by the isomers adopting different spin states. For $V@Si_{14}$, isomer C is a quartet while isomers A and B are doublets. For $Cr@Si_{14}$, isomer C is a triplet while isomers A and B are singlets. In both cases isomer C is further stabilised in its higher spin state in B3LYP, causing the curves for both isomer A and B to become less acute around $Cr@Si_{14}$. The same reasons can be applied to explain the stabilisation of isomers A and D at $Fe@Si_{14}$ in the B3LYP plot, since isomers A and D are triplet while isomers B and C are singlets. The second observation is that the isomers can be broadly divided into two groups: isomers A, D, E and F and, isomers B and C. Within the two groups the relative energies of isomers are relatively indepen-

dent of functional. Switching from PBE to either BLYP or B3LYP stabilises isomers from the first group relative to the isomers from the second group. As BLYP and B3LYP share the same electron correlation component, this observation suggests that the isomers within the same group share some common features in terms of the electron-electron repulsions. We will come back to this point later after we have looked into the electronic structure of isomers A, B and C.

The controversy in the literature lies mainly among isomer A, B and C. Our calculations also show that independent on the functional choice, the bicapped hexagonal prismatic isomer E is the most stable structure for $Ti@Si_{14}$, and isomers A′/D undoubtedly dominate the structural landscape for the late transition metal encapsulating silicon clusters. To further pursue the possible sources of the conflicting results, from here onward we focus on isomer A, B and C. We can obtain a different perspective on the balance between these isomers by considering the effect of charge changing within an isoelectronic series. Figure 3.3 presents the varying relative energies of isomer A, B and C within the 62-valence-electron series, $[Ti@Si_{14}]^{2-}$, $[V@Si_{14}]^{-}$, ..., *etc*. Besides the energy shift of isomer A against isomer B and C when switching to BLYP and B3LYP from PBE, the most striking feature of these plots is that positive charge destabilises isomer B strongly with respect to both isomers A and C. The controversy over the global minimum of $Cr@Si_{14}$ and $[V@Si_{14}]^{-}$ does not, therefore, extend to Ti^{2-} or Fe^{2+}, where isomer B and A, respectively, are most stable. From the shape of the curves, we infer that the stability of isomer B relies more on the availability of metal *d*-electron density than the other two isomers and so is favoured when the metal *d* electrons are more diffuse. The seemingly peculiar points at $[Mn@Si_{14}]^{+}$ in the B3LYP plot may be related to the heavy spin contamination for isomer C in B3LYP. The expectation value of $\widehat{S^2}$ is listed in Table 3.1 for isomer C calculated in B3LYP. The exact value $\langle\widehat{S^2}\rangle$ should be S(S+1), where S is the spin quantum number, but as discussed in

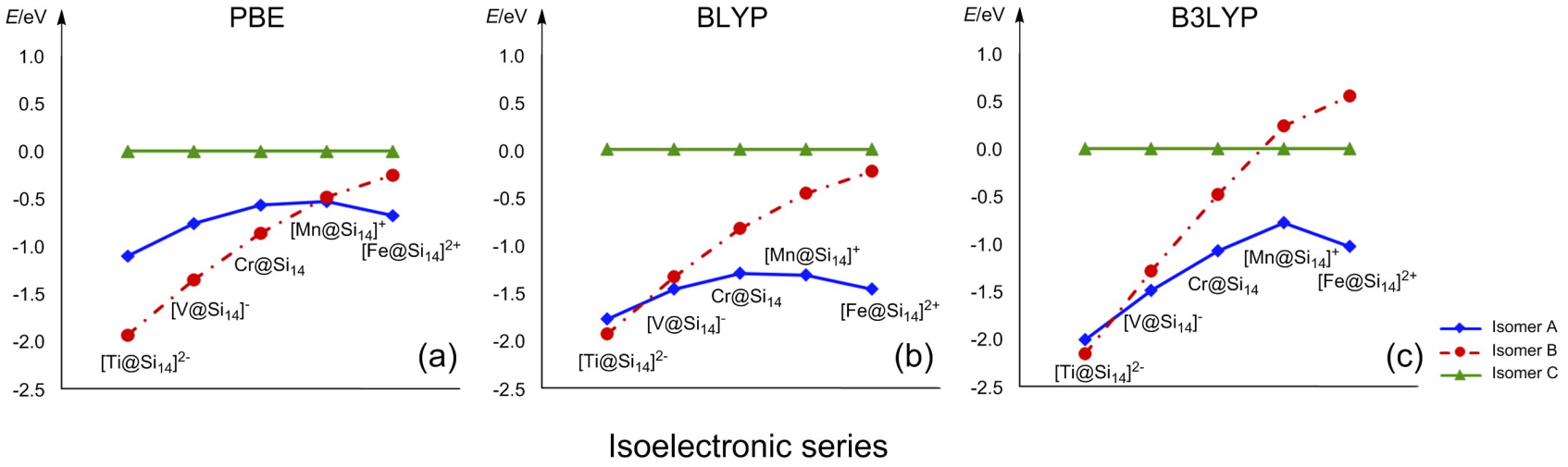


Figure 3.3: Relative energies of isomers A, B and C for the 62-valence-electron $[M@Si_{14}]^z$ clusters

	S(S+1)	$\langle \widehat{S^2} \rangle$
$[Ti@Si_{14}]^{2-}$	2.00	2.02
$[V@Si_{14}]^{-}$	2.00	2.05
$Cr@Si_{14}$	2.00	2.28
$[Mn@Si_{14}]^{+}$	2.00	2.65
$[Fe@Si_{14}]^{2+}$	2.00	2.24

Table 3.1: $\langle \widehat{S^2} \rangle$ values for the 'triplet' isomer C calculated in B3LYP

Chapter 2, unrestricted HF single determinants are not necessarily eigenfunctions of $\widehat{S^2}$. The deviation of the expectation value $\langle \widehat{S^2} \rangle$ from the exact value is an indicator for the extent of spin contamination in a system and is largest for $[Mn@Si_{14}]^{+}$. Isomers A and B are computed as close-shell singlets, so that spin contamination is a problem in neither of these cases. In fact, if we examine the $\langle \widehat{S^2} \rangle$ values of the isovalent series we see similar patterns: the manganese and iron species are heavily spin contaminated, while the vanadium, chromium and cobalt species are slightly spin contaminated, and the rest experience almost no spin contamination with B3LYP. In an earlier study from our group[184], a stable biradical state was identified for $[Mn@Si_{12}]^{+}$, where the driving force to form this state is a local high-spin configuration at the Mn centre (five unpaired *d* electrons). It is very likely that we are seeing the same thing here: the spin contamination is caused by a tendency to adopt configurations where spin density is localised on the central metal. The problem is more prominent for manganese species because of the favourable half-filled d shell in Mn^{2+}.

3.3.2 Electronic structures of isomer A, B and C

In both isovalent series and isoelectronic series we see different behaviour for isomer A compared to isomer B and C when using different functionals. In terms

of their structure, isomer A is clearly a 'fullerene-like' isomer with characteristic 3-connected vertices while the other two are more on the side of deltahedral-type. While this seems to be an important clue for the functional dependency issue, it does not readily explain the parallel behaviour of isomers A and B for $Cr@Si_{14}$, nor does it explain how the stability of isomer B is apparently more reliant on the availability of metal *d*-electron density. In an attempt to understand the similarities and differences between these three isomers, we now look into their electronic structures individually.

Isomer A: the archetypal "fullerene-like" cluster

In the field of cluster chemistry, the term 'fullerene-like' is applied to clusters with a structural resemblance to the archetypal fullerene, C_{60}. More specifically, isomers are often referred to as 'fullerene-like' when they adopt endohedral structures with 3-connected vertices and pentagonal faces. However, adopting a 'fullerene-like' geometry does not necessarily indicate the adoption of a 'fullerene-like' electronic structure, as 3-connected vertices and pentagonal faces are also characteristics of electron-precise clusters. Typically, the electron count on each of the vertices of a fullerene is four, three of which participate in 2-centre-2-electron σ bonding with adjacent vertices and the last one is in the delocalised π system formed by linear combinations of the outwardly oriented orbitals perpendicular to the surface tangent. Therefore, for an electronically 'fullerene-like' silicon cluster, the total number of valence electrons should be 4n (n being the number of vertices), where 3n electrons occupy the 3n/2 cage σ orbitals and the rest fill the n/2 π orbitals. Correspondingly, there should be an equal number of antibonding orbitals. An electron-precise cluster with the same structure, on the other hand, has 5n total valence electrons. The n/2 empty π^* orbitals in the fullerene are now filled by the excess n electrons. Thus electron-precise clusters have the same cage σ frame-

work as fullerene clusters, but no π interaction. Instead, a lone pair of electrons is localised on each of the vertices. Some gave such clusters a name 'fullerane-like cluster' as they can be regarded as analogues to fullerane, but here I will stick to the name 'electron-precise cluster'. In the case of 14-vertex clusters, stable isomers with the same structure as M@Si_{14} isomer A have been identified for both 56-electron C_{14}[185] and 70-electron P_{14}[186] albeit neither isomer is the global minima. This indicates that isomer A is tolerant of a wide range of electron counts between 56 and 70. Should the Si_{14} cage be 'truely fullerene-like', it would have 7 π orbitals and 7 corresponding π* orbitals which are linear combinations of the radially directed silicon orbitals. If we examine the 7 lowest lying empty orbitals of the Si_{14} cage ($6a_1'$, $2a_2'$, $4a_2''$, 7e', 4e'') closely, all of them are combinations of radially directed silicon orbitals with π* character, so that they should correspond to the 7 π* orbtials in the fullerene-like model. In Cr@Si_{14}, where isomer A peaks in terms of relative stability, the six metal *d* electrons all participate in back-bonding interactions by populating three of these empty π* orbitals, 4e'' and $6a_1'$, of the Si_{14} fragment (see Figure 3.4). The populated π* orbitals localise mainly on the atoms in the polar regions of the cluster (labelled I and II in Figure 3.4), while the π* orbitals in the equatorial plane ($2a_2'$ and 7e') remain empty. This leads to shorter equatorial Si-Si bond lengths comparing to bonds in polar regions (2.30 Å *vs* 2.37 Å). In summary, the *d* electrons from the metal stabilise the cluster through a back-bonding interaction which is similar to the text book metal back-bonding interaction in $Cr(CO)_6$ compound. The formation of Cr-Si bonds is at the expense of a weakening of the silicon cage π system, and significant π bonding is maintained only in the equatorial plane. Therefore, the phrase 'fullerene-like' is a little misleading for M@Si_{14} clusters where the π system is never complete as it is in fullerenes. A closer inspection at the remaining four empty π* orbitals explains why the electron count of 62 (4n+6, n=14) is particularly stable. Amongst the four

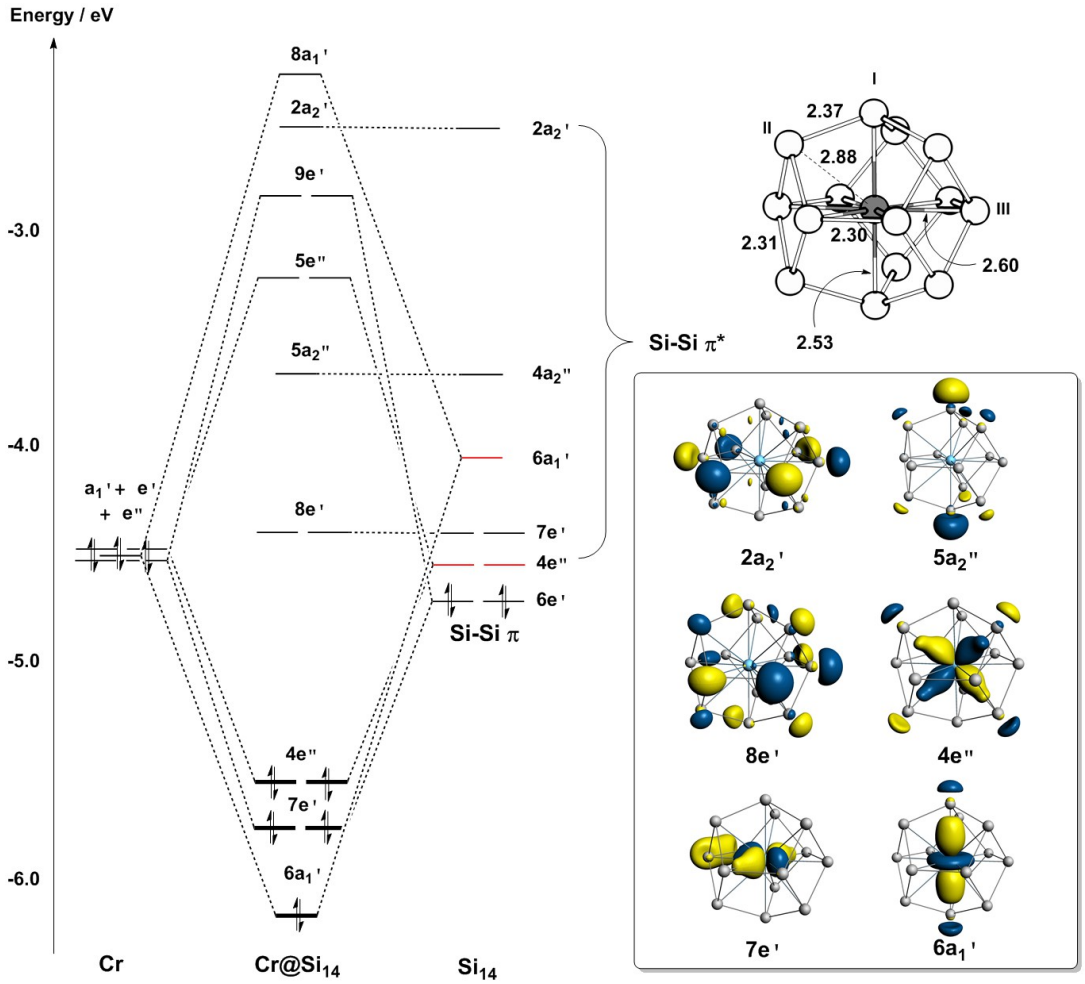


Figure 3.4: Kohn-Sham orbitals for isomer A of $Cr@Si_{14}$

orbtials, $2a_2'$ and $4a_2''$ lack the matching symmetry with metal d orbitals (which are in a_1', e' and e" symmetry) and thus by occupying these orbitals, the cluster would lose π bonding with no compensation from the strengthening of the Cr-Si bonds. The 7e' orbital could, in principle, accept electron density from metal $d_{xy}/d_{x^2-y^2}$ orbitals, but the destabilising interaction with the occupied 6e' (7e' in $Cr@Si_{14}$) orbital would be strong.

Isomer B: an archetypal "*arachno*" cluster

We have noted in previous sections that the high vertex connectivity of isomer B indicates electron deficiency within the Wade's rules bonding paradigm, devel-

oped in the context of electron deficient boranes. Just like isomer A, the relative stability of isomer B also peaks around $Cr@Si_{14}$, where the formal valence electron count is 62. According to Wade's rules, for a 14-vertex cluster, 62 (4n+6, n=14) is the ideal electron count for an *arachno*-architecture and indeed, isomer B has two open faces which is a structural characteristic of *arachno* clusters. We therefore tried looking for the parent 16-vertex *closo* polyhedron from which isomer B can be derived, and found a D_{4d}-symmetric octa-capped square antiprismatic structure predicted by von Ragué Schleyer *et al*.[187] to be the ground state for the (unknown) borane $[B_{16}H_{16}]^{2-}$. In our calculations, this D_{4d}-symmetric *closo* structure is a stable minimum for the isoelectronic $[Si_{16}]^{2-}$, irrespective of the chosen functional. Moreover, the similarity between the frontier orbitals of the *closo*-$[Si_{16}]^{2-}$ cluster, the corresponding *arachno*-$[Si_{14}]^{6-}$ and isomer B of $Cr@Si_{14}$ indicates an isolobal relationship between these three clusters (shown in Figure 3.5), which supports our argument that isomer B of $M@Si_{14}$ could be post-rationalised as an *arachno* cluster. To examine the interaction between the central metal and the cage, we again look into the Kohn-Sham orbitals of isomer B. As shown in Figure 3.5, the HOMO-LUMO gap of the neutral empty Si_{14} cage is very narrow, and the three lowest-lying vacant orbitals $8b_1$, $7b_2$ and $5a_2$ are closely spaced. This suggests immediately a first-order description of the cluster stable as $[Si_{14}]^{6-}$ instead of Si_{14}. The $8b_1$, $7b_2$ and $5a_2$ orbitals are stabilised in $Cr@Si_{14}$ by bonding interactions with the metal *d* orbitals, and the resulting $8b_1$, $8b_2$ and $4a_2$ orbitals of $Cr@Si_{14}$ have both cage bonding character and Cr-Si bonding character. The former can be easily observed from the shape of $Cr@Si_{14}$ orbitals, while the latter is better appreciated by looking at the corresponding $[Si_{14}]^{6-}$ orbitals, where the in-phase relationship between the neighbouring Si atoms is more obvious. The electrons in these orbitals, together with those in $10a_1$ and $11a_1$, play a dual role by contributing to both the 18-electron count of the metal and to the 4n+6 electron count of the *arachno* cluster.

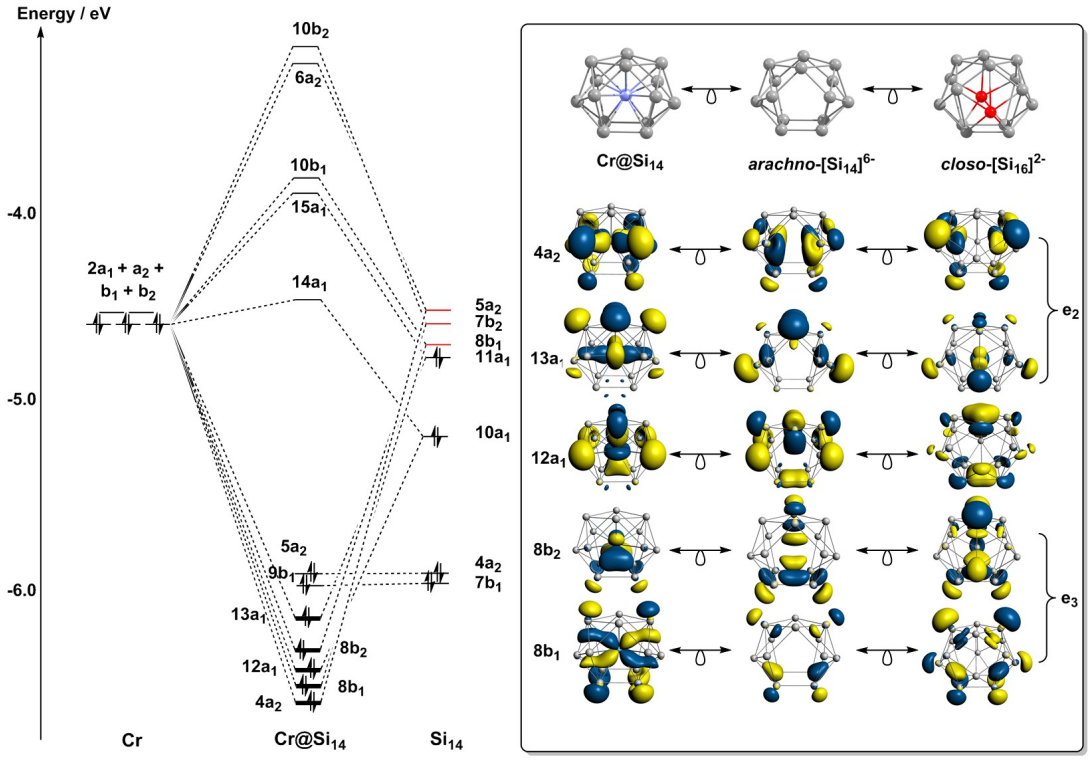


Figure 3.5: Kohn-Sham orbitals for isomer B of $Cr@Si_{14}$ (left), and the isolobal relationship between $Cr@Si_{14}$, *arachno*-$[Si_{14}]^{6-}$ and *closo*-$[Si_{16}]^{2-}$ (right)

Therefore, it is clear that isomer B is uniquely tailored to accommodate precisely 62 valence electrons, and that the 6 electrons from the metal are crucial to its stability. Unlike isomer A, where the electrons from the metal do not participate in the cage σ framework, and where without the metal *d*-electrons the electronic structure of the cage make sense on its own, in isomer B, the electrons from the metal complete the essential electron count of the cage framework. The dual role of the metal *d* electrons can only be fulfilled when the *d* orbitals have good overlap with the cage orbitals. That is to say, when the *d* orbitals contract to become more compact, the stability of isomer B is compromised. This explains why the stability of isomer B is more dependent on the charge in the isoelectronic series than isomer A, where the *d* electrons play a less integral role in the cluster's stability.

Isomer C: an archetypal "*closo*" cluster

Since isomer C was predicted by Kumar and Kawazoe to be the most stable isomer for $Fe@Si_{14}$[46], the stability of this isomer has been discussed in many subsequent papers, most notably by Khanna *et al*. who considered in detail the relationship between geometry and stability[112]. Here, we focus on the electronic structure of isomer C, and try to understand its stability in the context of existing bonding paradigms, consistent with how we analysed isomer A and B. The high vertex connectivity characteristic of isomer C is again suggestive of an electron-deficient configuration. A reference cluster can be found in the work of King and co-workers[188], where the same octahedral isomer was identified as the global minimum for $[Ge_{14}]^{2-}$. The total valence electron count in this 14-vertex germanium cluster is 58, which fits the classic 4n+2 electron count for *closo* clusters according to Wade's rules. Indeed, aside from the fact that the triangular faces in isomer C are far from equilateral, isomer C possesses almost all the characteristics of a *closo* structure: all vertices are either 4 or 5-connected, all vertices are in

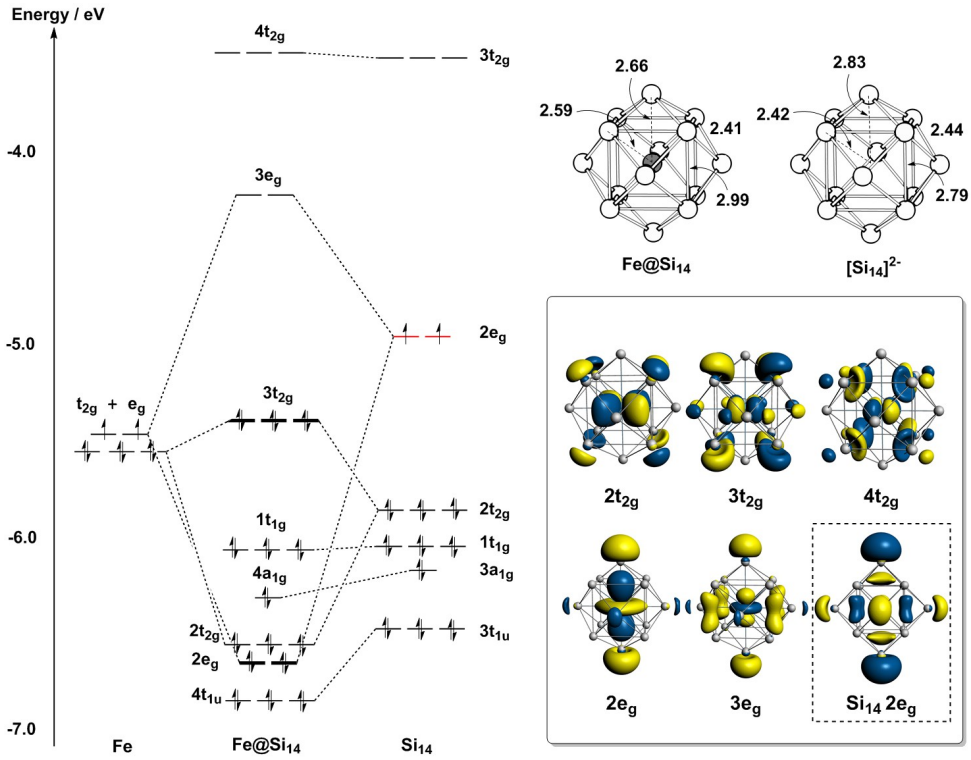


Figure 3.6: Kohn-Sham orbitals for isomer C of $Fe@Si_{14}$

a near spherical arrangement with respect to the cluster centre, and there are no 'open faces'. If it is true that isomer C can be considered as a Wade's rules *closo* isomer, for the relatively more stable $Fe@Si_{14}$ cluster, the central atom must then contribute two electrons to the cage bonding system, and not all eight available on an Fe atom. This is exactly the situation in the Kohn-sham MO diagram in Figure 3.6. As shown in Figure 3.6, the $2e_g$ orbital of the octahedral Si_{14} cage is the last cage bonding orbital that needs to be fully filled to reach a 4n+2 electron count. In $Fe@Si_{14}$, by interacting with metal *d* orbitals in the same symmetry, this orbital now becomes the fully filled $2e_g$ orbital with substantial Fe-Si bonding character. The electrons in this orbital therefore play a similar dual role as the electrons in the $8b_1$, $8b_2$ and $4a_2$ orbitals of isomer B, contributing to both the stability of the cage framework and the central metal. The remaining six electrons, on the other hand, are excessive, at least from the cage's perspective, and the $3t_{2g}$ orbital is antibond-

ing in nature , and in effect it cancels out the Fe-Si bonding character of $2t_{2g}$ orbital. The antibonding interaction between metal d_{xy}, d_{xz} and d_{yz} orbitals is reflected in a comparison of the structural parameters of the optimised Fe@Si_{14} and $[Si_{14}]^{2-}$ cages: the distances between the centre and the Si atoms lying along the 3-fold rotation axes become longer when the metal is encapsulated, while the distances between the centre and Si atoms along 4-fold rotation axes becomes shorter due to bonding interactions between the cage and metal d_{z^2/x^2-y^2} electrons.

The difference in preferred electron count between isomer C (56) and isomer A/B (62) accounts for the relative stability of isomer C both at the start and at the end of the period. Early in the series this is simply because there are fewer electrons while at the end, although the *d* electrons are more numerous, they descend into core and become less available. In the same context, the fact that the energies of isomers A and B lie in parallel relative to isomer C is very possibly due to that they share the same optimum electron count. We also note that in the plots for the isoelectronic series, the curves of isomer A are parabolic, indicating that its stability relative to isomer C increases for both high negative and high positive charges. The reason is not obvious if we examine the stability of isomer A alone, for we expect that the stability of isomer A will always decrease when the cluster becomes more negative and the *d* electrons becomes less available. The stability of isomer C, however, is expected to have a more complicated relationship with the availability of the metal *d* electrons as there are two competing factors: while the contraction of the metal *d* orbitals would certainly hinder the electrons in the $2e_g$ orbital from fulfilling their role in completing the 4n+2 count at the cage, it will also reduce the antibonding character of the $3t_{2g}$ orbital. Thus, it is reasonable to infer that the parabolic behaviour of the curves for isomer A is actually caused by the complex stability changes of isomer C, where some of the metal *d* electrons are bonding and some are antibonding.

3.3.3 Relationship between the two bonding paradigms and possible sources of functional dependency

So far, we have analysed the electronic structure of isomers A-C and were able to explain the stability trend seen in isovalent and isoelectronic $[M@Si_{14}]^z$ series in terms of differences in electron count and metal-cage interaction. What we have not established is the origin of the functional dependency seen in these systems. In this section, I compare the 'fullerene-like' isomer A with 'electron-deficient' isomer B/C, and try to understand the systematic relative energy shift when switching to B3LYP/BLYP from PBE.

We noted that 'fullerene-like' and 'Wade's rule electron deficient' paradigms of cluster bonding usually apply to very different families of clusters. The former is seen mostly in carbon clusters while the latter mainly applies to boranes, and they rarely overlap. However, despite the significant differences between these two bonding paradigms, they can actually be related to a common reference point, which is the 'electron precise' (or 'fullerane-like') paradigm. As mentioned in the section where we discussed the electronic structure of isomer A, an n-vertex 'electron precise' cluster would have in total 5n valence electrons, 3n of which participate in the cage σ bonding, where all the bonds are well-defined two-centre-two-electron (2c-2e) bonds between adjacent atoms, and the other 2n constitute lone-pair electrons on each vertices. To accommodate a lower electron count, electrons in the lone pairs are removed in the 'fullerene route' to generate π bonds while the σ framework is left intact. On the other hand, when following the Wade's rules route, the lone pairs are left alone and fewer electrons are used for cage bonding. The decrease in cage bonding electron leads to the formation of triangular faces and high vertex connectivity, which is the structural fingerprint of electron-deficiency. In terms of the type of bonding, multi-centred electron bonds construct

the cage framework in electron deficient deltahedral clusters, and compared to classic 2c-2e frameworks the electron densities are more delocalised and lower in general. A schematic comparison of the two routes is shown in Figure 3.7, where the 14-vertex clusters are taken as examples. It should be noted that even though the image of an M@Si_{14} isomer A was used to represent the fullerene-like cluster, a truly 'fullerene configuration' is never met for any M@Si_{14} in our study. For simplicity, the lone pair (or π) orbital bands are well separated from the cage framework bands in the figure, although in reality there would be inevitable overlap. In large carbon clusters C_n (n>20), the good 2p-2p overlap and the low surface curvature combine to stabilise the π bonding orbitals, making the fullerene solution favourable. In boranes, in contrast, it is extremely difficult to depopulate the radial orbitals because they are B-H bonding orbitals instead of lone pairs. As a result, electrons can only be removed from the cage σ framework, forcing the system to follow the Wade's rules route. The endohedral tetrel clusters appear to be rare intermediate cases where the two bonding paradigms collide, creating situations where isomers from the two routes compete with each other, giving rise to functional dependency issues. There are several differences between the 'fullerene-like' clusters and the 'Wade's rules' clusters that could possibly lead to the functional dependence issue we are seeing. Originally, we suspected the problem was with the different treatments of central transition metal, since the absence of a radial node in 3*d* orbitals amplifies the electron-repulsions, and therefore, amplifies any inaccuracy in their treatment. In Wade's rules clusters isomer B and C, metal *d* electrons are integral parts of the cage framework while in fullerene-like isomer A, metal *d* electrons back-bond to cage π^* orbitals. Clearly, the role of metal *d* electrons is different in these two types of clusters. We noticed that the change of functional from PBE to B3LYP replicates the effect of increasing positive charge in the isoelectronic series: both destabilise isomer B with respect to isomer A and C,

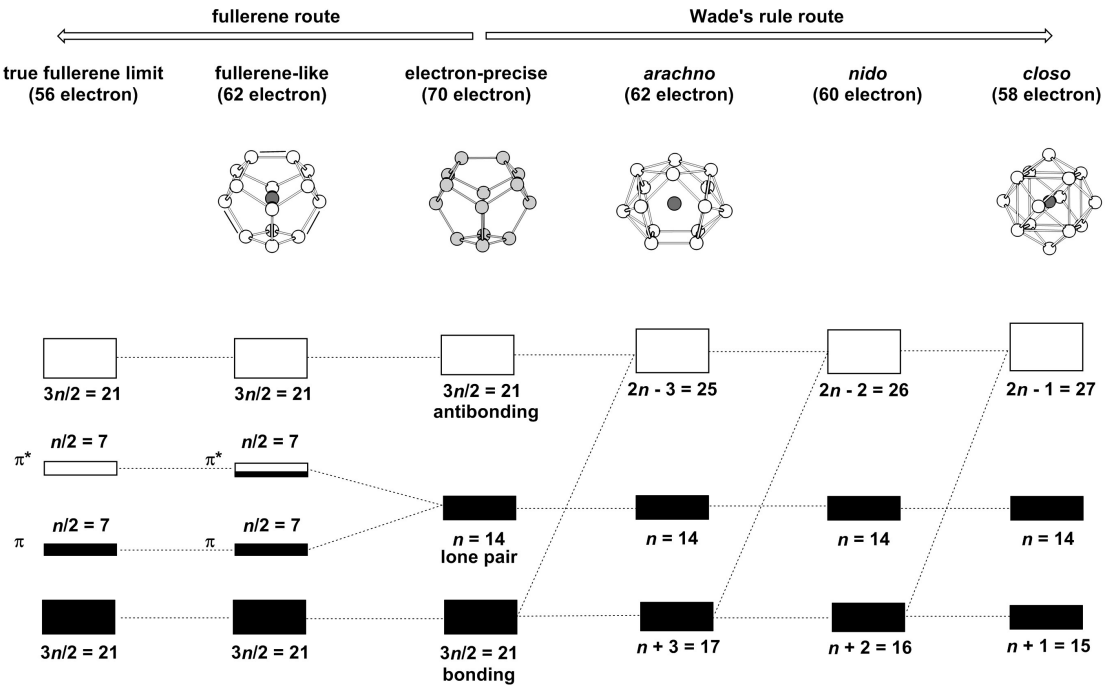


Figure 3.7: Schematic representation of the fullerene-like and Wade's rules routes to accommodating electron deficiency in 14-vertex clusters. The numbers below each band indicate the number of orbitals

from which we inferred that B3LYP makes the electron density on the metal less available to the silicon cage. It is difficult to quantify the 'availability' of electron density, but we can take the C-O stretching frequency of metal carbonyls which is strongly dependent on back bonding, as a convenient parameter. It is striking that the computed frequency of the totally-symmetric C-O stretch of $Cr(CO)_6$ is 2081 cm^{-1} in PBE, which is almost 100 cm^{-1} lower than the 2161 cm^{-1} calculated by B3LYP. However, the totally symmetric C-O stretch is 2068 cm^{-1} in BLYP, which is even lower than PBE. Should the availability of metal *d* be the only factor that controls the relative energy, the relative stability with BLYP should resemble of PBE, not B3LYP. Therefore, it is either that the treatment of metal *d* orbitals is not the main source of the functional dependency problem, or it is affecting the system in a more complicated way.

Aside from the different roles of the central metal, the differences in silicon cage

themselves can possibly give rise to the pathological dependence on methodologies. There are two major differences regarding the fullerene-like and Wade's rules clusters. First, the fullerene-like clusters have residual π interactions between the silicon atoms while the Wade's rules clusters do not. Second, the cage framework of the Wade's rules clusters is constructed by electron-deficient-multicentre-bonds, unlike the fullerene-like clusters where only 2c-2e bonds are involved. Since for C_{14}, isomer A is much higher in energy than the global minimum, which is the monocyclic ring, the stabilisation effect of possible π interaction in isomer A must have been less important than the stability of the cage σ framework. The question now becomes whether the LYP functional (or the PBE functional) is particularly problematic at describing multi-center bonds or electron-deficient systems. Fan and Schaefer's computational study[189] on small Ag_n clusters ($n \leq 4$) provides us some inspirations on this matter. Twenty-three functionals were used to calculate the properties of neutral and ionic silver clusters in Fan and Schaefer's study and almost all functionals incorporating the LYP correlation functional failed to qualitatively predict the correct structure for Ag_3 and $[Ag_4]^-$ clusters calculated with high-level theoretical methods. The reason lies within the stability change of electrons in different frontier orbitals. In Figure 3.8, we present a schematic picture of the Walsh diagram for the $^2B_2$ state of Ag_3 calculated in Fan and Schaefer's study. The two orbitals $3b_2$ and $3a_1$ shown in Figure 3.8 are the two highest lying occupied orbitals in the neutral Ag_3 cluster, the former being half-filled. In $[Ag_3]^+$, only $3a_1$ would be populated, thus the cluster undoubtedly adopts a triangular configuration very similar to trihydrogen cation, which is the simplest example of a three-center-two-electron (3c-2e) bonded system. In the anion $[Ag_3]^-$, both $3b_2$ and $3a_1$ would be fully occupied, and the cluster would adopt a near linear structure, stabilised by two 2c-2e bonds, independent of functional. CCSD(T) calculations predict a global minimum with an acute Ag-Ag-Ag angle (~70°) for neutral

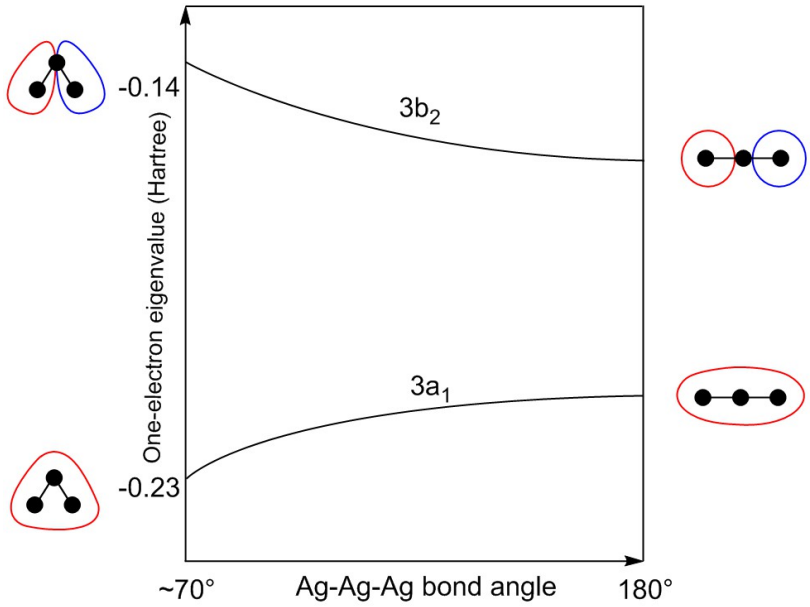


Figure 3.8: Schematic Walsh diagram for the $^2B_2$ state of Ag_3 along with sketches for the orbitals $3b_2$ and $3a_1$

Ag_3, which most of the functionals with LYP correlation functional failed to capture. The LYP functionals find only one minimum on the potential energy surface, with an angle of ~140°. Thus, we can infer that the balance between the triangular structure and the near linear structure reflects the competition between delocalised 3c-2e interaction and the localised 2c-2e interaction, and that LYP functionals tends to underestimate the stability of the former (or overestimate the stability of the latter). The story is similar for the $[Ag_4]^-$ cluster as the LYP functionals favours a linear structure while high-level calculations suggests a rhombic structure.

In fact, it is shown in Fan and Schaefer's study that the problem is not limited to LYP functionals but nearly all functionals that do not conform to the uniform electron gas (UEG) limit. As noted in Chapter 2 LYP, unlike PBE, PW91, or P86, was not designed to reproduce the LDA correlation energy at the UEG limit. Kurth, Perdew and Blaha's[190] showed that the exchange-correlation energy calculated by BLYP is higher than the exact exchange-correlation energy at the UEG limit for both unpolarised and fully spin polarised systems, and that the performance of

LYP correlation functional is not ideal for jellium surfaces. Therefore, a reasonable explanation for the failure of LYP functionals to locate the minimum for Ag_3 and $[Ag_4]^-$ is that the electrons in the 3c-2e bonding configuration resembles a UEG more closely compared to a 2c-2e bonding configuration, and so that LYP underestimate the stability of the former. There are several other cases where the LYP functional and/or other correlation functionals that do not obey the UEG limit behave problematically. For example, LYP failed in finding the agostic minima for Niobium complex[191], while B3LYP and BLYP also underestimate the stability of B_{20} clusters with more spherical structures but reproduce the CCSD(T) results closely for planar and tubular isomers[192]. It appears that LYP disfavours situations where electron densities are shared between more atoms, or arranged in a more spherical way. Even though we cannot fully exclude influences from other factors, it is very likely that we are seeing the same problem in our endohedral tetrel cluster systems. The last thing worth mentioning here is that in the study by Fan and Schaefer, O3LYP was shown to be the one exception of the LYP functionals family that qualitatively agrees with other functionals such as PBE instead of other LYP functional. Calculations on the $Cr@Si_{14}$ systems with O3LYP are qualitatively consistent with PBE rather than B3LYP and BLYP, as shown in Table 3.2. In summary, the literature suggests that the LYP functional (except for O3LYP, somehow) will systematically underestimate the stability of the deltahedral cages relative to their fullerene counterparts. Whilst our analysis above reveals why the LYP functionals is potentially problematic, it has not brought us closer to an answer to the question of which isomer is in fact the global minimum. It does, however, highlight the important point that functional roulette is a dangerous game in the $M@Si_{14}$ family.

$Cr@Si_{14}$	Isomer A	Isomer B	Isomer C
BP86	0	-0.013	0.839
PBE	0	-0.270	0.624
PBE0	0	-0.076	0.355
BLYP	0	0.483	1.328
B3LYP	0	0.614	1.113
O3LYP	0	-0.394	0.350

Table 3.2: Relative energies in electron volt of isomer A, B and C for $Cr@Si_{14}$ obtained by different functionals, with the energy of isomer A set to zero

3.4 Post Hartree-Fock calculations

In light of the uncertainty regarding the correct choice of functional, I now turn to post HF calculations for isomer A and isomer B, hoping to provide a benchmark for DFT calculations and determine the ground-state structure for $Cr@Si_{14}$ cluster. CCSD(T) results will be reported, followed by CASPT2 results, along with a discussion of the strength and weaknesses of both.

3.4.1 CCSD(T) results

Table 3.3 summarizes our Coupled-Cluster calculation results. As shown in the table, Isomer A is marginally more stable than isomer B for both $Cr@Si_{14}$ and $[Mn@Si_{14}]^+$ species at the CCSD level, but the perturbative triple excitation correction is large in both cases. For $Cr@Si_{14}$, the triples correction tips the balance towards isomer B and the final CCSD(T) energy indicates that isomer B is in fact more stable than isomer A. For isoelectronic $[Mn@Si_{14}]^+$, however, the correction further enlarges the energy gap between isomer A and B, making isomer A significantly more stable than isomer B. The basis set limit energy calculated by applying the two point extrapolation method to DLPNO-CCSD(T) agrees with the CCSD(T) result in that isomer B should be the ground state structure for $Cr@Si_{14}$

Cr@Si$_{14}$	Isomer A	Isomer B	$\Delta E_{(A-B)}$
E_{CCSD}	-5090.1982 a.u	-5090.1898 a.u.	-0.23 eV
$E_{CCSD(T)}$	-5090.4615 a.u.	-5090.4737 a.u.	0.33 eV
DLPNO $E_{3/4_extrapolation}$	-5090.6510 a.u.	-5090.6451 a.u.	0.16 eV
T_1 diagnostic	0.084	0.089	
Largest T_2	<0.066	<0.087	
[Mn@Si$_{14}$]$^+$	Isomer A	Isomer B	$\Delta E_{(A-B)}$
E_{CCSD}	-5196.4382 a.u.	-5196.4264 a.u.	-0.32 eV
$E_{CCSD(T)}$	-5196.7447 a.u.	-5196.7049 a.u.	-1.08 eV
T_1 diagnostic	0.036	0.101	
Largest T_2	0.091	<0.089	

Table 3.3: CCSD(T) results for M@Si$_{14}$ (isomer A and isomer B) using a cc-pVTZ basis set: the upper part is for Cr@Si$_{14}$ and the lower part is for isoelectronic [Mn@Si$_{14}$]$^+$, and DLPNO CCSD(T) cc-pVTZ/cc-pVQZ basis set extrapolation result for Cr@Si$_{14}$.

although the energy gap between the two isomers is small. Though qualitatively, the CCSD(T) results are in agreement with results calculated with PBE functional, which assigned isomer B and isomer A as the ground state structures of $Cr@Si_{14}$ and $[Mn@Si_{14}]^+$, respectively, the different behaviour of the perturbation triple excitation correction in $Cr@Si_{14}$ and $[Mn@Si_{14}]^+$ is alarming. A reasonable concern is that both species, especially $[Mn@Si_{14}]^+$, might have multiconfigurational character, which will challenge the reliability of CCSD(T) method. We have mentioned in Chapter 2 that the coupled-cluster method is only valid when there is no significant multireference character in the calculated system, yet there is no standardized method to determine how 'multiconfigurational' a system is, nor is there a clear threshold for the CCSD(T) method's tolerance. In the absence of experimental data, to judge whether CCSD(T) is a valid method for a specific system, one can check three criteria: (a) how easily the CC convergence is reached; (b) the T_1 diagnostic and (c) the largest T_2 amplitude. A difficult convergence, a T_1 diagnostic larger than 0.05 and large T_2 amplitudes usually indicate a multiconfigurational system, although one cannot draw definitive conclusions according to these criteria[193–195]. In our systems, for example, the $Cr@Si_{14}$ clusters are easy to converge and have reasonable T_2 amplitudes. However, the T_1 diagnostics are larger than the 0.05 threshold. The two isomers of $[Mn@Si_{14}]^+$ have significant differences in their T_1 diagnostics: isomer A has a T_1 diagnostic smaller than 0.05, but the T_1 diagnostic of isomer B is ~0.1. Some believe that the largest T_2 amplitude is a more direct and more valid criterion than T_1 diagnostic since a proper description of a multireference system usually requires double and higher excitations. Nevertheless, it is difficult to draw conclusions when not all three criteria are met. To conclude, although qualitatively, our CCSD(T) calculations agree with our DFT calculations done with PBE, the T_1 diagnostic raises some concerns over the validity of this method.

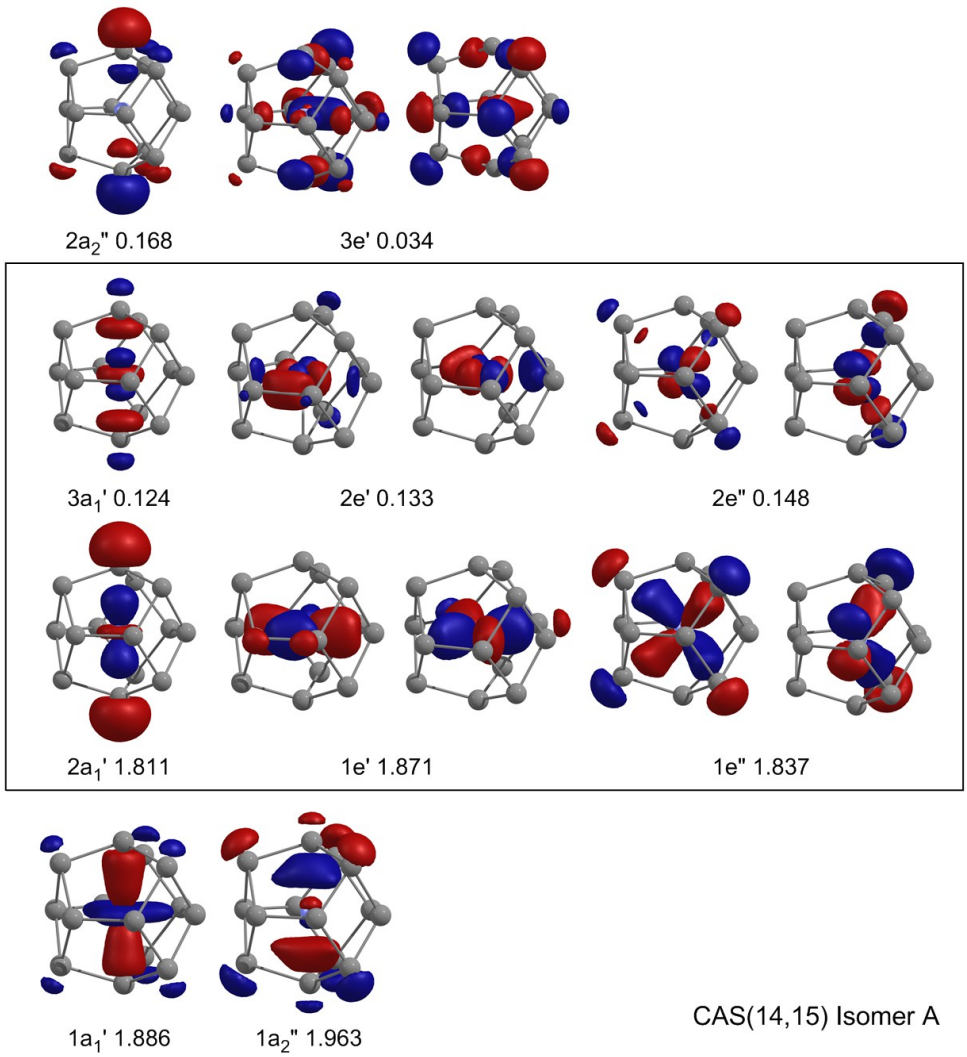


Figure 3.9: Natural CASSCF(14,15) active space for $^1A_1'$ ground state of $Cr@Si_{14}$ isomer A. Orbitals in the box are included in the (10, 10) active space

3.4.2 CASSCF and CASPT2 results

In light of the potential multiconfigurational character of the $Cr@Si_{14}$ systems, we attempted to find an alternate solution to the problem using CAS calculations. We first did CASPT2 calculations based on a CAS(10, 10) wave functions, consisting of ten bonding and antibonding MOs between metal *d* orbtials and the cage orbitals. At the CASSCF level, isomer A is about 1.50 eV more stable than isomer B, while at the CASPT2 level, isomer A is about 2.18 eV less stable. Again, we

see large perturbation corrections that tip the balance between the two isomers just like we did with the CCSD(T) calculations. The huge difference in the result suggests possibly inadequate active spaces or unbalanced treatment for the two isomers. We then expanded our active space to (14, 15). The active orbitals are shown in Figure 3.9 and 3.10. For isomer A, two additional occupied orbitals a_1', a_2'' and three empty orbitals a_2'', e' (drawn outside the box in Figure 3.9) are included, just as they were in the $[Mn@Si_{14}]^+$ study[196] done by Ngan *et al*. All of the extra orbitals added in are silicon based orbitals, except for the a_1' orbital, which has a significant metal d_{z^2} components. In Ngan's study, the extra e' orbitals are necessary in the active space because they are singly occupied in the triplet states of interest in that study. Thus for our singlet system they seem to be less important, but their occupation numbers are larger than 0.02, so they are retained in the active space. As shown in Figure 3.9, the occupation of the metal-cage bonding-antibonding pairs all add up to be approximately 2.00 except for the d_{z^2} pair. Judging by the occupation number, the bonding-antibonding cage-metal d_{z^2} orbital pairs should be correlating with the empty cage-based a_2'' and occupied d_{z^2}-cage bonding a_1' orbitals added into the active space. The correlation between cage-based orbitals and orbitals that have a prominent metal d component indicates the existence of static-correlation in the system. However, aside from the singlet ground state configuration which has a dominant weight of 0.639, no other configuration has a weight larger than 0.015. The next two configurations with largest weight (and CI-coefficient) are those where two electrons are taken out of the cage-metal $d_{xz/yz}$ bonding orbitals and put into the corresponding antibonding orbitals. The result of calculation shows that whilst the Hartree-Fock configuration (similar to that shown in Figure 3.4) contributed to only 64% of the total wave function, there is no specific doubly excited configurations that dominate the static correlation, and that dynamic correlation is very possibly the dominant correlation

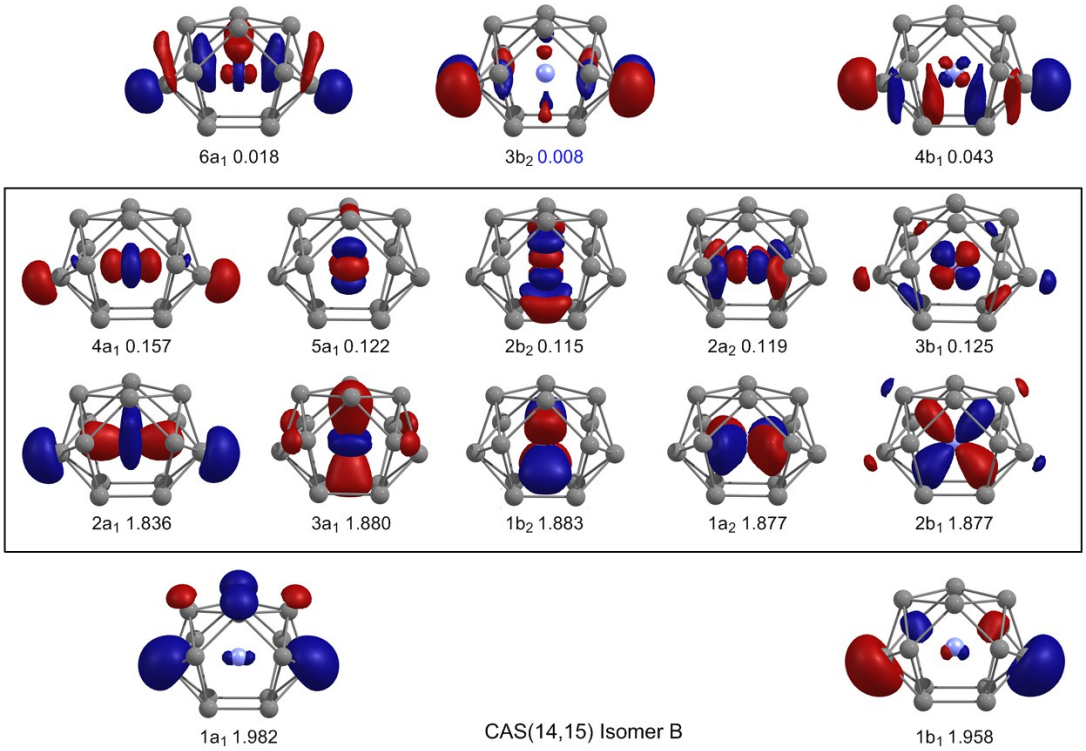


Figure 3.10: Natural CASSCF(14,15) active space for the $^1A_1'$ ground state of $Cr@Si_{14}$ isomer B. Orbitals in the box are included in the (10, 10) active space

in our studied system. Unfortunately, attempts to find an equivalent active space in isomer B have not been successful. In order to compare the two isomers, we did CASSCF/CASPT2 calculations with a (14,15) active space for isomer B as well. The CASSCF(14,15) active space for $^1A_1'$ ground state is shown in Figure 3.10. Aside from the clearly correlated metal-cage bonding-antibonding pairs, the correlation between cage orbitals (outside the box) should also be considered. The occupation numbers of $1b_1$ and $4b_1$, which are mainly cage orbitals, deviate noticeably from 2.00 and 0.00. Also, judging from the occupation number, it is better not to exclude $1a_1$ and $6a_1$ from the active space. If we want to have a balanced active space, we would need to take all the cage-based orbitals matters into consideration, which is going to be too demanding for a CASSCF calculation. Moreover, even if we succeeded in taking all the important correlations in the cage based orbitals into account using generalised active space self-consistent field (GASSCF) method, we

still face the problem of getting an equivalent active space for isomer A. The problem we face here is not uncommon. Pierloot, Cramer and co-workers[197, 198] have expressed similar concerns in their studies on $Cu(O_2)Cu$ systems. Namely, they suggested that it is nearly impossible to calculate and compare the energy of the $\mu - \eta^2$: η^2 peroxo isomer and the bis(μ-oxo) isomer on an equal footing using the CASPT2 method, and that the problem can be only alleviated when a restricted active space self-consistent field wave function method is applied to include all valence electrons originating from occupied Cu $3d$ and O $2p$ atomic orbitals. The problem with the two $Cu(O_2)Cu$ isomers is that static correlation clearly plays a more important role in the $\mu - \eta^2$: η^2 peroxo isomer due to its biradical nature, while the bis(μ-oxo) isomer has much less biradical character but more dynamic correlation. In our case, the CASPT2 calculations based on the CAS(14,15) wavefunctions show that the perturbation correction in isomer B is about 5 eV larger than in isomer A, and the difference mainly comes from configurations where two electrons in the inactive orbitals are excited to virtual orbitals. This is indicative of more important correlations between the cage orbitals in isomer B than in isomer A, which is not that surprising considering the cages in the two isomers are constructed by bonds with fundamentally different bonding nature.

In summary, we have been unable to identify a satisfactory active space that treat both isomers in a balanced way, preventing us from assessing the relative energies of isomer A and B with CASSCF/CASPT2 methods.

3.5 From $[M@Si_{14}]^z$ to other endohedral clusters with a single metal

We can now collect the results from the literature and our own study to make a figure for the structural landscape of $[M@Si_{14}]^z$ clusters, just as we did for clusters of

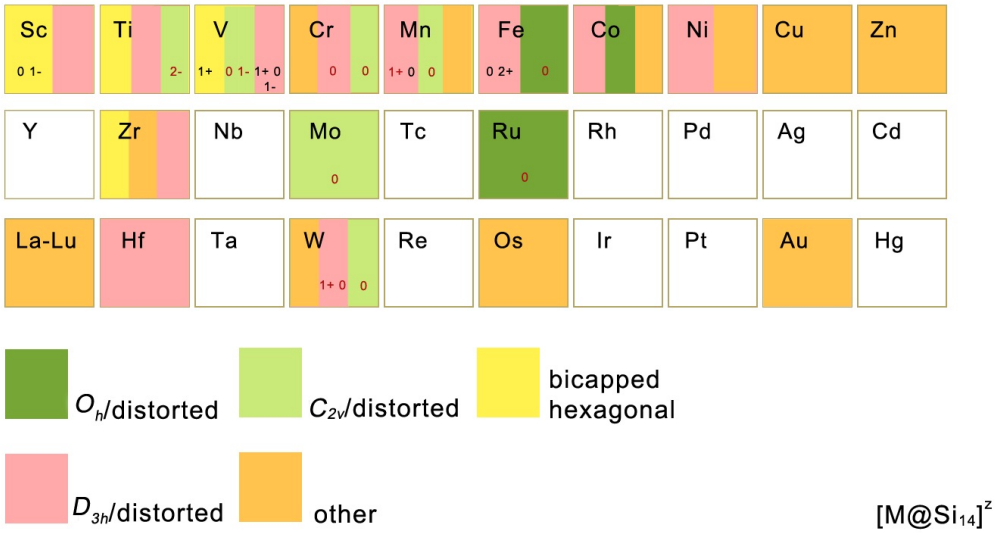


Figure 3.11: Theoretical predictions of equilibrium structures for $[M@Si_{14}]^z$ clusters. The numbers inside the blocks represent the charge number z of the cluster[44, 46–48, 88–99, 101–103, 107, 109–112, 119, 123, 124, 196, 199, 200]

different stoichiometry in Chapter 1. Compared to the figures in Chapter 1, Figure 3.11 shows the greatest number of conflicting results by far. Nevertheless, it has many common features with the others that make $[M@Si_{14}]^z$ clusters fit into the big picture of single metal encapsulating tetrel clusters nicely. Overall, for all endohedral clusters, there is a competition between two bonding paradigms. One is the Wade's rule route, where clusters have electron-deficient cages constructed by multicenter-electron-bonds and lone pair electrons which structurally give triangular faces and highly connected vertices. The other is the fullerene route, where the cage σ framework contains only classic 2c-2e bonds and the cage is further stabilised by π interactions. Both routes provide various structures capable of accommodating different number of total valence electrons. In the Wade's rules route, a *closo* structure is ideal for clusters with 4n+2 electron count, n being the number of vertices. As the cluster accumulates more valence electrons, the optimal isomer becomes *nido*, then *arachno*, with more open faces, just like in boranes. In the fullerene route, a 'fullerene-like' structure with three-connected vertices and

pentagonal faces is tolerant of a wide electron count, from 4n to 5n. Due to the difference in nature between the heavier tetrels and carbon and the small size of these clusters, the overlaps between the p orbitals are never ideal, thus the true 'fullerene' limit is never reached. Because the global π interaction is weak in these clusters, the more spherical arrangement can be abandoned in favour of structures that maximise the effectiveness of 'local' π interactions (the π bonding will accumulate in regions with less curvature) and as the number of total valence electrons increases, the spherical arrangement can be recovered. The balance between the two routes is affected by the type of tetrel element, the total number of valence electrons, the central metal and the size of the cage. The effect of using different tetrel elements is the most obvious: the increasing stability of the ns^2np^2 configuration over ns^1np^3 down group 14 leads to the favouring of Wade's rule clusters, as the radial lone pair gets stabilised (more BH bond-like). From the total number of valance electrons, one can then infer the most stable structure. For Wade's rules clusters, an increase in the total valence electron number stabilises structures with more open faces and for the clusters on the 'fullerene-like' route, the increase will make the 'spherical' structures more favourable as the clusters becomes more 'electron-precise'. However, there are two conditions that need to be fulfilled in order for the above statement to make sense. The first is, the metal d orbitals have to be in matching symmetry with the energetically adjacent empty cage orbitals, so that the 'total valence electron count' truly is the 'total valence cage electron count'. The second is that the metal d orbitals must not be too contracted, so that there will be an effective electron sharing between the metal and the cage. The latter condition is controlled by both the central metal type and the cage, so to see the influence of total valence electron number, the easiest way is to compare the clusters $[M@E_n]^z$ with different charge number when all other conditions are the same. In addition, the fullerene-like structures are generally tolerant of a wider

range of electron count comparing to any specific Wade's rules structure.

The relative energies of Wade's rules isomers and fullerene-like isomers is always functional dependent, but the problem only results in different claims for the ground-state structure for $[M@Si_n]^z$ and $[M@Ge_n]^z$ clusters with moderate size and early to mid-period transition metals, where the Wade's rules isomer comes very close in energy to the fullerene-like alternatives. Examples include the $Cr@Si_{14}$, $Fe@Si_{14}$ and $Ti@Si_{16}$ ($[Sc@Si_{16}]^-$, $[V@Si_{16}]^+$) clusters. The competition between the D_{6h} and D_{6d} isomers for $[M@Ge_{12}]^z$ clusters is potentially a competition between fullerene-like and *arachno-* configurations as well. To further explore the issue of functional dependency, I have calculated the energies of various isomers of $Ti@Si_{16}$ using different functionals (Table 3.4). The potential energy landscape of the $M@Si_{16}$ family is reviewed in Chapter 1, and thus will not be repeatedly discussed here. Instead, the focus is solely on the relative energies of different $Ti@Si_{16}$ isomers when different functionals are applied. Aside from the Frank-Kasper structure and the D_{4d}-symmetric fullerene-like structure reported in literatures, we also included a D_{4d}-symmetric '*closo-*' and a C_{5v}-symmetric '*nido-*' structure for comparison. The '*closo-*' structure is predicted to be the structure of $[B_{16}H_{16}]^{2-}$[187] by von Ragué Schleyer *et al.*, while a distorted version has been reported to be the ground state isomer for $[Sc@Si_{16}]^-$ and $[Ti@Si_{16}]^-$ in Torres's[107] and Khanna's[105] papers, respectively. We labelled this structure as D_{4d}-'*closo-*' just to distinguish it with the D_{4d}-fullerene-like structure, although we are aware that it is arguable that this is a truly *closo* structure. The structures are shown in Figure 3.12. All isomers in Table 3.4 except for the *closo-* have small imaginary frequencies, indicating they can distort to minima with lower symmetry. All of the four isomers have a substantial HOMO-LUMO separation for $Ti@Si_{16}$, but beyond Ti, for $M@Si_{16}$ (M=V-Fe) the HOMO-LUMO gap is much smaller, indicating that the group 4 metals with an electron count of 68 are particularly suited for the

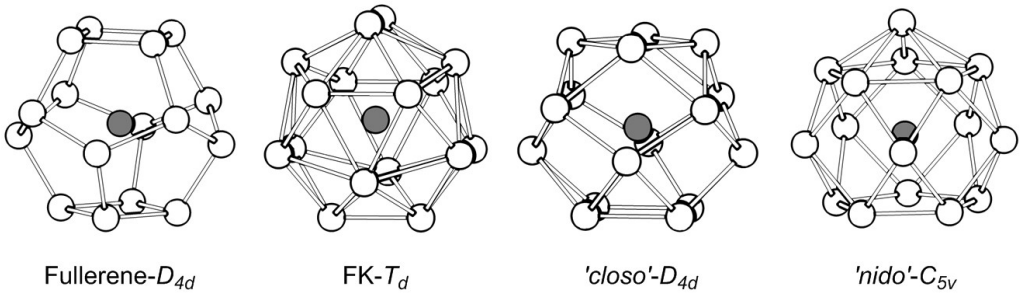


Figure 3.12: Structures of Ti@Si_{16} isomers considered in this study

Ti@Si_{16}	PBE	B3LYP	BLYP
Fullerene-D_{4d}	0.85	-0.59	-0.52
FK-T_d	0	0	0
'*closo*'-D_{4d}	0.66	0.64	
'*nido*'-C_{5v}	0.44	0.29	

Table 3.4: Relative energies in electron volt for four different Ti@Si_{16} isomers

M@Si_{16} stoichiometry, irrespective of its structure. The Frank-Kasper, '*closo*'-D_{4d} and '*nido*'-C_{5v} isomers all show the characteristic structural features of electron-deficient clusters in a Wade's rule sense – all three have highly-connected vertices and a number of triangular faces. It is striking, then, that the relative energies of these three isomers are not strongly dependent on functional: with both PBE and B3LYP, the FK isomer is the most stable among the three, followed by the '*nido*'-C_{5v} alternative. The fullerene-like isomer, in contrast, shows the characteristic 3-connected vertices and square/pentagonal faces, and its energy relative to the other three isomers is strongly dependent on functional: with PBE the FK isomer is the global minimum, 0.85 eV below the fullerene-like alternative while for B3LYP the order is reversed, with the fullerene-like isomer constituting the equilibrium structure. This replicates precisely the trends shown in Figure 3.2, where the B3LYP functional strongly stabilises the fullerene-like isomer in the M@Si_{14} series.

Chapter 4

Structures of endohedral clusters containing two transition metal atoms

4.1 Introduction

The aim of this chapter is to show how the bonding model developed for the $M@E_n$ clusters can be extended to their bi- and polymetallic analogues containing two or more endohedral transition metal atoms. Whilst the structures of monometallic endohedral tetrel clusters have been studied extensively, the larger $M_2@E_n$ analogues have attracted much less attention. Much of the work that has been reported is computational in nature, and several groups have used stable $M@E_n$ clusters as building blocks to construct dimers, trimers or nanotubes[46, 201–207]. The validity of this approach is not, however, obvious because the stability is generally associated with closed electron shells, which will tend to resist dimerisation and polymerisation. There are also a number of computational studies on M_2Si_n clusters that are not obviously related to smaller monometallic fragments[103, 208–211]. The most stable M_2Si_n clusters predicted in these papers often exhibit the typical 'fullerene-like' features of three connected vertices and pentagonal/ hexagonal

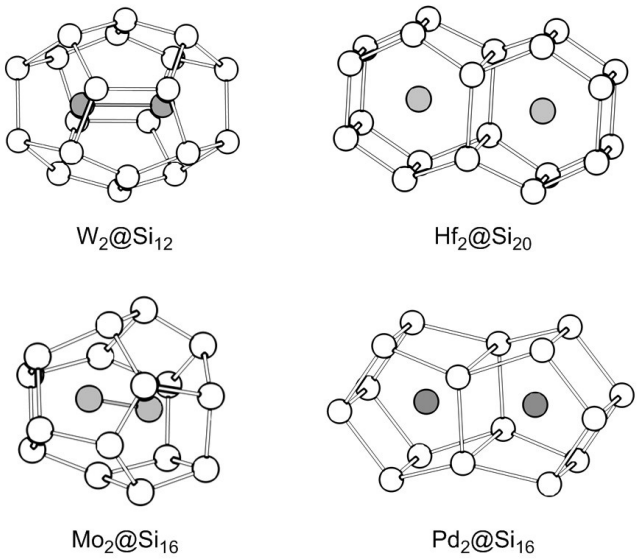


Figure 4.1: A selection of $M_2@Si_n$ structures reported in computational studies

faces. For example, Lu and co-workers have predicted the $W_2@Si_{20}$ cluster to be a dodecahedron elongated along C_2 axis[103] while Wang has suggested a structure based on stacked hexagonal silicon prisms for $M_2@Si_{20}$, M = V, Cr, Mo and Hf[208]. A closely related stacked pentagonal prismatic structure was proposed as the equilibrium structure for $Pd_2@Si_{16}$ and $Pt_2@Si_{16}$ by Han[210, 211], while the same group identified an isomer of $Mo_2@Si_{16}$ which resembles closely the elongated dodecahedron[209]. Unfortunately, there is very little experimental evidence that can be invoked to support these theoretical predictions. As was the case for the monometallic analogues, there are no crystallised examples of $M_2@Si_n$ clusters, but Katayama and co-workers[212] have prepared highly ordered honeycomb-like nanostructure arrays by depositing beryllium onto a Si(111) 7×7 reconstructed surface. The authors noted that the shape of the building blocks is similar to Be-encapsulated silicon nanotubes predicted by Singh *et al.*[213] although the height of these nanoscale features in the STM image is much smaller than one would expect for the nanotube based on the theoretical results. There are, however, a few structurally characterised $M_2@E_n$ clusters for the heavier tetrels, Ge or Sn, including

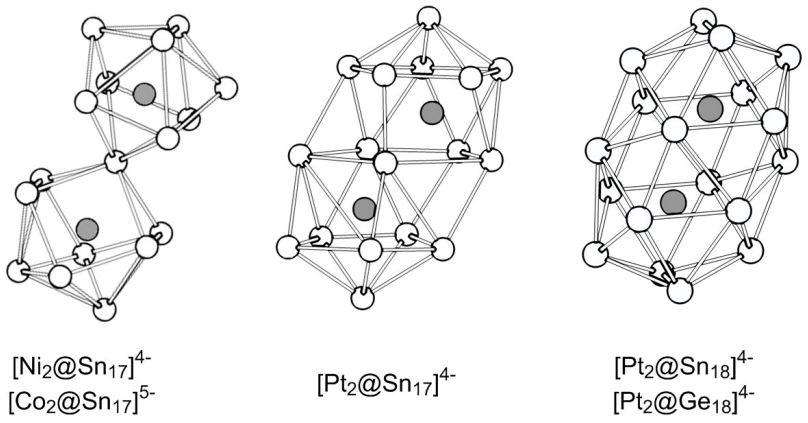


Figure 4.2: Schematic pictures of the experimentally characterised $M_2@E_n$ clusters

$[M_2@Sn_{17}]^{4-}$ (M=Pt, Ni)[31, 32], $[Co_2@Sn_{17}]^{5-}$[33] and $[Pd_2@E_{18}]^{4-}$ (E=Sn, Ge)[34, 35], all of which have approximately deltahedral structures (Figure 4.2). Amongst these, $[Ni_2@Sn_{17}]^{4-}$ and $[Co_2@Sn_{17}]^{5-}$ share the same D_{2d}-symmetric structure, consisting of two coupled distorted tricapped trigonal prisms sharing a common vertex. The $[Pd_2@E_{18}]^{4-}$ clusters are '*closo*' deltahedral clusters containing two identical $PdGe_9$ (or $PdSn_9$) units connected by an inversion centre. The $PdGe_9$ (or $PdSn_9$) unit can be viewed as a fragment of an I_h-symmetric $Pd@Ge_{12}$ ($Pd@Sn_{12}$) cluster, obtained by removing a Ge/Sn_3 triangle from the original icosahedron. The $[Pt_2@Sn_{17}]^{4-}$ cluster is somewhere in between $[Ni_2@Sn_{17}]^{4-}$ and $[Pd_2@Sn_{18}]^{4-}$: although one can divide this cluster into two distorted tricapped trigonal prisms, the orientation of the two units is different from that of $[Ni_2@Sn_{17}]^{4-}$, making the overall structure 'capsule-like'. None of these experimentally discovered isomers correspond to the computed ground state structures of the bimetallic silicon clusters which, as noted above, tend to show fullerene-like characteristics. As we have shown in previous chapters, the change to from "deltahedral" to 'fullerene-like' structures was not abrupt in the monometallic clusters, and in fact the relative stability of the two forms varies smoothly with changing factors such as the atomic number of the encapsulated transition metal atom, the type of tetrel and cluster

size. The 'fullerene-like' and 'deltahedral-type' isomers therefore inevitable come very close in energy for particular combinations of transition metal and tetrel, and there is no particular reasons to assume that the bimetallic clusters should behave differently despite the possible complicating factor of direct interactions between the transition metal ions. The remainder of this chapter focuses on an example of precisely this phenomenon, found in the $[Co_2@Ge_{16}]^{4-}$ anion synthesised by our collaborators in Oxford, under the direction of Professor José Goicoechea[37].

4.2 Experimental work on the $[Co_2@Ge_{16}]^z$ family

Goicoechea and co-workers[37] have prepared the $[K(2.2.2\text{-crypt})]_4[Co_2@Ge_{16}]\cdot 2en$ salt (2.2.2-crypt = 4,7,13,16,21,24-hexaoxa-1,10-diazabicyclo[8.8.8]hexacosane) by reacting an ethylenediamine solution of K_4Ge_9 and 2.2.2-crypt with a THF solution of $Co(PPhEt_2)_2(mes)_2$. Unfortunately, although crystalline samples of $[K(2.2.2\text{-crypt})]_4[Co_2@Ge_{16}]\cdot 2en$ could be isolated, they suffer from extensive disorder of the anionic moieties and a satisfactory single crystal X-ray structure could not be obtained. The presence of four charge-cancelling cations, however, suggests a 4- charge (we cannot eliminate the possibility that the cage is protonated although this has never been observed in monometallic germanium clusters). In ESI-MS experiments clusters with the same composition but much lower charge were observed (see Figure 4.3), immediately inviting the question of how the structure evolves with increasing charge. These questions encouraged us to use density functional theory to explore structure of the $[Co_2@Ge_{16}]^z$ clusters, the results of which are summarised below.

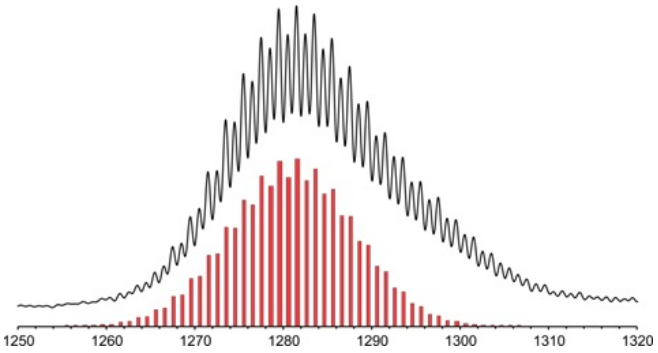


Figure 4.3: ESI-MS mass envelope corresponding to $[Co_2@Ge_{16}]^{1-}$ provided in Goicoechea's study[37]: experimental (black trace) and simulated (red)

4.3 Computational details

All calculations described in this chapter were performed with the Amsterdam Density Functional package[159–161] (ADF2013.02). A Slater-type basis set[162] of triple-ζ quality, extended with one polarisation function (TZP),was used to describe all transition metals and a DZP basis was used for tetrel elements. Electrons in orbitals up to and including $3d$ on Ge and $2p$ on cobalt were considered part of the core and treated in accordance with the frozen core approximation. All calculations employed the non-local exchange and correlation functional proposed by Becke and Perdew[146, 150]. Alternative choices of functional such as PBE[149] have been tested and shown not to materially affect the outcome. For the anionic species, a continuum dielectric solvation model[169–172] (COSMO) with ϵ=78.4 was imposed. All structures were optimised using the gradient algorithm of Versluis and Ziegler[163].

4.4 Result and discussions

4.4.1 Structural identification of the $[Co_2@Ge_{16}]^z$ cluster

In our computational survey, we have considered different isomers of $[Co_2@Ge_{16}]^z$ where z ranges from 0 to 4, including the Frank-Kasper symmetric isomer reported for monometallic $M@E_{16}$ cluster studies (see Chapter 1 and 3). We have used a number of high-symmetry structures as initial starting points, but the calculations always converge on one of three stable minima shown in Figure 4.4. At each of the five oxidation level of $[Co_2@Ge_{16}]^z$ studied, the most stable isomer has D_{2h} symmetry, and is isostructural to the predicted equilibrium structures of $Pd_2@Si_{16}$ and $Pt_2@Si_{16}$. The cluster unit can be described as a fusion of two identical pentagonal prismatic $Co@Ge_{10}$ units (the structure of which is shown in Chapter 1 Figure 1.1 as '10B') through a rectangular face, with the four germanium atoms on the shared face expanding outwards in a direction perpendicular to the Co-Co axis. For both the neutral and the tetra-anionic clusters, an alternative C_{2h}-symmetric isomer lies only about 0.3 eV higher than the D_{2h}-symmetric alternative. The C_{2h}-symmetric structure was reported to be the global minimum of Si_{16} in the theoretical study of Shvartsburg[214] and is clearly deltahedral in nature, with characteristic high-connectivity vertices and triangular faces. The third isomer, with D_{4d} symmetry , can be constructed at least notionally from 'fullerene-like' $M@Si_{16}$ clusters by replacing the central metal atom by metal atom dimer. It therefore allows close approach of the metal atoms and the formation of M-M bonds. While the D_{4d}-symmetric isomer found in our calculation bears a strong resemblance to the reported structure of Mo_2Si_{16} where strong Mo-Mo multiple bonding prevails[209], in all calculations on $[Co_2@Ge_{16}]^z$, this isomer was found to be much higher in energy than the D_{2h}- and C_{2h}-symmetric alternatives, and thus

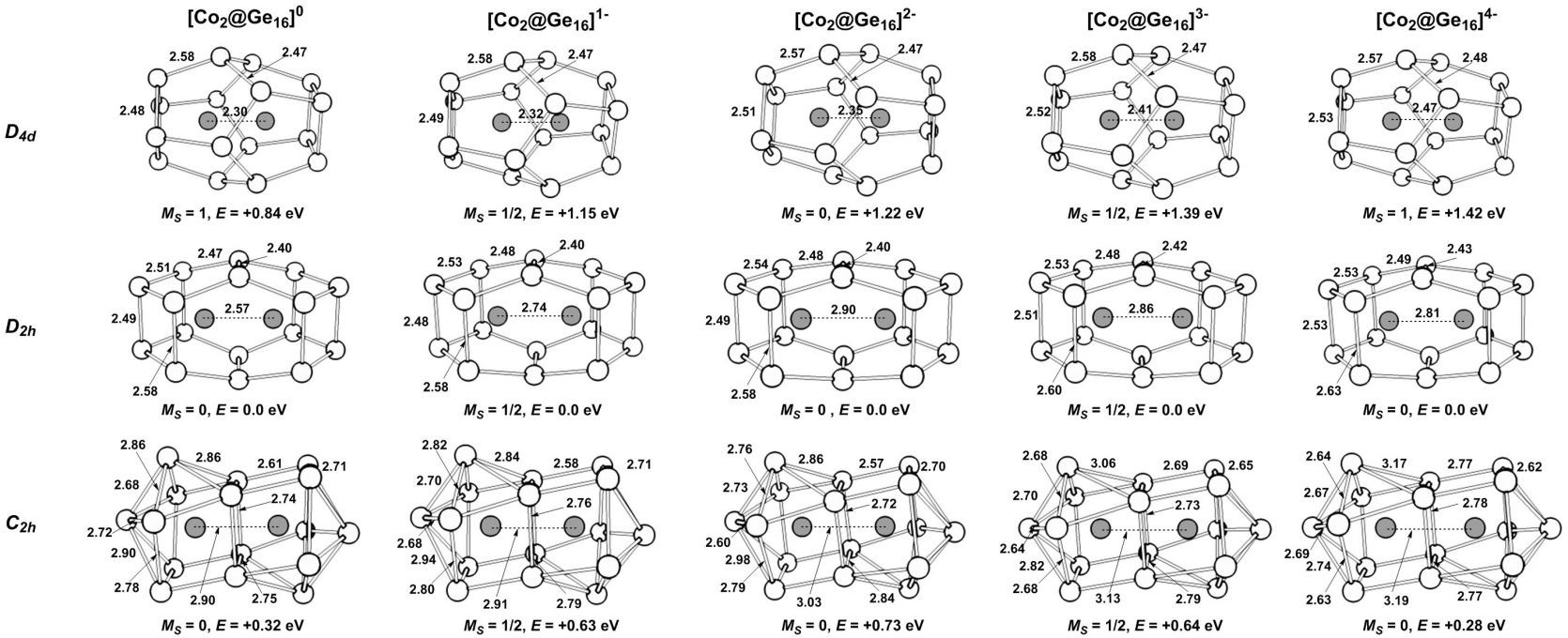


Figure 4.4: The lowest lying optimised structures of $[Co_2@Ge_{16}]^z$, z = 0-4

can be confidently ruled out as a candidate for the experimental structure. The 0.3 eV separation between the D_{2h}- and C_{2h}-symmetric isomers is, however, too close to offer a confident statement on the structure of [K(2.2.2-crypt)]$_4$[Co_2@Ge_{16}]·2en in the solid state. In a subsequent study reported in *Chem. Eur. J.* in 2017, Sun and co-workers[38] synthesised the same $[Co_2@Ge_{16}]^{4-}$ anion via the reaction of [(ArN)$_2$CtBuCo(η^6-toluene)] (Ar=2,6-diisopropylphenyl) and K_4Ge_9 in ethylenediamine solution in the presence of 2.2.2-crypt. They were able obtain diffraction-quality crystals, in this case with only a single molecule of en solvent in the unit cell, [K(2.2.2-crypt)]$_4$[Co_2@Ge_{16}]·en. Remarkably, the $[Co_2@Ge_{16}]^{4-}$ anion occupies two sites in the the crystalline lattice of [K(2.2.2-crypt)]$_4$[Co_2@Ge_{16}]·en. The first site contains only the D_{2h} isomer reported in our DFT study[37] while the second site, in contrast, contains a mixture of the D_{2h} and C_{2h} isomers, with the latter dominating (90%). The bond lengths and angles of the D_{2h} isomer are in remarkable agreement with our computed values (Figure 4.3), with Ge-Ge distances ranging from 2.44 to 2.59 Å, and a Co-Co distance of 2.75 Å. The Ge-Ge distances in the quasi-C_{2h} isomer lie between 2.56 and 3.21 Å, again matching well with the theoretical prediction. The fact that the two isomers co-exist in the solid state is a very clear indication that they have similar energies, precisely as predicted in our earlier computational study. It seems, therefore, that $[Co_2@Ge_{16}]^{4-}$ anion represents another case where the fullerene-like and deltahedral motifs are very close in energy, precisely as we saw in the Cr@Si_{14} case with the competing fullerene-like and *arachno* isomers. Nevertheless, before we draw an conclusion to this matter, we need to look into the electronic structure of these two isomers.

4.4.2 Electronic structure of the $[Co_2@Ge_{16}]^z$ clusters

One key question here is whether there is direct bonding interaction between the two metal atoms, either in the tetra-anion present in the crystal or in one of the

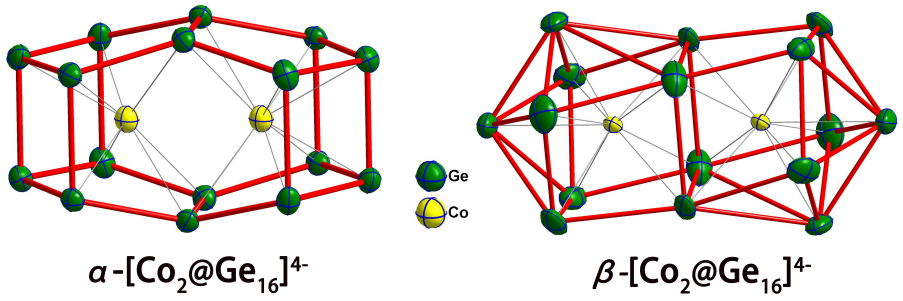


Figure 4.5: Thermal ellipsoid plot of $[Co_2@Ge_{16}]^{4-}$ at two different sites (drawn at 50% probability level) provided in the study of Sun Zhongming *et al.*

more oxidised states observed in the mass spectrum. As shown in Figure 4.4, the distance between the two Co atoms in our calculation is 2.81 Å in the D_{2h}-symmetric global minimum of $[Co_2@Ge_{16}]^{4-}$, similar to the Pd-Pd separation of 2.83 Å in the $[Pd_2@Ge_{18}]^{4-}$ compound, where no bond was proposed[35]. One- and two-electron oxidation drives a further elongation of the Co-Co separation to 2.90 Å but further oxidation to the mono-anion and neutral species reverses this trend, leading to a short distance of 2.57 Å in the latter. The contraction of the metal-metal distance is accompanied by an outward displacement of the four Ge atoms that lie in the plane bisecting the two Co centres: as the metal-metal bonding interaction becomes more significant, the Ge_{16} cage becomes more spherical. The Kohn-Sham orbital diagrams shown in Figure 4.6 (right) indicate the origin of these bond length changes. The HOMO of $[Co_2@Ge_{16}]^{4-}$ is the $4b_{3g}$ orbital which is localised primarily on the germanium cage. The out-of-phase character of the $4b_{3g}$ orbital between the top and the bottom layer suggests an antibonding interaction in the z direction on the cage. The HOMO also has a small amount of Co d_{yz} character in an in-phase arrangement. Gradually depopulating this $4b_{3g}$ orbital should therefore result in a contraction of the Ge-Ge bond lengths in the z direction and a slight elongation of the Co-Co distance, precisely as observed in Figure 4.4. The HOMO-1 of $[Co_2@Ge_{16}]^{4-}$, the $5b_{1g}$ orbital, is in contrast localised mainly on the metal and the Co d_{xy} orbitals are combined in an out-of-phase pattern to give

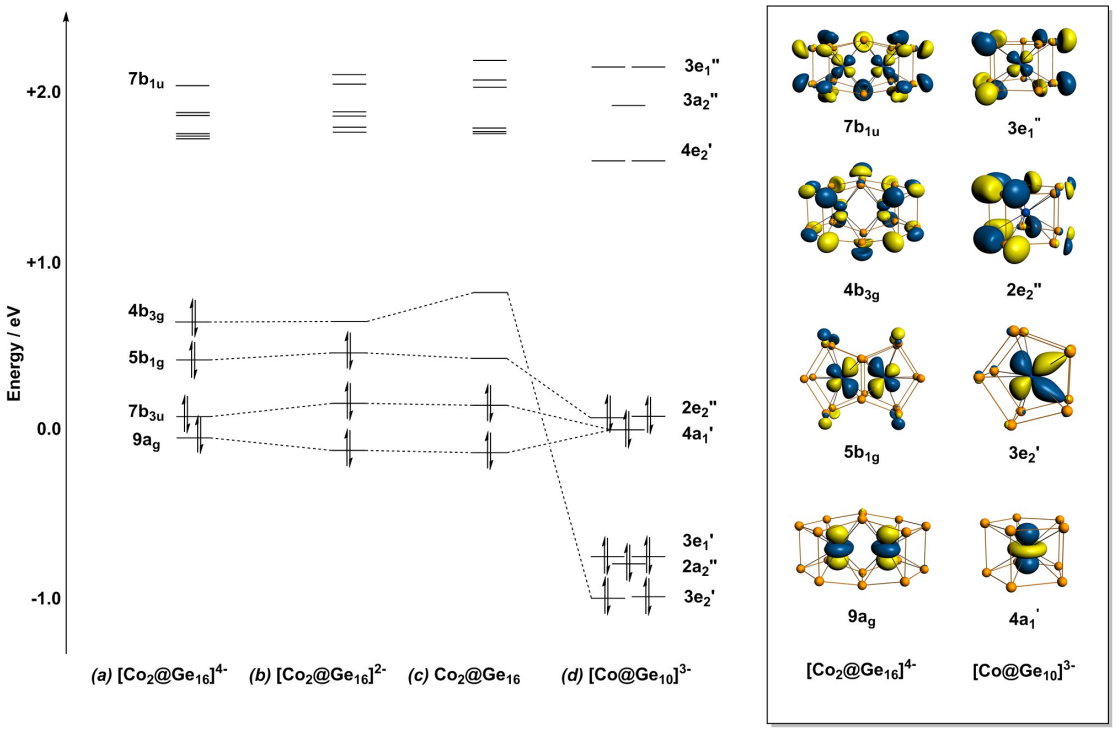


Figure 4.6: Kohn-Sham diagrams for D_{2h}-symmetric $[Co_2@Ge_{16}]^z$, z = 4, 2, 0 and D_{5h}-symmetric $[Co@Ge_{10}]^{3-}$. The contour plots emphasise the close relation between the mono- and bimetallic structures

significant Co-Co π* character. Oxidation to $[Co_2@Ge_{16}]^-$ and then to the neutral cluster depopulates the $5b_{1g}$ orbital (as well as the $4b_{3g}$ orbital) and so causes the emergence of a significant Co-Co π bonding interaction and a contraction in the Co-Co distance. The computed Mayer bond orders mirror the structural trends, with the Co-Co bond order dropping marginally from 0.26 to 0.20 upon oxidation from $[Co_2@Ge_{16}]^{4-}$ to $[Co_2@Ge_{16}]^{2-}$, then rising to 0.49 at $Co_2@Ge_{16}$. Thus although the Co-Co bonding is relatively weak in the tetra-anion found in the X-ray structure, it seems likely that the transition metal ions interact more strongly in the more highly oxidised species observed in the mass spectrum. It is clear that the D_{2h}-symmetric isomer of $[Co_2@Ge_{16}]^{4-}$ can be thought of as a 'dimer' of the pentagonal prismatic $[Co@Ge_{10}]^{3-}$ cluster reported by Fässler and co-workers[39], and more generally as being typical of a fullerene-type structure. This in turn suggests that some or all of the metal *d* electrons play a 'dual role', contributing both to the

electron count at the cage and at the metal. The 52-electron $[Co@Ge_{10}]^{3-}$ can be regarded as an 'electron-precise' cluster, which is on the electron-rich limit of the fullerene route. For a hypothetical electron-precise $[Ge_{10}]^{10-}$ cluster, one needs 5n = 50 valence electrons, 3n of which are used to construct the 2c-2e cage σ bonds and 2n form the lone pairs. A symmetry analysis using the edges of the pentagonal prism (D_{5h}) as a basis suggests that the cage σ bonding orbitals span the set $2a_1'+1a_2''+2e_1'+2e_2'+1e_1''+1e_2''$ while using the n vertices as a basis (synonymous with the radial lone pairs) gives $1a_1'+1a_2''+1e_1'+1e_2'+1e_1''+1e_2''$. These 25 orbitals correspond precisely to the symmetries of the occupied manifold in $[Co@Ge_{10}]^{3-}$ shown in Figure 4.6, with the two surplus electrons occupying a localised metal d_{z^2} orbital, which is non-bonding with respect to the cage ($4a_1'$). From the perspective of the metal, an 18-electron count implies the participation of 4*s*, 4*p* and 3*d* orbitals, either in bonding or to accommodate metal-based lone pairs. These transform as a_1', $a_2''+e_1'$ and $a_1'+e_2'+e_1''$, respectively and so a subset of 8 of the 25 orbitals noted above (with $a_1'+a_2''+e_1'+e_2'+e_1''$ symmetry) play a dual row, contributing both to the 18 electron count at the metal and the 5n electron count at the cage. The arguments can be extended to $[Co_2@Ge_{16}]^{4-}$ which can be regarded as a fusions of two $[Co@Ge_{10}]^{3-}$ clusters. The relationship between selected frontier orbitals of $[Co_2@Ge_{16}]^{4-}$ and $[Co@Ge_{10}]^{3-}$ is shown in Figure 4.6. If we consider a hypothetical electron-precise $[Ge_{16}]^{16-}$ cluster with D_{2h} symmetry, the cage bonding orbitals (along the edges) and the lone pairs (at the vertices) would span a set of orbitals with $8a_g+4b_{1g}+4b_{2g}+4b_{3g}+3a_u+6b_{1u}+5b_{2u}+6b_{3u}$ symmetry. These are precisely the symmetries of the occupied set of orbitals in $[Co_2@Ge_{16}]^{4-}$, supplemented now by three mainly metal-based orbitals: $9a_g$, $7b_{3u}$ and $5b_{1g}$. The first two are the in-phase and out-of-phase combinations of the metal d_{z^2} orbitals which are the analogues of the $4a_1'$ orbital of the 10-vertex cluster and the last one is the out-of-phase combination of metal d_{xy} orbitals. An 18-electron count at each metal therefore demands

that a further 15 of the Ge-Ge bonding orbitals play a dual role by overlapping with the $4s$, $4p$, $3d$ orbitals of the metal core.

The electronic structure of the less stable C_{2h}-symmetric isomer of $[Co_2@Ge_{16}]^{4-}$ is rather more difficult to analyse, because the deltahedral structure precludes a simple symmetry analysis based on lone pairs and 2-centre-2-electron bonds. In their study, Sun and co-workers[38] applied the adaptive natural density partitioning (AdNDP) method to both crystallised isomers. In the case of the D_{2h} isomer, the AdNDP analysis confirms the presence of localised 2c-2e σ bonds between the germanium atoms but in the case of the C_{2h} isomer delocalised multicentre σ bonds prevail. According to Sun's calculations, the capped pentagons and the bisecting germanium square should be able to rotate with respect to each other with a negligible barrier, leading to fluxional behaviour in solution.

The co-crystallisation and the AdNDP analysis together support the idea that here in $[Co_2@Ge_{16}]^{4-}$ we are faced with a scenario where the fullerene-route and the Wade's rule route are almost equally stable, such that the structure of the cluster could adopt either of them given the right conditions. However, unlike the D_{2h}-symmetric isomer, the electronic structure of which clearly suggests an 'electron-precise' configuration, though we are certain that the C_{2h}-symmetric isomer can be regarded as an electron-deficient deltahedral type of cluster, whether it can be treated as a *closo*, *nido*, or *arachno* is still debatable at this stage. For a further discussion of this isomer, we need to first look for an electron counting framework suitable for condensed polyhedral electron-deficient clusters, as Wade's rule were formulated for mono-polyhedral clusters only. Therefore, the discussion will continue on in the next section, where the focus will be the exploration of relationship between mono- and condensed polyhedral electron-deficient clusters.

4.4.3 Extensions to other polymetallic clusters and some thoughts on cluster growth mechanisms

The discussion in this chapter, based on both theory and X-ray crystallography, has shown that the $[Co_2@Ge_{16}]^{4-}$ cluster is almost equally stable in fullerene-like and deltahedral isomers. This leads to an important question: to what extent can we treat the bimetallic clusters as simple extensions to their monometallic analogues. To make sense of the stability of these clusters, we can apply the 'mno rule' developed by Jemmis[215], which is an extension of Wade's rules to fused clusters. Wade's rules were formulated for mono-polyhedral clusters, where occupation of a single core bonding molecular orbital and n tangential surface bonding molecular orbitals leads to a stable closed-shell configuration[60, 61]. In the case of condensed polyhedral clusters, such as the bimetallic tetrel clusters of interest here, there is obviously more than one core and thus a generalisation of the rules is needed. According to Jemmis' mno rule, the number of skeletal electron pairs (SEP) required by a condensed polyhedral cluster is m+n+o+p-q, where m is the number of sub-clusters, which equals the number of core bonding MOs, n is the number of vertices (equal to the number of tangential surface bonding MOs), o this the number of single-vertex shared condensations, p is the number of missing vertices and q is the number of caps. The 'missing vertices' capture the *closo-nido-arachno-hypho* relationship in Wade's rules, wherein structures with progressively lower numbers of vertices share the same electron count. Thus the *nido*, *arachno* and *hypho* clusters can be considered to be derived from their *closo* parent through the loss of one, two and three vertices, respectively. 'o' is added into the count because single-vertex sharing is a special case where each individual sub-clusters has to satisfy Wade's rule so that the number of tangential surface bonding MOs no longer equals 'n' but 'n+o' (since the shared vertex needs to be counted repeatedly).

In summary, a '*closo*' condensed polyhedral cluster should have 'm+n+o' skeletal electron pairs. More electrons would open up the cluster just like in monopolyhedral cluster cases.

The $[Pd_2@E_{18}]^{4-}$ (E=Sn, Ge) clusters shown in Figure 4.2 fit the Jemmis mno rule as *closo* clusters: each Sn or Ge atom provides one skeletal electron pair, the Pd atoms provide none, and the four negative charges provide two pairs, adding up to a total of 20 = 2+18+0 SEPs, exactly as the configuration required. The structure of the $[Ni_2@Sn_{17}]^{4-}$ cluster can be understood in the same way: $[Ni_2@Sn_{17}]^{4-}$ has one shared vertex and requires 2+17+1= 20 SEPs, the shared Sn atom can provide 2 electron pairs instead of one, because there is no lone pair on this highly connected atom. The isoelectronic $[Pt_2@Sn_{17}]^{4-}$ cluster apparently adopts a rather different structure based on a single ellipsoidal Sn_{17} cage, which would demand only 19 SEPs since there is no single vertex shared between two polyhedral. The reasons why $[Ni_2@Sn_{17}]^{4-}$ and $[Pt_2@Sn_{17}]^{4-}$ adopt different structure is unclear from this perspective since both fit Jemmis rule, although one possibility is that this is simply due to the greater size of Pt which destabilises the small Sn_9 polyhedra.

All of the electron count assessments given above are based on the assumption that the central metals are in closed-shell d^{10} configuration and do not contribute to the cage skeletal electron count. Our analysis above suggests that this is clearly not the case for the D_{2h}-symmetric isomer, where the 3-connected vertices are a clear indication of hybridisation of the orbitals on the metal and the cage. The role of these *d* orbitals in the deltahedral C_{2h}-symmetric isomer of $[Co_2@Ge_{16}]^{4-}$ is, however, less clear. If we assume that the cobalt atoms have a d^{10} configuration ($[Co^-]_2$) and contribute no electrons to the cage, we have a total of 16 x 4 +2 = 66 valence electrons available. The number that contributes to the skeletal electron count then depends critically on the number of electrons assigned to lone pairs on the Ge vertices. Recall that in $[Ni_2@Sn_{17}]^{4-}$, it was assumed that the shared (8-

coordinate) Sn atom did not carry a lone pair, but rather contributed all 4 valence electrons to the cluster count. If we make the same assumption for the four Ge atoms in the bisecting plane of the C_{2h}-symmetric isomer, we have 12×2 + 4×4 +2 = 42 skeletal electrons (or 21 SEPs). However, these 4 germanium atoms are only five coordinated and are not approximately spherically coordinated, so if we make the alternative assumption that they do each carry a lone pair then the cage electron count is reduced to 16×2 +2 = 34, or 17 SEPs. A *closo* configuration requires 16+2=18 SEPs according to Jemmis' rules, which means in the latter situation, there would be two electrons short for a perfect *closo* cluster. Alternatively, a count of 21 SEPs would demand three missing vertices – i.e. a condensed polyhedral analogue of a 'hypho' cluster in the Wade's rules ansatz.

At first sight, the quasi-C_{2h} isomer has six square faces, which seems to suggest that this structure is 'more open' than a *closo* structure and therefore the number of skeletal electrons on the cage clearly exceeds 36 (18×2). However, if there are four lone pair orbitals in the bisecting plane, they would span the set (a_g+b_g+a_u+b_u), and looking through the KS orbitals of $[Co_2@Ge_{16}]^{4-}$ we can actually spot three of them among the occupied orbitals (see Figure 4.7). Judging from the shape of their isosurface contours, although the electrons in the a_g orbital are debatable, it should be a reasonable argument to say that the electrons in the b_u and a_u orbitals are lone pair electrons. This means the germanium atoms are providing fewer than 21 SEPs if we consider the $[Co_2@Ge_{16}]^{4-}$ a typical Jemmis rule cluster. There are three possible ways to interpret this result: 1. The cluster is in fact closer to a '*closo*' cluster rather than '*nido*' or '*arachno*' clusters regarding the number of SEPs, but the square faces are not able to 'close up' due to the small size of the cluster. 2. The electron count on the cage does exceed 36, because the cobalt *d* electrons, or at least a subset of them, contribute to the cage electron count. 3. The cage itself is not a typical Wade's rule (or Jemmis rule) cage. Although there are delocalised multi-

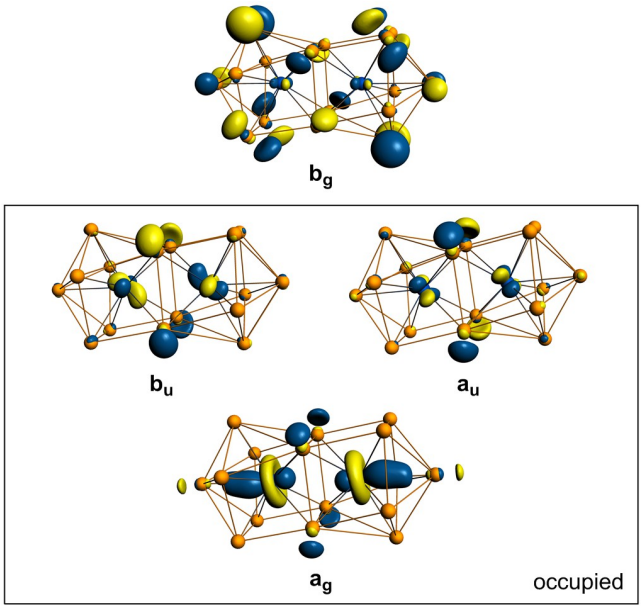


Figure 4.7: Orbitals corresponding to 'lone-pairs' on the bisecting germanium atoms in $[Co_2@Ge_{16}]^{4-}$

centre σ bonds that construct the framework, it is not true that there are precisely two lone-pair-electrons on each vertex. Evidence supporting the first possibility includes the structures of $FeSn_8$[216] and $ZnSn_8$[57] predicted theoretically. Since neither of these tin clusters are endohedral, it should be reasonable to infer that $[CoGe_8]^{2-}$ is not endohedral and therefore it is difficult for a 16-vertex germanium cage to fully enclose two non-interacting cobalt atoms. If the second interpretation is true, the first problem we face is the fact that $[Co_2@Sn_{17}]^{5-}$ is a *closo* cluster. However, it is well known that the geometries of 9-vertex tetrel clusters are flexible and the tricapped trigonal prism (or distorted tricapped trigonal prism) is capable of accommodating more than two electrons[19, 29, 30, 217] so it is perhaps too crude an approximation to say the $Co@Sn_9$ unit or even the $[Co_2@Sn_{17}]^{5-}$ cluster itself is really '*closo*'. The third proposal comes from the fact that this C_{2h} isomer is the predicted ground-state isomer for Si_{16}[214]. In the Si_{16} cluster, there is no external electron source, and its geometry deviates from what one would expect from a '*closo*' because forming lone pairs and delocalised σ bonds is no longer preferable

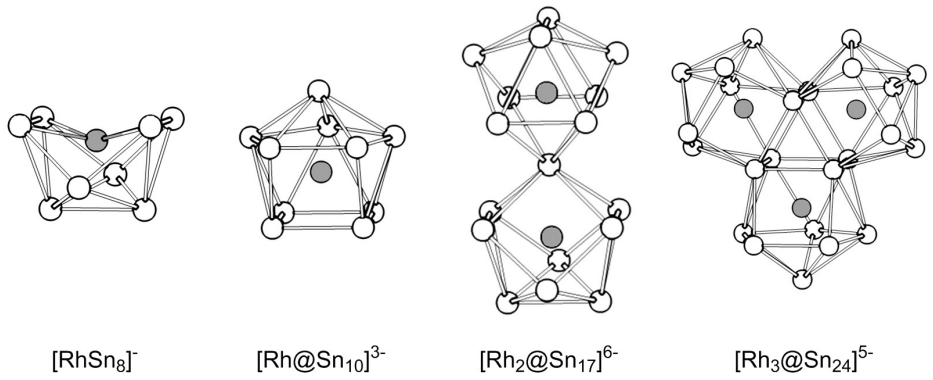


Figure 4.8: The structures of four rhodium stannides in different sizes and charges

to forming π bonds and and localised σ bonds as in the fullerene-like model. It is possible that one or more of the bonding situations we proposed here is valid and that the Jemmis' rules are an over-simplification of the reality. In fact, we do not even know what the '*closo*' structure should be like for a condensed polyhedron and thus it is difficult to extrapolate to the corresponding '*nido*' or '*arachno*' concepts. Nevertheless, we can be certain that the highly connected vertices and deltahedral structures are the signatures of delocalised multicentre σ bonding framework, which is preferred by heavier tetrels and gradually becomes less favourable as we go to lighter elements of the same group. In a very recent collaborative project with Sun and coworkers, we have explored the electronic structure of a tri-fused stannide anion $[Rh_3@Sn_{24}]^{5-}$, along with smaller rhodium encapsulating stannides $[Rh_2@Sn_{17}]^{6-}$ and $[Rh@Sn_{10}]^{3-}$ that were also characterised crystallographically. In the context of the discussion of $[Co_2@Ge_{16}]^{4-}$, the most significant observation is that the structure of $[Rh@Sn_{10}]^{3-}$ resembles closely one half of the C_{2h}- isomer of $[Co_2@Ge_{16}]^{4-}$, while the structure of $[Rh_3@Sn_{24}]^{5-}$ can be regarded as a fusion of three such units. Thus the $[Rh@Sn_{10}]^{3-} \rightarrow [Co_2@Ge_{16}]^{4-} \rightarrow [Rh_3@Sn_{24}]^{5-}$ series represents a snapshot of the fusion of two and three 10-vertex units *via* square faces. Whether this structural observation reflects the actual process of cluster growth is not, however, clear. The electrospray ionisa-

tion mass spectrometry (ESI-MS) spectrum of the DMF solution of dissolved crystalline $[K([2.2.2]crypt)]_3[Rh@Sn_{10}]\cdot en$ reveals a complex reaction mixture containing $K[Rh@Sn_8]^-$ and $[Rh@Sn_8]^-$ in addition to $[Rh@Sn_{10}]^-$, $K[Rh@Sn_{10}]^-$ and (K[2.2.2]-crypt) $[Rh@Sn_{10}]^-$. A survey of the potential energy surface identified a C_{2v}-symmetric singlet as the ground state of $[RhSn_8]^-$ where the Rh atom sits on the Sn_8 cluster in approximately square-planar coordination. A closer examination of this $[RhSn_8]^-$ isomer reveals that structurally, it can be regarded as a fragment of the C_{2v} isomer of $[Rh@Sn_{10}]^{3-}$, obtained by directly removing two Sn atoms on the edge of a square face. It has been shown by Eichhorn and co-workers in an ESI-MS study [31] that the loss of Sn atoms from polystannide clusters is a general phenomenon, and so it could be that the combination of coalescence of monometallic fragments and loss of tetral elements is responsible for the formation of larger clusters in solution. We do not yet have sufficient experimental information to justify a full exploration of the potential energy surface using DFT, but the crystallographic evidence highlights the fact that multi-metallic species are not fundamentally different from the monometallic ones, and that their stability can be considered within the same framework as smaller monometallic clusters.

Chapter 5

Electronic structure and electron transport properties of adsorbed WSi_{12} clusters on a Si(111) surface

5.1 Introduction

This final results chapter will be dedicated to the exploration of surface-supported metal clusters and will focus particularly on the link between the intrinsic electronic properties of an isolated cluster and its ability to conduct current when attached to a silicon surface. As noted in the introductory chapter, the inspiration and motivation for this work comes from Kanayama's study[51] of the deposition of $[TaSi_{10-13}H_x]^+$ clusters onto 7×7 reconstructed Si(111) surfaces and their subsequent characterised using scanning tunnelling microscopy (STM). The images of the $[TaSi_{10-13}H_x]^+$ clusters reported by Kanayama *et al.* show features with similar dimension to the isolated clusters, from which the authors concluded that the clusters remain intact after deposition (*i.e.* they undergo a 'soft landing'). Moreover, in a small number of cases 'double stripes' ~2.5 Å apart were observed on the sur-

face, close to the DFT-computed distances between hexagonal faces in an isolated $[Ta@Si_{12}]^+$ cluster. This feature was proposed to arise from $Ta@Si_{12}$ clusters that had landed on their rectangular faces. These STM images are important in so much as they provide the only direct structural information for the family of silicon clusters that has been the focus of much of this thesis. More importantly, the potential for grafting clusters with well-defined architectures onto a silicon surface may offer a mechanism for modifying the intrinsic transport electron-transport properties of silicon. There may therefore be potential applications in the field of molecular electronics but these can only be realised if we understand fully the relationship between the transport properties and the intrinsic electronic structure of adsorbed molecule. The formation of metal silicides through the adsorption of free metal atoms on a silicon surface has been established in the literature for many years. In a recent study by Lilley and co-workers[218], nickel was deposited onto a 7×7 reconstructed Si(111) surface, leading to the formation of the so-called $\sqrt{7}$ and $\sqrt{19}$ ring clusters[219–221], first identified in the 1990's and 1980's, respectively. In the proposed structure of the $\sqrt{7}$ cluster, shown in Figure 5.1a, the metal atom sits in a surface substitutional site, with a ring of six silicon adatoms above it, three of which are 'bridging adatoms' bonded to a single silicon substrate atom while the other three are connected to two 'bridging adatoms'. In the $\sqrt{19}$ ring cluster (Figure 5.1b), in contrast, three metal atoms occupy positions in the surface layer, with six adatoms above the surface . Reproducible resonant tunnelling through quantised levels was reported for clusters of both sizes and the band gap, measured by resonant peaks above and below the Fermi level in the dI/dV trace, is larger in the smaller $\sqrt{7}$ cluster, as would be expected for quantum dots. The study therefore suggests that these clusters can be viewed as discrete surface entities with the potential for qubit design. Whilst Kanayama and co-workers have attempted to interpret their images in terms of the bond metrics of the isolated clusters, the pre-

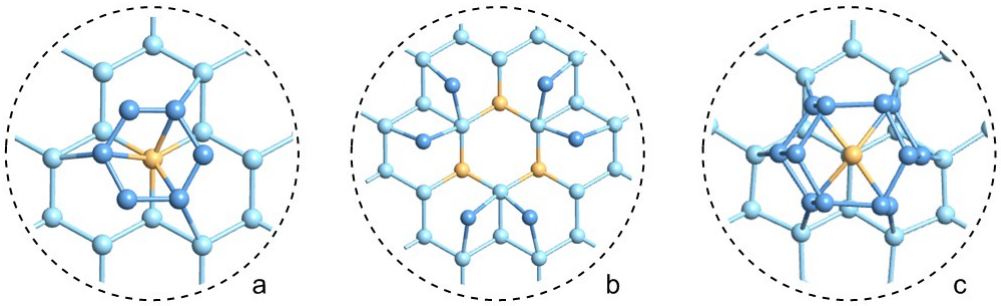


Figure 5.1: Schematic picture of proposed structures of (a) a $\sqrt{7}$ ring cluster (b) a $\sqrt{19}$ ring cluster and (c) absorbed $CrSi_{12}$. Metal atoms, surface silicon atoms and additional silicon atoms are shown as yellow, light blue and blue balls, respectively

cise structure of the $Ta@Si_{12}$ cluster deposited on 7×7 reconstructed surface Si(111) remains uncertain. Some possible arrangements were revealed by Khanna and co-workers who modelled the structures of adsorbed $Cr@Si_{12}$ clusters on a simple unreconstructed Si(111) surface[204]. Their calculations showed that in the most stable structures, the Si_{12} cage remains intact but the Cr atom forms an additional bond to the closest surface silicon atom , becoming 13-coordinate (Figure 5.1c). In all cases, the unsaturated Si atoms of the cluster form strong covalent bonds to the surface and, as a result, the border between the cluster and the surface becomes hard to define. There is a striking resemblance between Khanna's proposed structure of the surface-attached $M@Si_{12}$ cluster and the local structure of the $\sqrt{7}$ cluster: in both cases, a single metal atom sits on the substrate surface and is capped by extra silicon atoms. In this chapter, we extend Khanna's study in two distinct ways. First, we consider more elaborate and accurate models for the silicon surface including the 7×7 reconstruction used in the experimental work itself and also the two distinct reconstructed cleaved Si(111) surface models with smaller unit cells proposed by Haneman[222] and by Pandey[223]. Second, we explicitly compute the transmission properties of the surface-bound clusters, thereby establishing a direct link from the electronic structure of the cluster to the features observed in the experiment. Computing electron transport properties of molecules is a challenging

task even when the molecules are absorbed on metallic surfaces where the density of states around the Fermi level is large and (relatively) constant. For a silicon surface, the Fermi level sits in the band gap and as a result the effects of charge depletion can extend several layers into the surface. As a result, a deep unit cell is typically needed to model such systems, making the calculations computationally more demanding. Moreover, the surface dynamics controlling electron transport are strongly dependent on the subtleties of the surface reconstructions[224]. Kanayama has argued that the surface absorption will be accompanied by electron transfer from the bulk silicon, such that the $Ta@Si_{12}$ unit becomes negatively charged to attain a closed-shell configuration (isoelectronic with $Cr@Si_{12}$). Our surface models contain only a limited number of layers and so do not afford the possibility of electron transfer from deep within the bulk. To avoid the possibility of spurious charge transfer effects within our finite unit cells, we have therefore chosen to use neutral $W@Si_{12}$, isoelectronic to $[Ta@Si_{12}]^{-}$. The chapter is arranged in the following way. First the computational methodology is set out, followed by a brief recap of the electronic structure of $W@Si_{12}$ (this is almost identical to $Cr@Si_{12}$, which has been discussed in detail by Khanna, McGrady and Goicoechea and others[77, 104, 110]). The geometry of the cluster-surface system is then explored using periodic DFT calculations with a plane-wave basis set. Once the stable configurations of the cluster-surface systems have been identified, I will then move on to our electron transport study, where the optimised surface geometries are taken to set up the silicon-molecule-vacuum-gold tip device. Non-equilibrium Green's functions (NEGF) are then used to calculate the transmission properties of the cluster/surface interface.

5.2 Computational methods

5.2.1 Gas-phase studies

The properties of the isolated molecule W@Si_{12} were calculated using the PBE functional as implemented in the ADF software package[159–161] (ADF2013.01). All-electron Slater-type basis sets of triple-ζ plus polarisation function (TZP) and all-electron Slater-type basis sets of double-ζ plus polarisation (DZP) quality were used for W and Si, respectively[162]. The scalar relativistic zeroth-order regular approximation[164–168] (ZORA) to the Dirac equation is used in all calculations. The Conductor-like Screening Model[169–172] (COSMO) of solvation was applied in all cases (ϵ=78.4).

5.2.2 Surface studies

Geometry optimisations on cluster-surface systems were done with the Vienna *ab initio* Simulation Package 5.3.2[225, 226] (VASP.5.3.2) with the PW91 functional[151, 227] and a plane-wave basis set. An energy cutoff of 280 eV was used for all geometry optimisations. The Brillouin zone was sampled on a 4×4×1 Monkhorst Pack grid and a 2×2×1 Monkhorst Pack grid for the clean cleaved Si(111) surface systems and 7×7 reconstructed Si(111) surface systems, respectively. The Lattice parameters are listed in Table 5.1: the value of c is chosen to give a vacuum layer greater than 10 Å between periodic repetitions in this direction (see Figure 5.2).

5.2.3 Electron transport properties

Electron transport properties were calculated with the Atomistix ToolKit 2016.4 software package[228–230] (ATK 2016.4) using the PBE functional[149] and numerical LCAO basis sets[231] with double-ζ plus polarisation quality for all atoms (W, Si

	a(Å)	b(Å)	c(Å)
Clean cleaved Si(111)	15.36	15.36	22.54
Clean cleaved Si(111) + WSi_{12}	15.36	15.36	25.00
7×7 reconstructed Si(111)	26.88	26.88	20.40
7×7 reconstructed Si(111) + WSi_{12}	26.88	26.88	28.00

Table 5.1: Lattice parameters for the computed surface systems

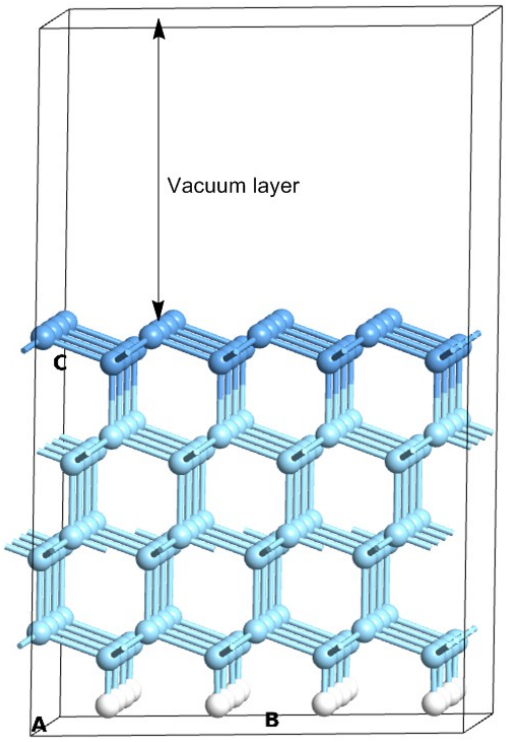


Figure 5.2: Unit cell settings

and Au). The Brillouin zone was sampled on a 5×5 grid in the plane perpendicular to the transport direction with 100 points along the transport direction. The process of the model construction will be discussed in detail later in the Results and discussion section. The configuration of the device model will be shown in Figure 5.11.

5.3 Results and discussion

5.3.1 Electronic structure of W@Si_{12}

W@Si_{12} and the isoelectronic species Cr@Si_{12} and Mo@Si_{12} have been studied extensively by several groups, and it is now a consensus that they adopt a D_{6h}-symmetric hexagonal prismatic structure where each Si vertex is connected to 3 others. In Chapter 1, we have summarised the structural studies and reviewed the electronic structure of these clusters, and in Chapter 3, we have rationalised the stability of the fullerene-like isomer of Cr@Si_{14}, to which the hexagonal prismatic W@Si_{12} cluster is closely related. Here I will only give a brief recap of the relevant features of the cluster electronic structure, which is summarised in the Kohn-Sham molecular orbital diagram shown in Figure 5.3. The W-Si bonding is dominated by the degenerate $d_{xz/yz}$ and $d_{x^2-y^2/xy}$ orbitals, which overlap strongly with cluster-based orbitals of e_{1g} and e_{2g} symmetry, respectively . The electrons in these W-Si bonding orbitals play a dual role, contributing both to the cage electron count and to the electron count on the central metal. The LUMO is a non-bonding orbital with dominant metal d_{z^2} character directed along the 6-fold rotational axis, and as a result the electron count on the central metal is 16. The a_{2u}-symmetric HOMO, in contrast, is localised entirely on the Si_{12} cage. In the context of surface binding, the vacant d_{z^2} orbital provides a channel for binding of the metal to the surface layer of the silicon substrate. As was the case for Cr@Si_{14}, some residual Si-Si π bonding

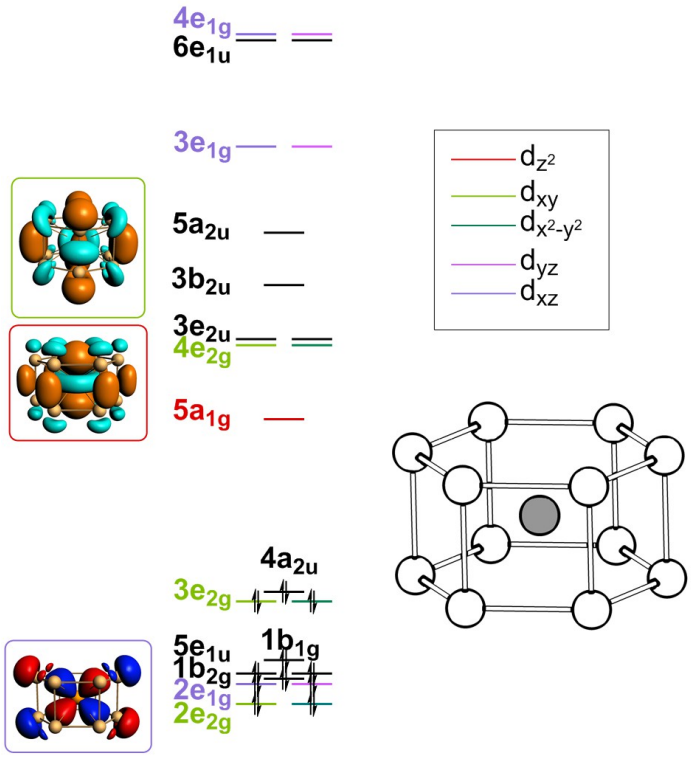


Figure 5.3: Structure of the isolated W@Si_{12} cluster and the Kohn-Sham orbitals

remains in W@Si_{12}, and this unsaturation allows for the formation of strong bonds to the surface silicon atoms.

5.3.2 Structures of the Si(111) surfaces

Overview

Whilst the electronic structure of bulk silicon is very well understood, low-index silicon surfaces are known to undergo complex reconstructions. Historically, surface structural studies relied largely on the low-energy electron diffraction (LEED) technique. LEED measures the diffraction intensities of incident electrons scattered by the first few layers of surfaces, and by matching calculated intensities for various surface models with the experimental data, structures can be established. The majority of studies of silicon have focused on the (111) surface (Figure 5.4a), but within seconds of cleavage this rearranges to give a (2×1) LEED pattern at temper-

atures as low as 9K[232, 233]. There are, inevitably, a large number of possible models that give reasonable fits to the measured data, and as a result many different alternatives have been proposed in the literature. The first widely accepted reconstruction model for the clean Si(111) surface was Haneman's buckling model (Figure 5.4b, which is a 2×2 reconstructed surface), where every second atom along close-spaced rows is raised with respect to its ideal Si(111) position[222]. This model was proposed not long after Farnsworth and Schlier first observed the half-order diffraction beams on the clean cleaved Si(111) surface[232]. In this model, the sp^3 hybridised surface dangling bonds tend to gain more p orbital character, leaving the three bonds connecting to the layer below more sp^2-like, hence pulling the surface atoms into a near planar structure. The stress created by this arrangement is relieved by lifting the central atom of each hexagonal ring out the surface and the dangling bonds on the raised atoms has enhanced s orbital character. Haneman's model was later slightly modified and became Haneman's 2×1 buckling model[234] where alternate rows of atoms in the [110] direction were raised and lowered (not shown in Figure 5.4). However, even with this modification, Haneman's model was unable to explain the results of polarisation-dependent angle-resolved photoemission spectroscopy (ARUPS) experiments reported in the early 1980s'[235, 236]. The ARUPS data, along with Rowe's study of the core-level binding energy shifts[237], led Pandey to revisit the surface reconstruction problem and propose an alternative 2×1 reconstruction model. Pandey's model[223] contains a top layer with one dangling bond on each atom forming zigzag π bond chains and a second layer with saturated silicon atoms (Figure 5.4c). Northrup and Cohen[238] reported calculations that show that Pandey's model can be easily reached from the buckled Si(111) surface with a barrier of only 0.03 eV per surface atom, suggesting that the π bond chain model should be energetically accessible even at very low temperatures. Pandey's original π bond chain model was, however, inconsistent

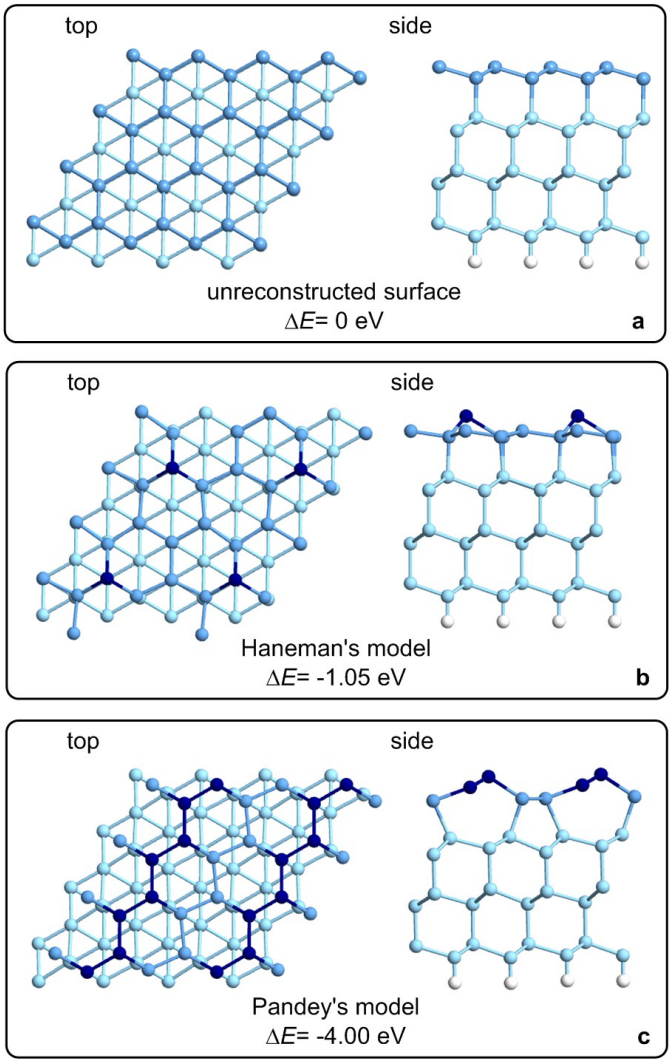


Figure 5.4: (a)The unreconstructed Si(111) surface, surface reconstruction models due to Haneman (b) and Pandey (c). The energy of the unreconstructed surface is set to zero for the surface systems. Lifted surface Si atoms and atoms forming π bond chains are presented by dark blue balls

with subsequent calculated dynamical LEED data reported by Himpsel[239], who proposed a modification by buckling the outer chains. STM images of the 2×1 reconstructed Si(111) surface confirm the presence of the parallel rows of atoms predicted by the π bond chain model[240, 241]. Haneman later proposed an alternative model where the cleavage took place through the three bonds plane which also forms π bond chains[242], but this proved inconsistent with further dynamical LEED study[243]. In summary, Pandey's π bond chain remains the most widely accepted model of the structure of the 2×1 reconstructed Si (111) surface.

Although readily accessible from the unreconstructed surface, even at low temperatures, the 2×1 reconstructed Si (111) surface is not the most thermodynamically stable form of the surface. Through annealing at elevated temperatures, the 2×1 reconstructed Si(111) surface eventually rearranges irreversibly to a more complex 7×7 reconstruction[244, 245]. This 7×7 reconstructed surface is well described by Takayanagi's "dimer-adatom-stacking fault (DAS)" model[246], where the unit cell is divided into faulted and unfaulted halves. Surface adatoms are again present in both halves (shown as dark blue in Figure 5.5), and deep holes that penetrate to the base layer are present at the corners of the unit cell. We note for future reference that the 6 adatoms on each side of the stacking fault are divided into two symmetry-distinct types: three along the edges and three at the corners (notice the three-fold rotation axis at the centre of the faulted/unfaulted half). As a result of its thermodynamic stability, this 7×7 reconstructed Si(111) surface has been widely used to study cluster-surface systems, including the absorption studies of Kanayama that are of direct interest here.

Structure and stability of reconstructed Si(111) surfaces

My initial calculations have focused on the relative stabilities of three distinct models of the Si(111), namely the ideal Si(111), Haneman's 2×2 buckled surface and

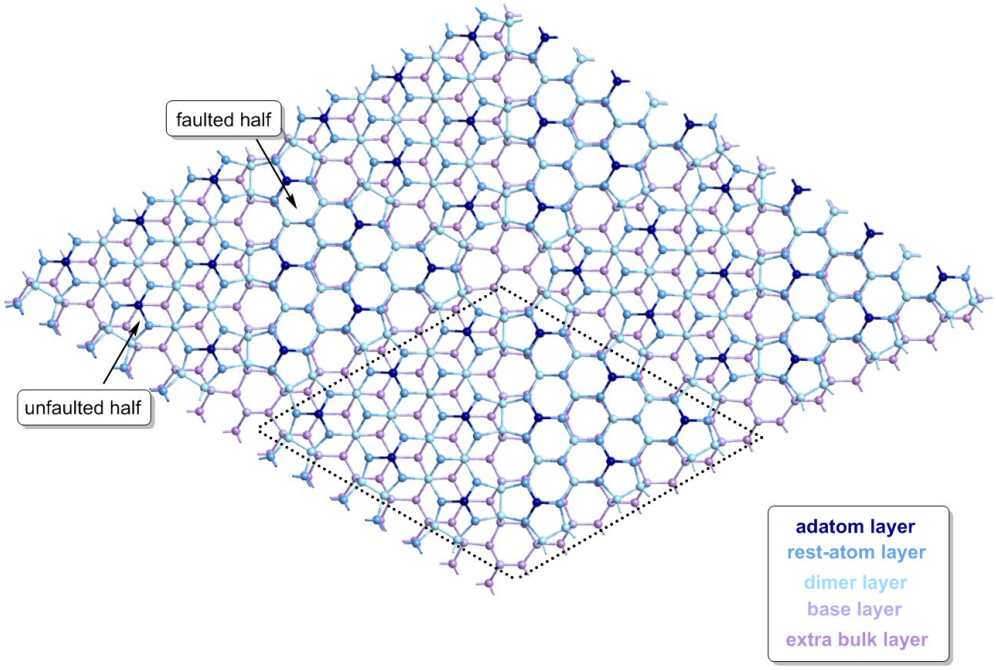


Figure 5.5: 7×7 reconstructed Si(111). Different atom layers are presented in different colours. The dashed line encloses the unit cell

Pandey's 2×1 reconstructed π bond chain. In each case, we used a 4×4 expansion of the primitive cell with 8 layers of silicon atoms terminated with one layer of hydrogen atoms as our unit cell. In the optimisations, all atoms were allowed to relax. Of the three models, Pandey's π bond chain model is the most stable, lying 0.250 eV per surface Si atom lower in energy than the ideal Si (111) surface. Haneman's buckled surface is also more stable than the unreconstructed (111), but only by 0.066 eV per surface atom. Moreover, optimisation starting from Haneman's 2×1 buckling model relaxed spontaneously to Pandey's π bond chain surface, confirming the latter to be the most stable.

In order to make the calculations tractable, our studies of the 7×7 reconstructed surface shown in Figure 5.5 were limited to a shallower unit cell the with only five layers of silicon, rather than the eight used for the Haneman and Pandey models. The four surface layers include the adatom layer, the rest-atom layer, the dimer layer and the base layer, (from the top to the bottom). We also include an extra

bulk layer that is saturated with hydrogen atoms. The minimal number of silicon atoms needed to model the 7×7 unit cell is 151 (excluding the extra bulk layer), which is not an integer multiple of the number of silicon atoms in the clean cleaved Si(111) surface model (in our case, 128), and so it is not possible to compare the stability of this 7×7 reconstructed Si(111) surface with the clean cleaved Si(111) alternatives. Nevertheless, the optimised structure of the 7×7 surface is clearly very close to Takayanagi's "DAS" model, with prominent adatoms on both the faulted and unfaulted halves.

5.3.3 Structure of the cluster-surface system: WSi_{12} on Si(111)

WSi_{12} absorption on 7×7 reconstructed Si(111) surfaces

We begin our analysis of the geometry of surface absorption using the largest 7×7 reconstructed model of the silicon surface, simply because that provides the most direct connection to Kanayama's experimental data. We note from the outset, however, that such a model will be intractable for the studies of electron-transport behaviour to be reported later, where, as emphasised by Datta[224], a deep unit cell with several sub-surface layers is necessary as a result of the semi-conducting nature of the substrate. We therefore then move to the simpler clean cleaved models of the surface (Haneman's buckling model and Pandey's 2×1 reconstructed surface) with a smaller number of atoms in each layer, with the aim of establishing whether similar absorption geometries emerge.

The structure of the molecule-surface interface was explored by docking the pre-optimised $W@Si_{12}$ cluster onto different sites of the 7×7 reconstructed Si(111) surface. The structures and relative energies of stable structures that lie within 1 eV energy of the most stable one (Structure A) are presented in Figure 5.6, along with one, E, that is much less stable. Structures A and C correspond to adsorption on the

unfaulted half of the 7×7 reconstructed unit cell, where the W atom sits above the two symmetry-distinct types of adatom on the unfaulted surface (shown in dark blue) – the corner (C) and the edge (A). Structure B is related, at least conceptually, to C by a reflection in the boundary separating the faulted and unfaulted halves. In structure D, in contrast, the cluster binds to the centre of the unit cell, and is not associated with any individual adatom but rather sits on a region of the surface surrounded by 3 adatoms. In the least stable structure E, the cluster bridges the faulted and unfaulted halves of the unit cell, and is largely unperturbed from the isolated W@Si_{12} molecule. The three structures where the cluster binds around the edge of the unit cell (A, B and C) have very short W-Si separations to one adatom on the silicon surface, with W-Si distances of ~2.6 Å in each case. In all three structures, the uppermost Si atoms lie ~4.5 Å above the surface, a value that compares well with Kanayama's upper limit of 4.4 Å for the surface features observed in the STM[51]. In contrast, when the cluster binds near the centre of the unfaulted half of the unit cell (D), there is no obvious new W-Si surface bond: the cluster sits flat on the surface and is stabilised by Si-Si bonds. Finally, in structure E the cluster bridges the boundary between the faulted and unfaulted halves of the unit cell. The four Si atoms of a square face are bound by the four surrounding surface rest-atoms (two on each side of the boundary). This orientation will present the opposite square face to the STM tip, and might, therefore, be responsible for Kanayama's double-stripe feature. However, the relative instability of structure E along with the high elevation of the cluster above the surface (5.5 Å), suggest that it is unlikely to form the prominent feature in the STM images.

WSi_{12} on clean cleaved Si(111) surfaces

We noted previously that calculation of electron transport properties of the surface absorbed species will be intractable for the 7×7 model due to the number of atoms

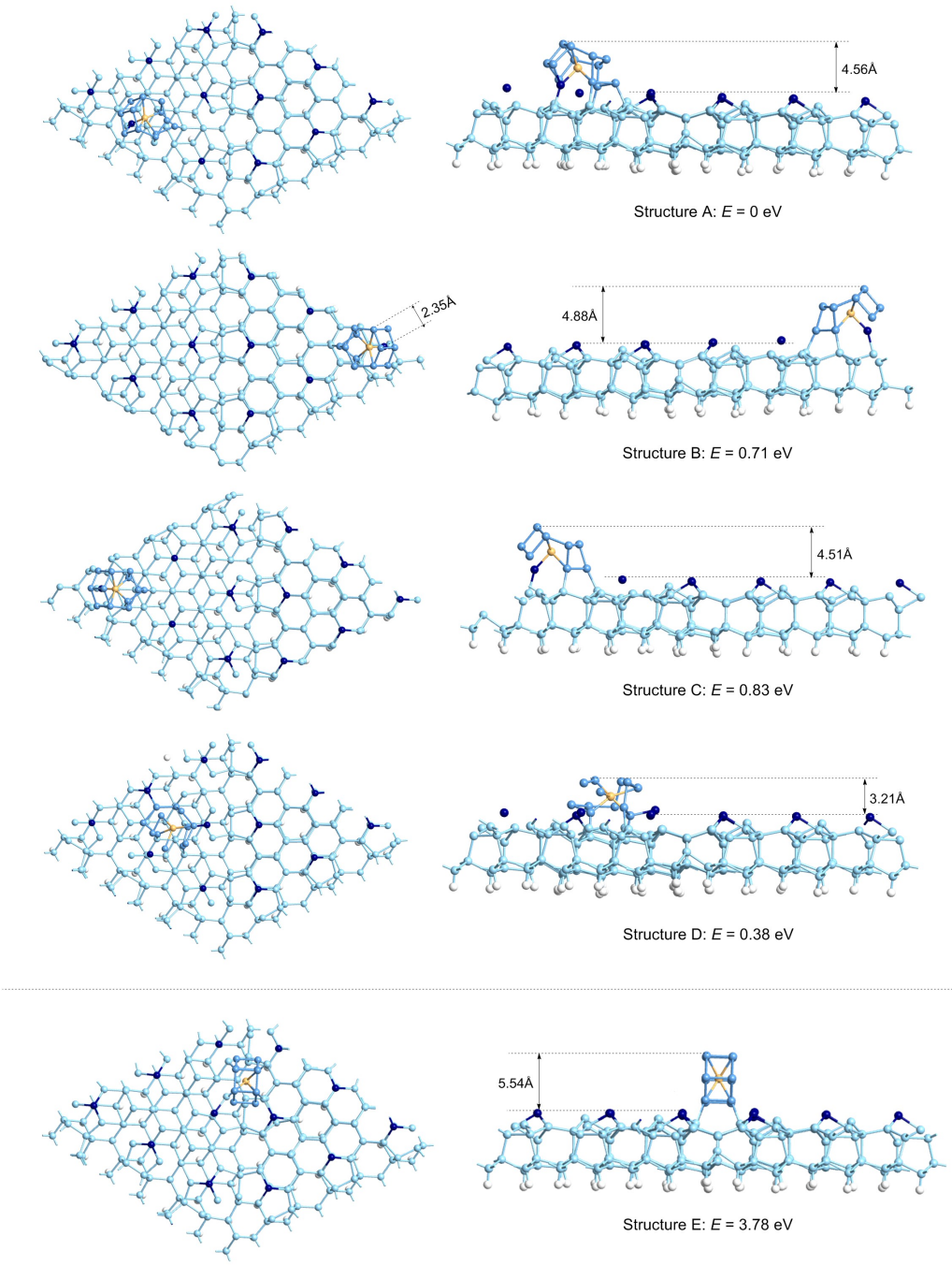


Figure 5.6: Geometries of 7×7 reconstructed Si(111) surface-bound clusters. Adatoms of the surface are highlighted by dark blue balls

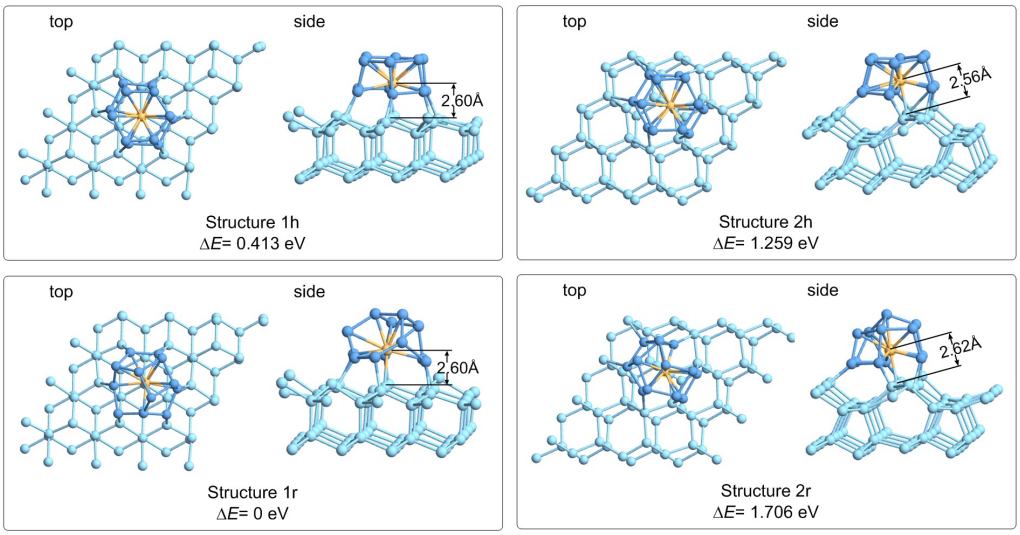


Figure 5.7: Geometries of surface-bound clusters. Structure 1r is taken as the zero of energy for the cluster-surface systems. Cluster Si atoms are in darker blue and the metal atom is in yellow

in each layer. We therefore turn now to the simpler clean cleaved Si(111) surfaces models of Haneman and Pandey to establish whether binding geometries similar to those identified on the 7×7 surface also emerge. The three models of the clean cleaved Si(111) surfaces are shown in Figure 5.4, and in each case, the structure of the molecule-surface interface was explored by docking the pre-optimised W@Si_{12} cluster onto different sites of the silicon surface. To reduce the cost of the calculations, we have used surfaces with six rather than eight layers of silicon atoms with the bottom two layers of Si atoms fixed. The optimised geometries using the simplified surfaces do not differ significantly from the optimised geometries using eight layered surfaces. In the initial configurations, the cluster was oriented so that the surface interacts with either a hexagonal face or a rectangular face. The four most stable structures found in our calculations are presented in Figure 5.7 (1h, 1r, 2h, 2r). Optimisations starting from Haneman's buckled structure[222] and the unreconstructed surface yields exactly the same final configuration, denoted 1h (h for docking via a hexagonal face) and 1r (r for docking via a rectangular face). In contrast, optimisations starting from Pandey's 2×1 reconstruction[223] led

to quite different structures, 2h and 2r, where the surface reconstruction remains despite the binding of the cluster. Of these, the cluster bound to the unreconstructed/Haneman surface (1h, 1r) is more stable than that bound to Pandey's π bond chain 2×1 (2h, 2r) by between 1 and 2 eV (structure 2h is 0.85 eV less stable than structure 1h while structure 2r is 1.71 eV less stable than structure 1r, which is the global minimum found in our calculation). Recalling that the Pandey reconstruction is significantly more favourable for the pristine surface, these results suggest that the surface adsorption reverses the effects of surface reconstruction. Illas and co-workers[247] have emphasised similar points in their work on group III metal adatoms on Si (111) and Ge(111) surfaces, where the energetics of substrate binding also exceed that of reconstruction. In this case, it seems that binding of the cluster overrides the driving force for reconstruction, which indicates that the adsorption process might cause a rearrangement in the surface if the energy barrier is surmountable. The reversal in stability of the reconstructed and unreconstructed surfaces can be understood at a qualitative level based on the distribution of available electrons on alternative substrates (Figure 5.7). It is clear that the 3-fold symmetry of the electrons in 'dangling bonds' of the unreconstructed surface is more compatible with the 6-fold rotation axis of the cluster. The cluster can easily stabilise the unreconstructed surface by terminating seven of its dangling bonds without having to distort itself too much. On Pandey's 2×1 reconstructed surface, however, bonding to the surface occurs in a '4 + 2' mode where the cluster bridges the gap between two parallel zig-zag π-bonded chains. Not only does the cluster have to distort to gain a better overlap with surface orbitals, the connection between the cluster and the surface locally perturb to the surface π-bond, which was the driving force to form the 2×1 reconstruction in the first place. A closer look at the optimised structures 1h and 2h shown in Figure 5.7 confirm that the hexagonal prismatic structure of the isolated cluster is retained after surface adsorption, al-

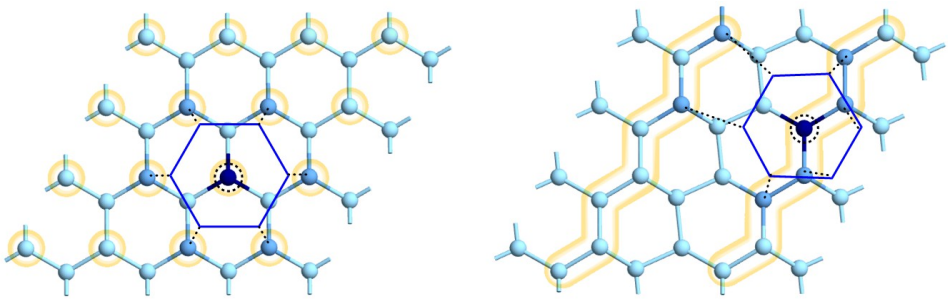


Figure 5.8: Schematic picture of surface-absorbed W@Si_{12}. Approximate positions of surface valences are indicated by yellow circles

beit in a somewhat distorted form. Adsorption on the Haneman/unreconstructed surface gives an approximately 3-fold symmetric structure where each of the six Si atoms in the lower half of the cluster is connected to one substrate silicon atom. The six Si atoms in the upper layer of the cluster remain approximately in their original positions. The binding geometry places the W atom directly above one surface silicon atom, which is lifted out of the surface to form a short W-Si distance (~2.60 Å), precisely as was observed for the 7×7 surface. The structure of the cluster on the 2×1 reconstructed surface is not too different, although the distortion is more pronounced. Again, a W-Si bond is formed to one of the surface silicons from the (π-bonded chain), this time with a W-Si distance of 2.56 Å. Turning to the structures located from approach of the rectangular face of the cluster, we have been unable to locate any minimum analogues to structure E on the 7×7 surface. This is perhaps unsurprising given the very high energy of E, and although the WSi_{12} cluster is still intact in the most stable structures, 1r and 2r, the rectangular face opens up, such that six silicon atoms of the cluster, rather than four, are connected directly to the surface layer. A hexagonal base is therefore common to all four structures 1h, 2h, 1r and 2r, as is the formation of a short W-Si bond to one atom of the surface layer. The structures of the cluster in 1r and 2r differ from those in 1h and 2h most obviously in the arrangement of Si atoms in the upper layer: distinguishable rectangular faces are found in the upper half of the former. It is worth

noting that in all four structures the silicon atoms of the cluster retained their low connectivity, being approximately 3- or 4- connected as they were in the isolated cluster. As analysed in earlier chapters, the 3-connected vertices are often seen in relatively electron rich Si clusters where the central metal shares valence electrons with the cage. The retention of this structural feature in the adducts indicates that the connection between the metal atom and the cluster Si atoms is not completely lost after the adsorption and that valence electrons on the central metal still play a vital row in maintaining the integrity of the cluster on the surface. The close structural similarities between structures 2h and 2r and the most stable structures on the 7×7 reconstructed surface (A, B and C) are striking. The comparison to the more stable 1h and 1r is perhaps less obvious, but the short W-Si bond of ~2.60 Å is a common feature in all cases. We have been unable to locate any minimum on the 2×1 reconstructed surface that resembles structure D on the 7×7 surface, but this is unsurprising given that there is no site on either the Haneman or Pandey surfaces that is surrounded trigonally by three surface adatoms. In summary, it seems that the simpler 2×1 models of the surface provide sufficient flexibility to replicate the majority of the important potential binding sites on the experimentally used but more computationally challenging 7×7 surface. The W-Si distances of around 2.60 Å in all four of the most stable surface adducts suggests that, along with new Si-Si interactions, W-Si bonding is an important contributor to the stability of the adsorbed species. Clear evidence for the presence of a W-Si bond can be found in the Partial Density of States (PDOS), which is projected onto the metal *d* orbitals for 1h, 1r and 2h as examples in Figure 5.9. The most striking feature of the PDOS for structure 1h is the presence of a prominent W d_{z^2} band ~1.3 eV below the Fermi level, with a smaller and more dispersed component in the virtual manifold. The prominent d_{z^2} band below the Fermi level can also be seen in the PDOS for structure 2h, albeit somewhat higher in energy. Recall that the d_{z^2}

orbital in the isolated cluster is localised in the LUMO, and so the presence of d_{z^2} character in the occupied manifold is a clear indication of interactions between the surface and the metal. Compared to the Kohn-Sham orbitals of the isolated cluster, all the other metal d bands are approximately unperturbed by binding to the surface. The $d_{xz/yz}$ and $d_{x^2-y^2/xy}$ bands in structure 1h remain almost degenerate, consistent with the near-perfect 3-fold rotational symmetry of the absorbed cluster. The $d_{xz/yz}$ character in the PDOS of structure 1h appears as two broad bands in the windows –2.0 to –2.5 eV and +1.2 to +2.8 eV: the Si sp contributions to the $2e_{1g}$ and $3e_{1g}$ orbitals in the isolated cluster are oriented outwards from the cluster, and as such are aligned optimally for overlap with the cluster surface, and strong coupling to the surface is responsible for the band broadening. The DOS for structure 1r is qualitatively similar, but the lower symmetry of the cluster makes the projection onto individual angular momentum components less informative. Nevertheless, a prominent metal-localised peak can be found around 1.2 eV below the Fermi level, originated from the LUMO of the free cluster, characterising a W-Si surface bond. Finally, we have also considered the possibility that the cluster loses its integrity entirely upon surface binding. In this case, the 12 additional silicon atoms form a partial mono-layer on the surface, with the metal inserted in either an interstitial or substitutional sites . These structures are ~1 eV higher in energy than 1h and 1r where the cluster remains recognisable. The apparent integrity of the cluster after surface adsorption is consistent with the previous studies[51, 204].

5.3.4 Electron transport pathways in the cluster-surface system: WSi_{12} on Si(111)

In the following discussion, I report calculations of the transmission spectrum of the two most stable cluster-surface models, 1h and 1r, using the non-equilibrium Green's functions technique. This addresses the important question of how elec-

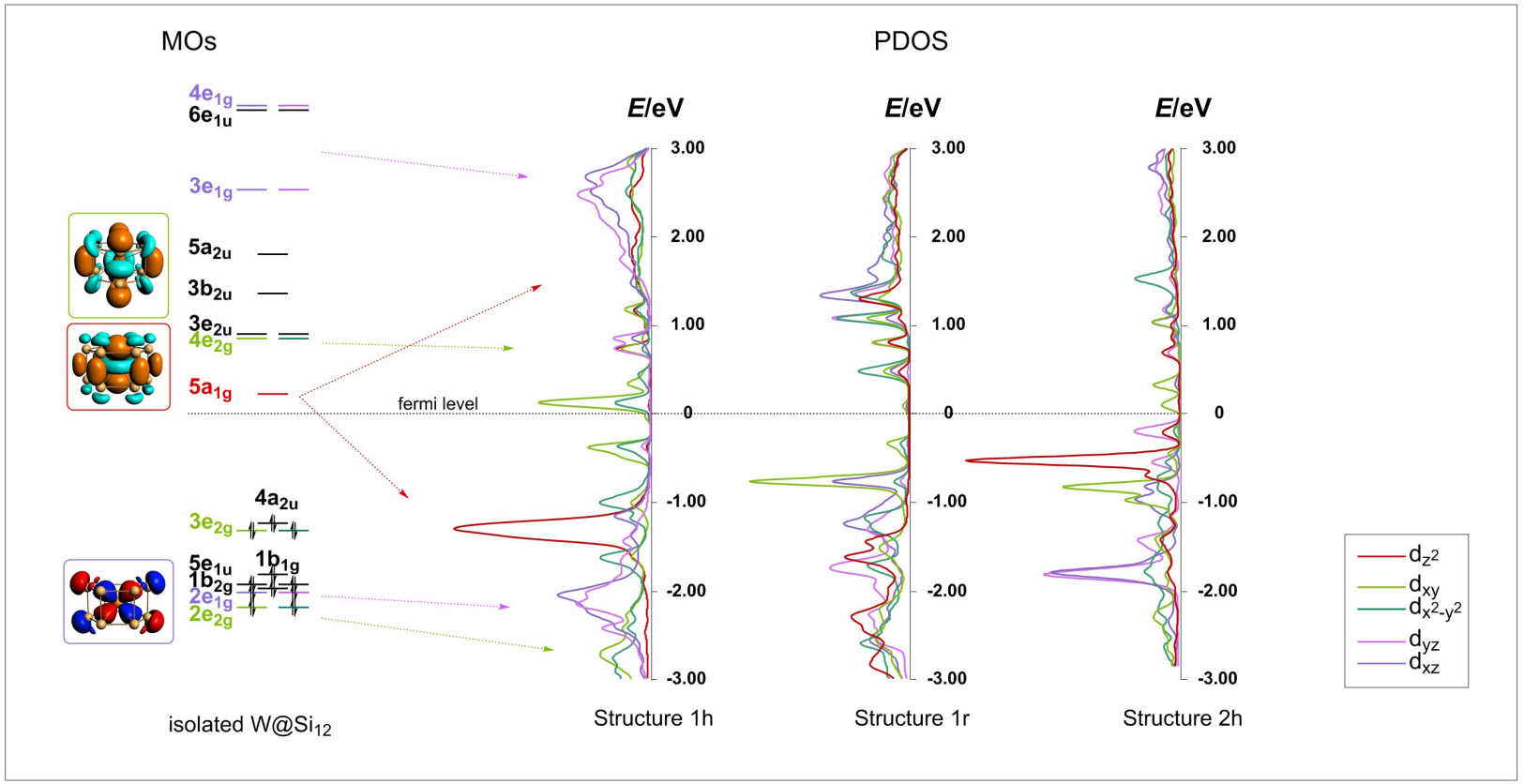


Figure 5.9: Kohn-Sham orbitals of the $W@Si_{12}$ cluster and partial density of states of surface-absorbed $W@Si_{12}$ (structure 1h, 1r and 2h)

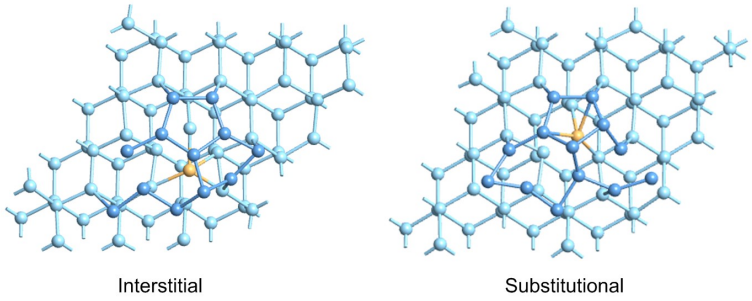


Figure 5.10: Optimised geometry of 'hard-landed' clusters

trons flow from an external source (an STM tip, for example) into the surface or *vice versa*. It is currently not possible to explore the transmission properties of species adsorbed on the 7×7 reconstructed surfaces simply because the number of atoms required to model the STM electrodes of comparable dimensions would be prohibitive. Instead, I will make a few comments on possible electron transport properties of the 7×7 reconstructed surface systems based on the results of our smaller systems at the end of this section.

Device configuration

We have modelled the STM process by setting up a two-probe device (Figure 5.11, upper part) using the Atomistix ToolKit. The left and right electrodes are made up of bulk silicon and bulk gold, respectively, with the W@Si_{12} molecule adsorbed on the surface of the former and a pyramid of gold atoms to model the STM tip on the latter. To model a tunnelling current, it is important to ensure that the tip does not form a chemical bond with any surface atoms. Thus, we need to set the tip far enough from the surface to ensure the presence of a vacuum gap. However, the localised orbitals used in the ATK software means that beyond a particular distance from the core, the amplitude of the basis orbital is set to zero. Therefore, we need to find a compromise distance that exceeds the chemical bonding distance but lies within the cutoff of the confinement potential. In order to determine the bonding

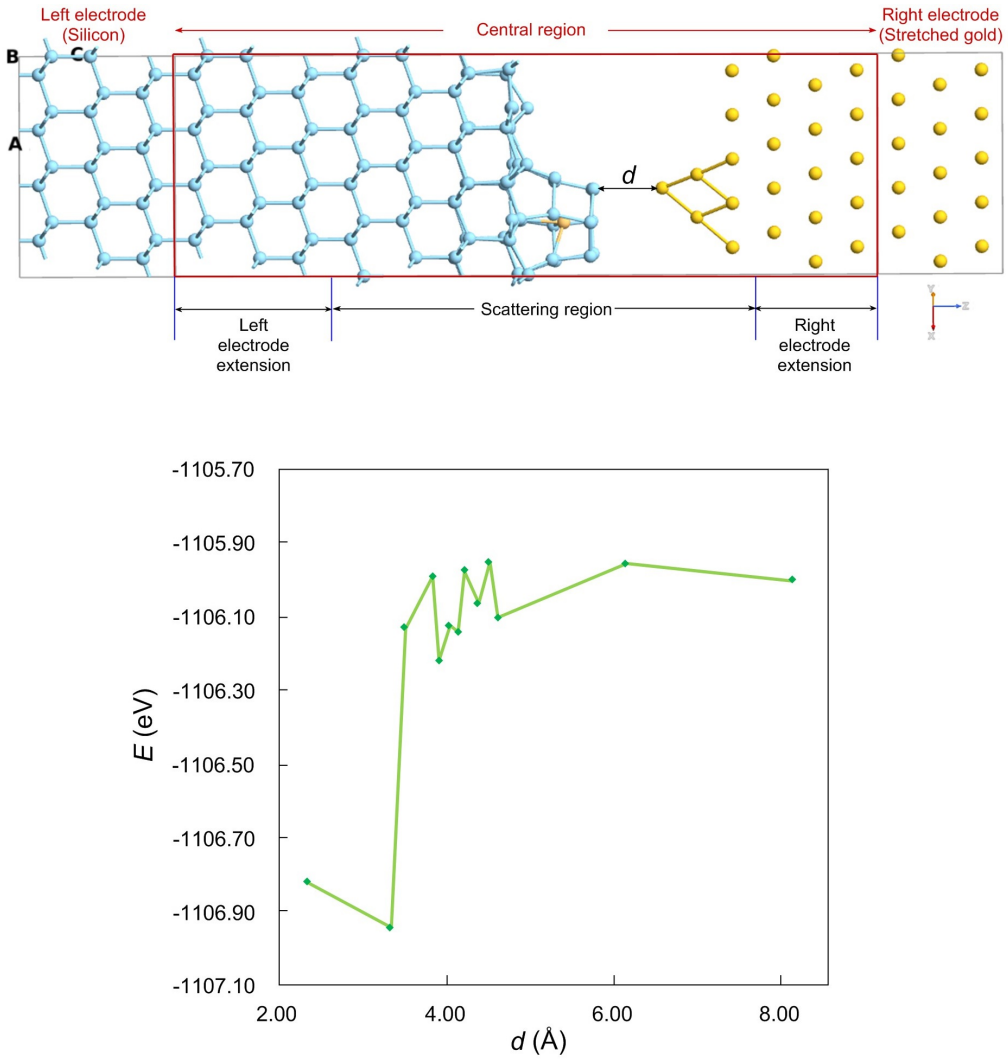


Figure 5.11: The model of the full device (top) and the relationship between tip-surface distance and total energy of the system (bottom)

distance, we have placed the tip above the surface at increasingly large distances and then allowed all cluster atoms, the first two layers of surface Si atoms and the four tip gold atoms to relax while keeping the the other atoms fixed. The total energy after geometry optimisation is plotted against the distance between the tip and the nearest Si atom in Figure 5.11 (lower part). This total energy is at its minimum as the tip bonds with the surface, then rises and starts oscillating around -1106.00 eV, beyond 4.15 Å. The oscillation is caused by noise associated with finite basis set and integration grid, and indicates that the tip is no longer covalently bonded to the surface. We adopt the distance 4.15 Å as the lowest tip-surface atom distance limit in the transport studies. Our first transmission calculation was therefore done with the tip placed 4.15 Å vertically above the highest lying Si atom from the surface side as shown in Figure 5.11 (d = 4.15 Å). Subsequent transmission scans are then performed by moving the tip in the xy plane but keeping its z coordinate fixed.

The Schrödinger equation for an electrode-device-electrode system can be written as[248]:

$$\begin{pmatrix} EI - H_1 + i\eta & -\tau_1^{\dagger} & 0 \\ -\tau_1 & EI - H & -\tau_2 \\ 0 & -\tau_2^{\dagger} & EI - H_2 + i\eta \end{pmatrix} \begin{Bmatrix} \Phi_1 + \chi_1 \\ \psi \\ \Phi_2 + \chi_2 \end{Bmatrix} = \begin{Bmatrix} S_1 \\ 0 \\ S_2 \end{Bmatrix}$$

where H_1, H_2, H are the Hamiltonians for contact 1 (Si), the device channel and contact 2 (Au). τ_1 and τ_2 are the coupling Hamiltonians while Φ_1 and Φ_2 are the eigenfunctions of H_1 and H_2. η is a small positive infinitesimal times the identity matrix which represent the extraction of electron from the contacts while S_1 and S_2 represent the reinjection of electrons from external sources. As the contacts couple with the device channels, device wavefunction ψ would be generated in the device, and in turn, it would excite scattered waves χ_1 and χ_2 in

the contacts. The Green's function for the device channels can be constructed as $G \equiv [EI - H - \Sigma_1 - \Sigma_2]^{-1}$ where $\Sigma_i = \tau_i G_i \tau_i^\dagger$, $G_i = [EI - H_i + i\eta]^{-1}$. Σ_i are the self-energy matrices of the contacts that show the influences of the contacts on the central device region. Their imaginary parts give the broadening of levels when the device channels couple to the contact. The broadening matrix Γ_i is used to represent $i[\Sigma_i - \Sigma_i^\dagger]$. $\{S\} \equiv \tau_1\{\Phi_1\} + \tau_2\{\Phi_2\}$ can be obtained based on the analysis of isolated contacts systems. We can now write out the probability density matrix as $\{\psi\}\{\psi\}^\dagger = G\{S\}\{S\}^\dagger G^\dagger$. The current can be expressed as the time rate of change in the probability density in the channel. Thus it could be obtained by taking the time derivative of the probability density. The current can be eventually written in the form down below:

$$\begin{aligned} I &= \frac{e}{2\pi\hbar}\int_{-\infty}^{+\infty} \mathrm{d}\varepsilon \mathrm{Trace}[\Gamma_1 G \Gamma_2 G^\dagger][f(\varepsilon - E_F - eV) - f(\varepsilon - E_F)] \\ &= \frac{e}{2\pi\hbar}\int_{-\infty}^{+\infty} \mathrm{d}\varepsilon \overline{T}(\varepsilon)[f(\varepsilon - E_F - eV) - f(\varepsilon - E_F)] \end{aligned}$$

where E_F is the equilibrium electrochemical potential of both contacts under same temperature and no bias and $\overline{T}(\varepsilon) = \mathrm{Trace}[\Gamma_1 G \Gamma_2 G^\dagger]$ is the transmission function. The transmission function is the central variable in this analysis: it represents the probability that an incident electron from the source with a given energy, ε, will emerge in the drain.

One important technical detail in the device calculation is that the lattice parameters of the unit cell in the central region are chosen to match those of bulk Si (a = 15.36 Å), and so they are necessarily slightly incommensurate with those of gold (a = 14.42 Å or 17.30 Å, for a 5×5 and a 6×6 unit cell, respectively). To overcome this problem, we have stretched the 5×5 gold unit cell in all three directions to make it commensurate with the silicon lattice . We have also constructed a device with all other parameters set the same, except for using a 'compressed 6×6 gold unit cell' rather than 'stretched 5×5 gold unit cell'. A comparison of the

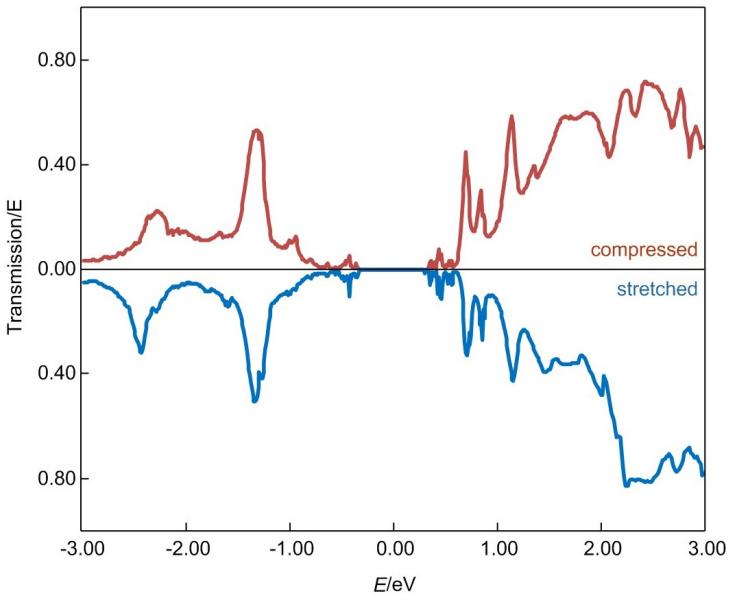


Figure 5.12: Zero-bias transmission spectra of structure 1h using a 'pressed' gold tip (red line), and a 'stretched' gold tip (blue line)

zero-bias transmission spectra of these two devices is presented in Figure 5.12. The two spectra (red and blue line) show no qualitative differences in the important region around the Fermi level, assuring us that the modification to the gold electrode made here does not challenge the validity of our model. In the following sections, we use 'stretched 5×5 gold' to model all gold electrodes.

Zero-bias transmission spectra analysis

The zero-bias transmission spectrum of structure 1h is shown in Figure 5.13 (middle), along with isosurface plots of the Molecular Projected Self-consistent Hamiltonian (MPSH) eigenstates that make the main contributions to transmission at the major peaks (right). The MPSH eigenstates are calculated by diagonalising the submatrix of the self-consistent device Hamiltonian (which considers both central region and probes) associated with selected projection atoms' orbitals. The projection in this case is made onto the cluster, the four gold tip atoms, the seven surface silicon atoms that are connected directly to the cluster and three further

surrounding surface silicon atoms. After the transmission spectrum was calculated using the NEGF method described in earlier sections, then the transmission eigenvalues and eigenstates are analysed for each major transmission peak. At each peak energy, there is only a single dominant transmission eigenstate, indicating that only one channel contributes to each transmission peak. The transmission eigenstate is then projected onto all the MPSH eigenstates to see how large a fraction of a transmission function is propagating through a particular MPSH eigenstate. The MPSH orbitals that carry the most transmission are picked out for each transmission eigenstates and the shapes of their isosurface contour can be compared directly with the Kohn-Sham orbitals of the W@Si_{12} cluster. By analysing the transmission spectrum in this way, we can establish a link from the transmission spectrum all the way back to the orbitals of the isolated cluster. The most significant feature of the zero-bias transmission spectrum of structure 1h is that it possesses only two strong peaks below the Fermi level in the window between -3.0 and 0 eV. The prominent peak at ~1.34 eV is precisely in the region where the W-Si bonding d_{z^2} band was located in the PDOS, and the decomposition of the transmission eigenstates at this energy confirms the relation between this transmission peak and the W-Si bonding d_{z^2} band. The transmission eigenstate contains significant contributions from the 70^{th} and 71^{st} eigenstates of the MPSH, both of which have dominant W d_{z^2} character (the two states differ only in the phase of coupling of the WSi_{12} component to the cluster surface). The high intensity of the peak in the transmission spectrum indicates that the coupling between the cluster and surface is strong, and we can trace this to the strong surface W-Si σ bond that was apparent from the DOS and the short W-Si bond. The complementary peaks above the Fermi level due to the W-Si σ* band are around 1.5 eV and 2.7 eV where the transmission propagate mainly through MPSH orbitals with W d_{z^2}-Si antibonding character. The DOS of the two-probe systems projected onto the device shown in

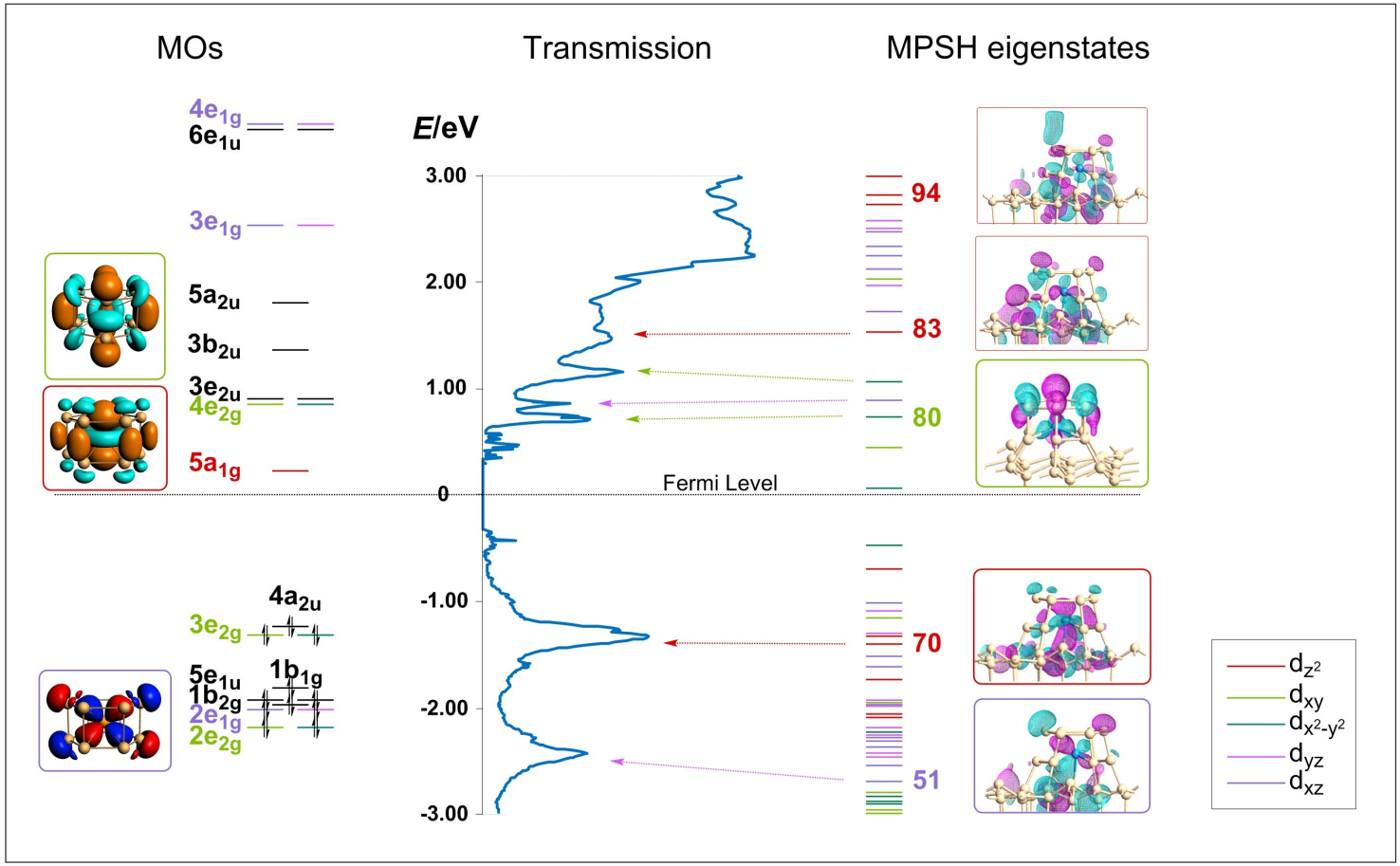


Figure 5.13: From left to right: Kohn-Sham orbitals of W@Si_{12} cluster, zero-bias transmission spectrum of surface-absorbed W@Si_{12} (structure 1h) and corresponding MPSH eigenstates

Figure 5.14 strengthen the argument that the metal d_{z^2} orbital is the dominant feature in the transmission peak at ~1.34 eV. The "device DOS" gives the DOS of the full device system, including the influence of the left and right electrodes on the central region calculated using NEGF method. Thus, it offers a better comparison with the transmission spectrum than does the PDOS of the surface in isolation (*i.e.* without the tip or the two electrodes, as in Figure 5.9). By summing over orbitals of several specific atoms, we can then project the device density of states onto its individual components (PDDOS). From Figure 5.14, we can see that when the projection is made onto all device atoms, there is no obvious feature that corresponds to the transmission peak at -1.34 eV. However, when the projection is restricted to the cluster and the surface silicons bonded to W (*i.e.* a W@Si_{13} unit), a feature at this energy emerges and becomes even more pronounced when all silicon atoms are removed from the projection (note the different horizontal scales in the three plots). The PDDOS in the latter case bears a striking resemblance to the transmission spectrum, confirming that the transmission channel around -1.34 eV is indeed contributed mainly from the metal d band. The other significant peak below E_f in the transmission spectrum occurs at –2.44 eV with contributions from three MPSH eigenstates 51, 55, 56, all of which have dominant W $d_{xy/yz}$ character. They can be traced back through the broad and intense feature in the PDOS in Figure 5.8 at ~-2.3 eV to the $2e_{1g}$ W-Si bonding orbital of the parent cluster. Different metal d bands overlaps more in energy above the Fermi level, making it harder to interpret the transmission result. Nevertheless, through our projection calculation, it is clear that the first broad peak above E_f at ~+0.75 eV propagates through MPSH eigenstate 80, which originates from the empty $4e_{2g}$ orbital of the isolated cluster. This analysis highlights the point that although the cluster is clearly greatly perturbed by the interaction with the surface, characteristic features of its electronic structure can still be identified in the transmission spectrum. Based on the trans-

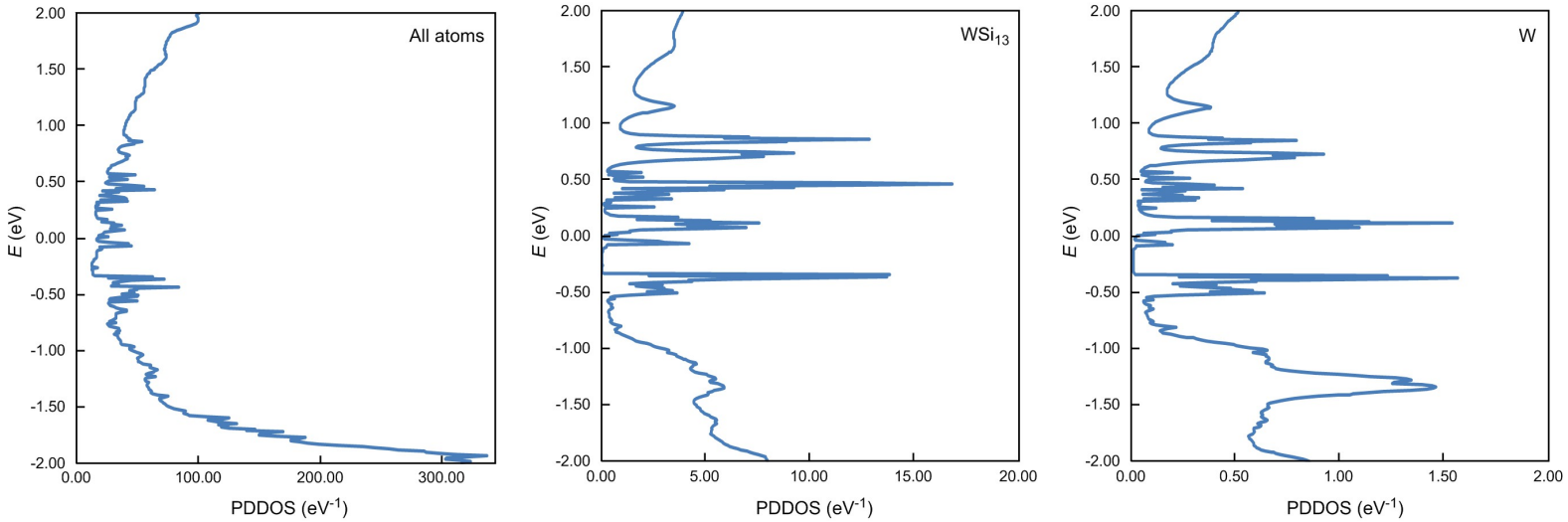


Figure 5.14: Projected device density of states where the projection is made onto all device atoms (left), the cluster plus the surface silicon bonded directly to W atom (middle), and the W atom only (right)

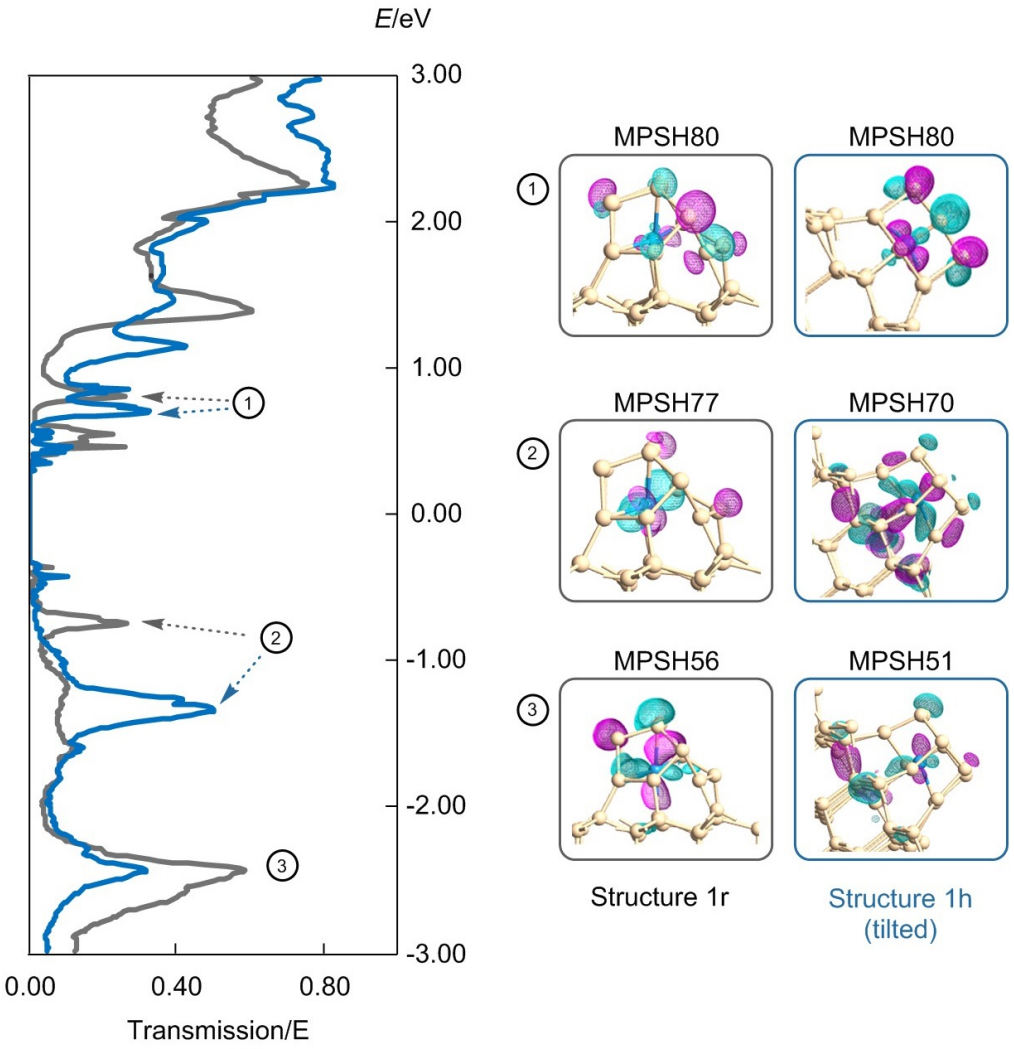


Figure 5.15: Zero-bias transmission spectra of structure 1h (blue line) and zero-bias transmission spectrum of structure 1r (dark grey line) along with MPSH eigenstates which contribute to the transmission channels of three major peaks

mission spectrum, we can infer that an STM scan in negative mode (*i.e.* probing the occupied manifold of the cluster) using a tip bias between 1 and 2 eV will be dominated by contributions from the d_{z^2} band. Increasing the negative bias would lead to the involvement of the $d_{xy/yz}$ band, while in a positive scan mode, the STM current would be made up of contributions from many different surface states. As discussed above, the cluster in structure 1r is noticeably more distorted by binding to the surface, and the fact that there is no longer a recognisable rotation axis

along the surface normal makes it more difficult to project the transmission onto individual angular momentum components in a meaningful way. Nevertheless, the cluster is still recognisable and there are in fact many similarities between the transmission spectrum of this structure and that of structure 1h. Compared with the geometry of the cluster in structure 1h, the cluster in structure 1r is tilted and the d_{z^2} orbital of the isolated W@Si_{12} now points approximately in the yz direction. In Figure 5.15, we compare the two transmission spectra of structure 1h and 1r. Although quantitatively different, the peaks in the transmission spectra of 1h and 1r have many features in common. In the range 0.00 to -3.00 eV, we see a sharp peak splits into two components at ~-0.75 eV, followed by another significant peak around -2.50 eV. By projecting the transmission eigenstates onto the MPSH eigenstates of structure 1r, we see that the peak around -0.75 eV in the spectrum of structure 1r propagates through the 76^{th} and 77^{th} MPSH eigenstates, while the peak around -2.50 eV has large contributions from the 52^{nd}, 53^{rd} and 56^{th} MPSH eigenstates. If we compare the isosurface contours of the 76^{th} and 77^{th} MPSH eigenstates, we can identify these two as the analogues of MPSH 70 and 71 in structure 1h: both originate from the LUMO of the isolated cluster and are displaced below the Fermi level through their participation in the W-Si surface bond. The fact that the corresponding transmission peak lies higher in energy in structure 1r than in structure 1h may be a result of the different orientation: the overlap between the metal d_{z^2} orbital and the surface 'dangling orbital' is less ideal in structure 1r, and as a result the W-Si σ transmission peak appears at higher in energy. The 52^{nd}, 53^{rd} and 56^{th} MPSH eigenstates are the equivalents of 51, 55 and 56, in structure 1h, and derive from the $2e_{1g}$ orbital of the parent cluster. The analysis on the transmission spectrum of structure 1r again emphasises the point that characteristic features of the isolated cluster are to a large extent preserved after adsorption.

Spatial profile for the transmission

One of the key features of the STM technique is that is affords a spatial profile of the surface which resulted. We can model this spatial profile for the transmission by shifting the STM tip in the xy plane, *i.e.* perpendicular to the transport direction, while maintaining it in a fixed z position above the silicon surface. Several distinct tip positions are shown in Figure 5.16, with the corresponding transmission spectra. The positions and shapes of the main peaks remain almost constant when the tip shifts, indicating that these features are determined primarily by the cluster-substrate interaction rather than the precise position of the tip. The variations in intensity of the peaks show how well the tip bands communicate with the surface bands. We see, therefore, that when the tip is moved well away from the cluster (spectrum 4 in 1h, spectrum 3 in 1r), the transmission drops close to zero. In structure 1h, the intensity of the d_{z^2} transmission peak around -1.3 eV increases, albeit only to a small degree, as the tip moves away from the centre of the cluster (position 1) towards the atoms of the upper Si_6 ring. The MPSH plots (70 and 71) shown in Figure 5.13 emphasise the significant Si p character which protrudes above the surface of the cluster to a much greater extent than the d_{z^2} orbital itself. Moving the tip off centre therefore enhances the overlap with the cluster and increases the transmission amplitude. Conversely, the opposite effect is seen in the band at +1.2 eV, which increases in intensity as the tip moves to the centre of the cluster. In this case, the eigenstates of the MPSH have W $d_{xy/yz}$ character, and position 3 lies in a nodal plane. The density of states therefore decreases near the periphery of the Si_6 ring, as does the transmission.

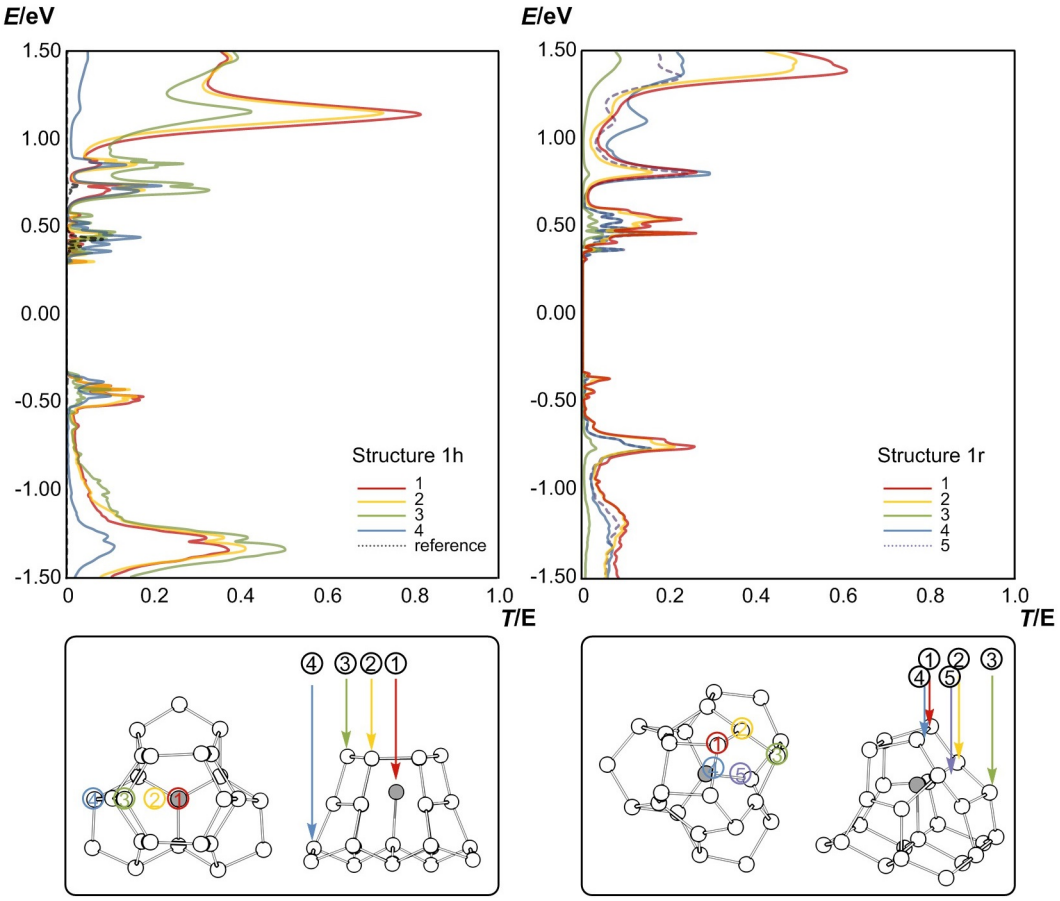


Figure 5.16: Spatial profile for the transmission spectra of surface models 1h and 1s. The dashed line on the left is a reference line, where the tip is placed far from the cluster

Extension to the transport properties of the WSi_{12}-7×7 reconstructed Si(111) systems

We have emphasised the importance of the metal d bands in the transmission with the WSi_{12}-unreconstructed Si(111) systems and we have shown in Figure 5.6 that in three of the most stable structures on the 7×7 reconstructed surface, there is a Si-W surface bond that provides a transmission pathway from the tip into the silicon bulk. In Figure 5.9, we showed that the position of the metal d bands depends on the orientation of the cluster. In structure 1h, the metal d_{z^2} band below the Fermi level is lower in energy than the corresponding metal d bands in structure 1r (the $d_{xz/xy}$ band) and structure 2h (the d_{z^2} band). This is very possibly due to a better overlap of the metal d_{z^2} and the dangling valence of the silicon atom in structure 1h, where the trigonal symmetry of the cluster is commensurate with that of the surface. For the WSi_{12}-7×7 reconstructed Si(111) systems with a W-Si surface bond, namely structure A-C, it is clear that the surface Si-W bond is not aligned perpendicular to the surface, as it is in 1h and 1r, but at an angle as in 2h and 2r. Thus, we should expect either a d_{z^2} band peak just below the Fermi level or a strong $d_{xz/xy}$ band peak well below Fermi level, or both. For structure D in Figure 5.6, where the metal did not form bonds with silicon adatoms, the d_{z^2} peak is likely to be less prominent and clusters in such a configuration may be transparent.

5.4 Summary

In this chapter, we have explored the geometry and electronic structure of the surface-absorbed W@Si_{12} cluster. We have shown that although the configuration of the system is dependent on the choice of model surface, there are some common features that emerge in all cases. The Si-Si bonds that link the cluster to the surface are not fundamentally different from those in the bulk silicon, and so the

metal encapsulating cluster becomes an 'extension' of the surface. Nevertheless, the structure is still identifiably 'cluster-like' and we can trace the dominant transmission channels back to the molecular orbital array of the cluster itself, showing that the cluster therefore retains at least some of its structural integrity, but also preserves a large part of its electronic character and can be viewed as an electronically unique entity. The d orbitals of the central metal atom, and in particular the vacant d_{z^2}, play a critical role, both in the energetics of absorption and also in the transmission of electrons.

Summary

To summarise, this thesis has been concerned with the electronic structure of tetrel clusters containing endohedral transition metal atoms. Chapter 1 reports a review of the literature review that shows that, despite the fact that $M_n@E_m$ clusters have been studied by several authors, our understanding remains incomplete. In particular, although a large number of computational studies have been devoted to the question of the structures of these clusters, the reported results are often contradictory and strongly dependent on the details of the computational methodology. There are few papers that address this issue directly, and none give a satisfactory explanation that explains all of the available data. The first results chapter, Chapter 3, focuses on the particularly 'problematic' $M@Si_{14}$ systems where many conflicting claims have been made in the literature. I have shown that there are two different but related routes to form stable $M@E_n$ clusters: the 'fullerene route' and the 'Wade's rule route', and discussed the factors that affect the balance between these two alternatives. Potential sources of functional dependency are also considered in this chapter. In Chapter 4, the stability trends established for the monometallic clusters are extended to polymetallic species, and specifically to the $[Co_2@Ge_{16}]^z$ cluster. I show that the polymetallic analogues are not fundamentally different from the $M@E_n$ clusters in the sense that the competition between the fullerene-like and deltahedral isomers still dominates the structural landscape, and is still affected strongly by the availability of electron density on the transition metals.

In Chapter 5, the last chapter, I explore the configurations of the surface-absorbed cluster W@Si_{12} on different reconstructed Si(111) surfaces. A subsequent electron transport study then illustrates the important point that the surface-absorbed clusters can be regarded as electronically unique entities even though their structures are strongly distorted by the absorption process. Throughout the thesis, the d orbitals on the central transition metal have played a defining role, controlling the structural chemistry of the isolated clusters, the geometries of the surface-bound species and the passage of electrons from an STM tip into the bulk or *vice versa*.

References

(1) S. M. Myers, M. Seibt and W. Schröter, *J. Appl. Phys.*, 2000, **88**, 3795–3819.

(2) A. P. Alivisatos, *Science*, 1996, **271**, 933–937.

(3) S. M. Beck, *J. Chem. Phys.*, 1987, **87**, 4233–4234.

(4) S. M. Beck, *J. Chem. Phys.*, 1989, **90**, 6306–6312.

(5) H. Hiura, T. Miyazaki and T. Kanayama, *Phys. Rev. Lett.*, 2001, **86**, 1733–1736.

(6) X. Zhang, G. L. Li and Z. Gao, *Rapid Commun. Mass Spectrom.*, 2001, **15**, 1573–1576.

(7) X. Zhang, Z. C. Tang and Z. Gao, *Rapid Commun. Mass Spectrom.*, 2003, **17**, 621–626.

(8) J. Atobe, K. Koyasu, S. Furuse and A. Nakajima, *Phys. Chem. Chem. Phys.*, 2012, **14**, 9403–9410.

(9) S. Furuse, K. Koyasu, J. Atobe and A. Nakajima, *J. Chem. Phys.*, 2008, **129**, 064311.

(10) M. Ohara, K. Koyasu, A. Nakajima and K. Kaya, *Chem. Phys. Lett.*, 2003, **371**, 490–497.

(11) K. Koyasu, M. Akutsu, M. Mitsui and A. Nakajima, *J. Am. Chem. Soc.*, 2005, **127**, 4998–4999.

(12) K. Koyasu, J. Atobe, M. Akutsu, M. Mitsui and A. Nakajima, *J. Phys. Chem. A*, 2007, **111**, 42–49.

(13) M. Ohara, K. Miyajima, A. Pramann, A. Nakajima and K. Kaya, *J. Phys. Chem. A*, 2002, **106**, 3702–3705.

(14) Z. F. Chen, S. Neukermans, X. Wang, E. Janssens, Z. Zhou, R. E. Silverans, v. P. King, R. B. and P. Lievens, *J. Am. Chem. Soc.*, 2006, **128**, 12829–12834.

(15) S. Neukermans, E. Janssens, Z. F. Chen, R. E. Silverans, P. von Ragué Schleyer and P. Lievens, *Phys. Rev. Lett.*, 2004, **92**, 163401.

(16) S. Neukermans, X. Wang, N. Veldeman, E. Janssens, R. E. Silverans and P. Lievens, *Int. J. Mass Spectrom.*, 2006, **252**, 145–150.

(17) E. Janssens, P. Gruene, W. L. Meijer, G., P. Lievens and A. Fielicke, *Phys. Rev. Lett.*, 2007, **99**, 063401.

(18) U. Rohrmann, S. Schäfer and R. Schäfer, *J. Phys. Chem. A*, 2009, **113**, 12115–12121.

(19) S. Scharfe, F. Kraus, S. Stegmaier, A. Schier and T. F. Fässler, *Angew. Chem. Int. Ed.*, 2011, **50**, 3630–3670.

(20) P. Jena, *J. Phys. Chem. Lett.*, 2013, **4**, 1432–1442.

(21) E. Janssens, S. Neukermans and P. Lievens, *Curr. Opin. Solid State Mater. Sci.*, 2004, **8**, 185–193.

(22) E. N. Esenturk, J. Fettinger and B. Eichhorn, *J. Am. Chem. Soc.*, 2006, **128**, 9178–9186.

(23) E. N. Esenturk, J. Fettinger, Y. F. Lam and B. Eichhorn, *Angew. Chem. Int. Ed.*, 2004, **43**, 2132–2134.

(24) J. Q. Wang, S. Stegmaier, B. Wahl and T. F. Fässler, *Chem. Eur. J.*, 2010, **16**, 1793–1798.

(25) Y. Wang, L. L. Wang, H. P. Ruan, B. L. Luo, R. L. Sang and L. Xu, *Chinese J. Struct. Chem.*, 2015, **34**, 1253–1258.

(26) B. B. Zhou, T. Krämer, A. L. Thompson, J. E. McGrady and J. M. Goicoechea, *Inorg. Chem.*, 2011, **50**, 8028–8037.

(27) E. N. Esenturk, J. Fettinger and B. Eichhorn, *Chem. Commun.*, 2005, 247–249.

(28) T. Krämer, J. C. A. Duckworth, M. D. Ingram, B. B. Zhou, J. E. McGrady and J. M. Goicoechea, *Dalton Trans.*, 2013, **42**, 12120–12129.

(29) S. Scharfe, T. F. Fässler, S. Stegmaier, S. D. Hoffmann and K. Ruhland, *Chem. Eur. J.*, 2008, **14**, 4479–4483.

(30) V. Hlukhyy, S. Stegmaier, L. van Wüllen and T. F. Fässler, *Chem. Eur. J.*, 2014, **20**, 12157–12164.

(31) E. N. Esenturk, J. C. Fettinger and B. W. Eichhorn, *J. Am. Chem. Soc.*, 2006, **128**, 12–13.

(32) B. Kesanli, J. E. Halsig, P. Zavalij, J. C. Fettinger, Y. F. Lam and B. W. Eichhorn, *J. Am. Chem. Soc.*, 2007, **129**, 4567–4574.

(33) V. Hlukhyy, H. Y. He, L. A. Jantke and T. F. Fässler, *Chem. Eur. J.*, 2012, **18**, 12000–12007.

(34) Z. M. Sun, H. Xiao and L. S. Wang, *J. Am. Chem. Soc.*, 2007, **129**, 9560–9561.

(35) J. M. Goicoechea and S. C. Sevov, *J. Am. Chem. Soc.*, 2005, **127**, 7676–7677.

(36) J. M. Goicoechea and S. C. Sevov, *Angew. Chem. Int. Ed.*, 2005, **44**, 4026–4028.

(37) X. Jin, G. Espinoza-Quintero, B. Below, V. Arcisauskaite, J. M. Goicoechea and J. E. McGrady, *J. Organomet. Chem.*, 2015, **792**, 149–153.

(38) C. Liu, I. A. Popov, L. J. Li, N. Li, A. I. Boldyrev and Z. M. Sun, *Chem. Eur. J.*, 2017, **23**, 1–8.

(39) J. Q. Wang, S. Stegmaier and T. F. Fässler, *Angew. Chem. Int. Ed.*, 2009, **48**, 1998–2002.

(40) B. B. Zhou, M. S. Denning, D. L. Kays and J. M. Goicoechea, *J. Am. Chem. Soc.*, 2009, **131**, 2802–2803.

(41) G. Espinoza-Quintero, J. C. A. Duckworth, W. K. Myers, J. E. McGrady and J. M. Goicoechea, *J. Am. Chem. Soc.*, 2014, **136**, 1210–1213.

(42) S. Mitzinger, L. Broeckaert, W. Massa, F. Weigend and S. Dehnen, *Chem. Commun.*, 2015, **51**, 3866–3869.

(43) W. J. Zheng, J. M. Nilles, D. Radisic and K. H. Bowen Jr., *J. Chem. Phys.*, 2005, **122**, 071101.

(44) S. N. Khanna, B. K. Rao and P. Jena, *Phys. Rev. Lett.*, 2002, **89**, 016803.

(45) J. T. Lau, K. Hirsch, P. Klar, A. Langenberg, F. Lofink, R. Richter, J. Rittmann, M. Vogel, V. Zamudio-Bayer and T Möller, *Phys. Rev. A*, 2009, **79**, 053201.

(46) V. Kumar and Y. Kawazoe, *Phys. Rev. Lett.*, 2001, **87**, 045503.

(47) V. T. Ngan, E. Janssens, P. Claes, J. T. Lyon, A. Fielicke, M. T. Nguyen and P. Lievens, *Chem. Eur. J.*, 2012, **18**, 15788–15793.

(48) P. Claes, E Janssens, V. T. Ngan, P. Gruene, J. T. Lyon, D. J. Harding, A. Fielicke, M. T. Nguyen and P. Lievens, *Phys. Rev. Lett.*, 2011, **107**, 173401.

(49) V. Kumar, C. Majumder and Y. Kawazoe, *Chem. Phys. Lett.*, 2002, **363**, 319–322.

(50) Z. H. Sun, H. Oyanagi, N. Uchida, T. Miyazaki and T. Kanayama, *J. Phys. D: Appl. Phys.*, 2009, **42**, 015412.

(51) N. Uchida, L. Bolotov, T. Miyazaki and T. Kanayama, *J. Phys. D: Appl. Phys.*, 2003, **36**, L43–L46.

(52) A. Spiekermann, S. D. Hoffmann and T. F. Fässler, *Angew. Chem. Int. Ed.*, 2006, **45**, 3459–3462.

(53) L. F. Cui, X. Huang, L. M. Wang, J. Li and L. S. Wang, *J. Phys. Chem. A*, 2006, **110**, 10169–10172.

(54) L. F. Cui, X. Huang, L. M. Wang, D. Y. Zubarev, A. I. Boldyrev, J. Li and L. S. Wang, *J. Am. Chem. Soc.*, 2006, **128**, 8390–8391.

(55) L. F. Cui, X. Huang, L. M. Wang, J. Li and L. S. Wang, *Angew. Chem. Int. Ed.*, 2007, **46**, 742–745.

(56) T. B. Tai and M. T. Nguyen, *J. Phys. Chem. A*, 2011, **115**, 9993–9999.

(57) T. B. Tai, N. M. Tam and M. T. Nguyen, *Chem. Phys.*, 2011, **388**, 1–8.

(58) H. Zhang and B. K. Teo, *Inorg. Chim. Acta*, 1997, **265**, 213–224.

(59) A. K. Kandalam, G. Chen and P. Jena, *Appl. Phys. Lett.*, 2008, **92**, 143109.

(60) K. Wade, *J. Chem. Soc. D*, 1971, 792–793.

(61) D. Michael and P. Mingos, *Acc. Chem. Res.*, 1984, **17**, 311–319.

(62) R. W. Rudolph, *Acc. Chem. Res.*, 1976, **9**, 446–452.

(63) J. Wang and J. G. Han, *J. Phys. Chem. A*, 2006, **110**, 12670–12677.

(64) J. Wang and J. G. Han, *J. Phys. Chem. B*, 2006, **110**, 7820–7827.

(65) J. Wang and J. G. Han, *J. Chem. Phys.*, 2005, **123**, 244303.

(66) W. J. Zhao and Y. X. Wang, *J. Mol. Struct.: THEOCHEM.*, 2009, **901**, 18–23.

(67) L. X. -J. and K. H. Su, *Theor. Chem. Acc.*, 2009, **124**, 345–354.

(68) D. Bandyopadhyay and P. Sen, *J. Phys. Chem. A*, 2010, **114**, 1835–1842.

(69) M. Kumar, N. Bhattacharyya and D. Bandyopadhyay, *J. Mol. Model*, 2012, **18**, 405–418.

(70) D. Bandyopadhyay, *J. Mol. Model*, 2012, **18**, 3887–3902.

(71) K. Dhaka, R. Trivedi and D. Bandyopadhyay, *J. Mol. Model*, 2013, **19**, 1473–1488.

(72) K. Dhaka and D. Bandyopadhyay, *RSC Adv.*, 2015, **5**, 83004–83012.

(73) N. Kapila, V. K. Jindal and H. Sharma, *Physica B*, 2011, **406**, 4612–4619.

(74) N. A. Borshch, N. S. Pereslavteza and Kurganskii, *Russ. J. Phys. Chem. B*, 2015, **9**, 9–18.

(75) J. G. Wang, L. Ma, J. J. Zhao and G. H. Wang, *J. Phys.: Condens. Matter*, 2008, **20**, 335223.

(76) C. M. Tang, M. Y. Liu, W. H. Zhu and K. M. Deng, *Comput. Theor. Chem.*, 2011, **969**, 56–60.

(77) J. M. Goicoechea and J. E. McGrady, *Dalton Trans.*, 2015, **44**, 6755–6766.

(78) V. Kumar and Y. Kawazoe, *Appl. Phys. Lett.*, 2003, **83**, 2677–2679.

(79) M. M. Uţă, D. Cioloboc and R. B. King, *Inorg. Chem.*, 2012, **51**, 3498–3504.

(80) G. L. Li, X. Zhang, Z. C. Tang and Z. Gao, *Chem. Phys. Lett.*, 2002, **359**, 203–212.

(81) J. Lu and S. Nagase, *Chem. Phys. Lett.*, 2003, **372**, 394–398.

(82) X. J. Deng, X. Y. Kong, X. L. Xu, H. G. Xu and W. J. Zheng, *Chem. Phys. Chem.*, 2014, **15**, 3987–3993.

(83) R. B. King, I. Silaghi-Dumitrescu and M. M. Uţă, *Chem. Eur. J.*, 2008, **14**, 4542–4550.

(84) V. Kumar and Y. Kawazoe, *Appl. Phys. Lett.*, 2002, **80**, 859–861.

(85) R. B. King, I. Silaghi-Dumitrescu and M. M. Uţă, *Inorg. Chem.*, 2006, **45**, 4974–4981.

(86) R. B. King, I. Silaghi-Dumitrescu and M. M. Uţă, *Dalton Trans.*, 2007, 364–372.

(87) M. M. Bentlohner, C. Fischer and T. Fässler, *Chem. Commun.*, 2016, **52**, 9841–9843.

(88) M. B. Abreu, A. C. Reber and S. N. Khanna, *J. Chem. Phys.*, 2015, **143**, 074310.

(89) J. Wang, Y. Liu and Y. C. Li, *Phys. Lett. A*, 2010, **374**, 2736–2742.

(90) F. C. Chuang, C. C. Hsu, Y. Y. Hsieh and M. A. Albao, *Chin. J. Phys.*, 2010, **48**, 82–102.

(91) J. R. Li, G. H. Wang, C. H. Yao, Y. W. Mu, J. G. Wan and M. Han, *J. Chem. Phys.*, 2009, **130**, 164514.

(92) J. R. Li, C. H. Yao, Y. W. Mu, J. G. Wan and M. Han, *J. Mol. Struct.: THEOCHEM.*, 2009, **916**, 139–146.

(93) Q. Peng and J. Shen, *J. Chem. Phys.*, 2008, **128**, 084711.

(94) L. J. Guo, G. F. Zhao, Y. Z. Gu, X. Liu and Z. Zeng, *Phys. Rev. B*, 2008, **77**, 195417.

(95) D. Bandyopadhyay, *J. Appl. Phys.*, 2008, **104**, 084308.

(96) D. Bandyopadhyay and M. Kumar, *Chem. Phys.*, 2008, **353**, 170–176.

(97) J. G. Wang, J. J. Zhao, L. Ma, B. L. Wang and G. H. Wang, *Phys. Lett. A*, 2007, **367**, 335–344.

(98) J. Wang, Q. M. Ma, Z. Xie, Y. Liu and Y. C. Li, *Phys. Rev. B*, 2007, **76**, 035406.

(99) L. Ma, J. J. Zhao, B. L. Wang, Q. L. Lu and G. H. Wang, *Phys. Rev. B*, 2006, **73**, 125439.

(100) P. Guo, Z. Y. Ren, A. P. Yang, J. G. Han, J. Bian and G. H. Wang, *J. Phys. Chem. A*, 2006, **110**, 7453–7460.

(101) J. Wang and J. G. Han, *J. Chem. Phys.*, 2005, **123**, 064306.

(102) H. Kawamura, V. Kumar and Y. Kawazoe, *Phys. Rev. B*, 2004, **70**, 245433.

(103) J. Lu and S. Nagase, *Phys. Rev. Lett.*, 2003, **90**, 115506.

(104) J. Ulises Reveles and S. N. Khanna, *Phys. Rev. B*, 2005, **72**, 165413.

(105) J. Ulises Reveles and S. N. Khanna, *Phys. Rev. B*, 2006, **74**, 035435.

(106) J. Wang, Q. M. Ma, R. P. Xu, Y. Liu and Y. C. Li, *Phys. Lett. A*, 2009, **373**, 2869–2875.

(107) M. B. Torres, E. M. Fernández and L. C. Balbás, *Phys. Rev. B*, 2007, **75**, 205425.

(108) D. Palagin, M. Gramzow and K. Reuter, *J. Chem. Phys.*, 2011, **134**, 244705.

(109) H. Kawamura, V. Kumar and Y. Kawazoe, *Phys. Rev. B*, 2005, **71**, 075423.

(110) M. B. Abreu, A. C. Reber and S. N. Khanna, *J. Phys. Chem. Lett.*, 2014, **5**, 3492–3496.

(111) G. Mpourmpakis and G. E. Froudakis, *Phys. Rev. B*, 2003, **68**, 125407.

(112) V. Chauhan, M. B. Abreu, A. C. Reber and S. N. Khanna, *Phys. Chem. Chem. Phys.*, 2015, **17**, 15718–15724.

(113) E. N. Koukaras, C. S. Garoufalis and A. D. Zdetsis, *Phys. Rev. B*, 2006, **73**, 235417.

(114) C. Y. Xiao, F. Hagelberg and W. A. Lester Jr., *Phys. Rev. B*, 2002, **66**, 075425.

(115) F. Hagelberg, C. Y. Xiao and W. A. Lester Jr., *Phys. Rev. B*, 2003, **67**, 035426.

(116) A. D. Zdetsis, E. N. Koukaras and C. S. Garoufalis, *J. Math. Chem.*, 2009, **46**, 971–980.

(117) N. Uchida, T. Miyazaki and T. Kanayama, *Phys. Rev. B*, 2006, **74**, 205427.

(118) L. J. Guo, X. H. Zheng, Z. Zeng and C. Zhang, *Chem. Phys. Lett.*, 2012, **550**, 134–137.

(119) T. Miyazaki, H. Hiura and T. Kanayama, *Phys. Rev. B*, 2002, **66**, 121403.

(120) J. G. Han, C. Y. Xiao and F. Hagelberg, *Struct. Chem.*, 2002, **13**, 173–191.

(121) R. L. Johnston and M. P. Mingos, *J. Chem. Soc. Dalton Trans.*, 1987, 647–656.

(122) V. Kumar, *Comput. Mater. Sci.*, 2006, **36**, 1–11.

(123) V. Kumar and Y. Kawazoe, *Phys. Rev. B*, 2002, **65**, 073404.

(124) J. G. He, K. C. Wu, C. P. Liu and R. J. Sa, *Chem. Phys. Lett.*, 2009, **483**, 30–34.

(125) D. J. Griffiths, *Introduction to Quantum Mechanics*, Prentice Hall, Upper Saddle River, 1995.

(126) C. J. Cramer, *Essentials of Computational Chemistry: Theories and Models*, Wiley, Chichester, 2002.

(127) F. Jensen, *Introduction to Computational Chemistry*, Wiley, Chichester, 1999.

(128) A. Szabo and N. S. Ostlund, *Modern Quantum Chemistry: Introduction to Advanced Electronic Structure Theory*, Dover, New York, 1996.

(129) E. Schrödinger, *Ann. Phy.*, 1926, **79**, 361–376.

(130) D. R. Hartree, *Math. Proc. Camb. Philos. Soc.*, 1928, **24**, 89–132.

(131) V. Fock, *Z. Phys.*, 1930, **61**, 126–148.

(132) C. C. J. Roothaan, *Rev. Mod. Phys.*, 1951, **23**, 69–89.

(133) C. A. Coulson and A. H. Neilson, *Proc. Phys. Soc.*, 1961, **78**, 831–837.

(134) J. Čížek, *J. Chem. Phys.*, 1966, **45**, 4256–4266.

(135) E. Schrödinger, *Ann. Phys.*, 1926, **80**, 437–490.

(136) C. Møller and M. S. Plesset, *Phys. Rev.*, 1934, **46**, 618–622.

(137) B. O. Roos, *Lecture Notes in Chemistry volume 58: Lecture Notes in Quantum Chemistry. European Summer School in Quantum Chemistry*, Springer-Verlag, Berlin, 1992.

(138) K. Adersson, P. Malmqvist and B. O. Roos, *J. Chem. Phys.*, 1992, **96**, 1218–1226.

(139) P. Hohenberg and W. Kohn, *Phys. Rev.*, 1964, **136**, B864–B871.

(140) L. H. Thomas, *Proc. Camb. Phil. Soc.*, 1927, **23**, 542–548.

(141) E. Fermi, *Rend. Accad. Naz. Lincei*, 1927, **6**, 602–607.

(142) J. C. Slater, *Phys. Rev.*, 1951, **81**, 385–390.

(143) F. Bloch, *Z. Phys.*, 1929, **57**, 545–555.

(144) P. A. M. Dirac, *Proc. Camb. Phil. Soc.*, 1930, **26**, 376–385.

(145) W. Kohn and L. J. Sham, *Phys. Rev.*, 1965, **140**, A1133–A1138.

(146) A. D. Becke, *Phys. Rev. A*, 1988, **38**, 3098–3100.

(147) G. J. Laming, V. Termath and N. C. Handy, *J. Chem. Phys.*, 1993, **99**, 8765–8773.

(148) N. C. Handy and A. J. Cohen, *Mol. Phys.*, 2001, **99**, 403–412.

(149) J. P. Perdew, K. Burke and M. Ernzerhof, *Phys. Rev. Lett.*, 1996, **77**, 3865–3868.

(150) J. P. Perdew, *Phys. Rev. B*, 1986, **23**, 8822–8824.

(151) J. P. Perdew and Y. Wang, *Phys. Rev. B*, 1992, **45**, 13244–13249.

(152) C. Lee, W. Yang and R. G. Parr, *Phys. Rev. B: Condens. Matter*, 1988, **37**, 785–789.

(153) A. D. Becke, *J. Chem. Phys*, 1993, **98**, 5648–5652.

(154) P. J. Stephens, F. J. Devlin, C. F. Chabalowski and M. J. Frisch, *J. Phys. Chem.*, 1994, **98**, 11623–11627.

(155) J. C. Slater, *Phys. Rev.*, 1930, **36**, 57–64.

(156) S. F. Boys, *Proc. Roy. Soc. London A*, 1950, **200**, 542–554.

(157) F. Bloch, *Z. Phys.*, 1928, **52**, 555–600.

(158) P. E. Blöchl, *Phys. Rev. B*, 1994, **50**, 17953–17979.

(159) G. Te Velde, F. M. Bickelhaupt, E. J. Baerends, C. Fonseca Guerra, S. J. A. Van Gisbergen, J. G. Snijders and T. Ziegler, *J. Comput. Chem.*, 2001, **22**, 931–967.

(160) C. Fonseca Guerra, J. G. Snijders, G. Te Velde and E. J. Baerends, *Theor. Chem. Acc.*, 1998, **99**, 391–403.

(161) E. J. Baerends, T. Ziegler, A. J. Atkins and et al., *ADF2013, SCM, Theoretical Chemistry, Vrije Universiteit, Amsterdam, The Netherlands, https://www.scm.com*.

(162) E. Van Lenthe and E. J. Baerends, *J. Comput. Chem.*, 2003, **24**, 1142–1156.

(163) L. Versluis and T. Ziegler, *J. Chem. Phys.*, 1988, **88**, 322–328.

(164) E. Van Lenthe, E. J. Baerends and J. G. Snijders, *J. Chem. Phys.*, 1993, **99**, 4597–4610.

(165) E. Van Lenthe, E. J. Baerends and J. G. Snijders, *J. Chem. Phys.*, 1994, **101**, 9783–9792.

(166) E. Van Lenthe, J. G. Snijders and E. J. Baerends, *J. Chem. Phys.*, 1996, **105**, 6505–6516.

(167) E. Van Lenthe, R. Van Leeuwen, E. J. Baerends and J. G. Snijders, *Int. J. Quantum Chem.*, 1996, **57**, 281–293.

(168) E. Van Lenthe, A. Ehlers and E. J. Baerends, *J. Chem. Phys.*, 0110, **110**, 8943–8953.

(169) A. Klamt and G. Schüürmann, *J. Chem. Soc. Perkin Trans. 2*, 1993, 799–805.

(170) A. Klamt, *J. Phys. Chem.*, 1995, **99**, 2224–2235.

(171) A. Klamt and V. Jonas, *J. Chem. Phys.*, 1996, **105**, 9972–9981.

(172) C. C. Pye and T. Ziegler, *Theor. Chem. Acc.*, 1999, **101**, 396–408.

(173) F. Neese, *Wiley Interdiscip. Rev.: Comput. Mol. Sci.*, 2012, **2**, 73–78.

(174) F. Pavošević, F. Neese and E. F. Valeev, *J. Chem. Phys.*, 2014, **141**, 054106.

(175) D. E. Woon and T. H. Dunning Jr., *J. Chem. Phys.*, 1993, **98**, 1358–1371.

(176) N. Balabanov and K. A. Peterson, *J. Chem. Phys.*, 2005, **123**, 064107.

(177) C. Riplinger and F. Neese, *J. Chem. Phys.*, 2013, **138**, 034106.

(178) C. Riplinger, P. Pinski, U. Becker, E. F. Valeev and F. Neese, *J. Chem. Phys.*, 2016, **144**, 024109.

(179) F. Neese, A. Hansen and D. G. Liakos, *J. Chem. Phys.*, 2009, **131**, 064103.

(180) F. Aquilante, J. Autschbach and et al., *J. Comput. Chem.*, 2016, **37**, 506–541.

(181) V. Veryazov, P. O. Widmark, L. Serrano-Andres, R. Lindh and B. O. Roos, *Int. J. Quantum Chem.*, 2004, **100**, 626–635.

(182) B. O. Roos, R. Lindh, P. Å. Malmqvist, V. Veryazov and P. O. Widmark, *J. Phys. Chem. A*, 2004, **108**, 2851–2858.

(183) B. O. Roos, R. Lindh, P. Å. Malmqvist, V. Veryazov and P. O. Widmark, *J. Phys. Chem. A*, 2005, **109**, 6575–6579.

(184) V. Arcisauskaite, D. Fijan, M. Spivak, C. de Graaf and J. E. McGrady, *Phys. Chem. Chem. Phys.*, 2016, **18**, 24006–24014.

(185) R. O. Jones and G. Seifert, *Phys. Rev. Lett.*, 1997, **79**, 443–446.

(186) M. Häser, U. Schneider and R. Ahlrichs, *J. Am. Chem. Soc.*, 1992, **114**, 9551–9559.

(187) P. von Ragué Schleyer, K. Najafian and A. M. Mebel, *Inorg. Chem.*, 1998, **37**, 6765–6772.

(188) R. B. King, I. Silaghi-Dumitrescu and M. M. Uţă, *Eur. J. Inorg. Chem.*, 2008, **2008**, 3996–4003.

(189) S. Zhao, Z. H. Li, W. N. Wang, Z. P. Liu, K. N. Fan, Y. M. Xie and H. F. Schaefer III, *J. Chem. Phys.*, 2006, **124**, 184102.

(190) S. Kurth, J. P. Perdew and P. Blaha, *Int. J. Quantum Chem.*, 1999, **75**, 889–909.

(191) D. A. Pantazis, J. E. McGrady, F. Maseras and M. Etienne, *J. Chem. Theory Comput.*, 2007, **3**, 1329–1336.

(192) F. Y. Li, P. Jin, D. E. Jiang, L. Wang, S. B. Zhang, J. J. Zhao and Z. F. Chen, *J. Chem. Phys.*, 2012, **136**, 074302.

(193) W. Y. Jiang, N. J. DeYonker and A. K. Wilson, *J. Chem. Theory Comput.*, 2012, **8**, 460–468.

(194) J. N. Harvey, *J. Biol. Inorg. Chem.*, 2011, **16**, 831–839.

(195) I. W. Bulik, T. M. Henderson and G. E. Scuseria, *J. Chem. Theory Comput.*, 2015, **11**, 3171–3179.

(196) V. T. Ngan, K. Pierloot and M. T. Nguyen, *Phys. Chem. Chem. Phys.*, 2013, **15**, 5493–5498.

(197) C. J. Cramer, M. Włoch, P. Piecuch, C. Puzzarini and L. Gagliardi, *J. Phys. Chem. A*, 2006, **110**, 1991–2004.

(198) P. Å. Malmqvist, K. Pierloot, A. Rehaman, M. Shahi, C. J. Cramer and L. Gagliardi, *J. Chem. Phys.*, 2008, **128**, 204109.

(199) X. Jin, V. Arcisauskaite and J. E. McGrady, *Dalton Trans.*, 2017, **46**, 11636–11644.

(200) T. Miyazaki, H. Hiura and T. Kanayama, *Eur. Phys. J. D*, 2003, **24**, 241–244.

(201) A. N. Andriotis, G. Mpourmpakis, G. E. Froudakis and M. Menon, *New J. Phys.*, 2002, **4**, 78.

(202) G. Mpourmpakis, G. E. Froudakis, A. N. Andriotis and M. Menon, *J. Chem. Phys.*, 2003, **119**, 7498–7502.

(203) A. K. Singh, V. Kumar and Y. Kawazoe, *Eur. Phys. J. D*, 2005, **34**, 295–298.

(204) R. Robles and S. N. Khanna, *Phys. Rev. B*, 2009, **80**, 115414.

(205) T. Iwasa and A. Nakajima, *J. Phys. Chem. C*, 2012, **116**, 14071–14077.

(206) W. X. Ji and C. L. Luo, *Int. J. Quantum Chem.*, 2012, **112**, 2525–2531.

(207) X. M. Huang, X. H. -G., S. J. Lu, Y. Su, R. B. King, J. J. Zhao and W. J. Zheng, *Nanoscale*, 2014, **6**, 14617–14621.

(208) J. Wang and J. H. Liu, *J. Comput. Chem.*, 2008, **30**, 1103–1110.

(209) J. G. Han, R. N. Zhao and Y. H. Duan, *J. Phys. Chem. A*, 2007, **111**, 2148–2155.

(210) R. N. Zhao, J. G. Han and Y. H. Duan, *Thin Solid Films*, 2014, **556**, 571–579.

(211) R. N. Zhao, R. Chen, Z. C. Lu and J. G. Han, *Mater. Sci. Eng. B*, 2017, **226**, 151–157.

(212) A. A. Saranin, A. V. Zotov, V. G. Kotlyar, T. V. Kasyanova, O. A. Utas, H. Okado, M. Katayama and K. Oura, *Nano Lett.*, 2004, **4**, 1469–1473.

(213) A. K. Singh, V. Kumar, T. M. Briere and Y. Kawazoe, *Nano Lett.*, 2002, **2**, 1243–1248.

(214) A. A. Shvartsburg, B. Liu, Z. Y. Lu, C. Z. Wang, M. F. Jarrold and K. M. Ho, *Phys. Rev. Lett.*, 1999, **83**, 2167–2170.

(215) E. D. Jemmis, M. M. Balakrishnarajan and P. D. Pancharatna, *J. Am. Chem. Soc.*, 2001, **123**, 4313–4323.

(216) P. G. A. Leyva, E. M. Sosa-Hernández, J. M. Montejano-Carrizales and F. Aguilera-Granja, *Eur. Phys. J. D*, 2015, **69**, 51.

(217) C. Liu, L. J. Li, X. Jin, J. E. McGrady and Z. M. Sun, *Inorg. Chem.*, 2018, **57**, 3025–3034.

(218) J. Y. Cheng, B. L. Fisher, N. P. Guisinger and C. M. Lilley, *npj Quantum Materials*, 2017, **2**, 25.

(219) M. H. Tsai, J. D. Dow, P. A. Bennett and D. G. Cahill, *Phys. Rev. B*, 1993, **48**, 2486–2492.

(220) P. A. Bennett, M. Copel, D. Cahill, J. Falta and T. R. M., *Phys. Rev. Lett.*, 1992, **69**, 1224–1227.

(221) R. J. Wilson and S. Chiang, *Phys. Rev. Lett.*, 1987, **58**, 2575–2578.

(222) D. Haneman, *Phys. Rev.*, 1961, **121**, 1093–1100.

(223) K. C. Pandey, *Phys. Rev. Lett.*, 1981, **47**, 1913–1917.

(224) T. Rakshit, G. C. Liang, A. W. Ghosh and S. Datta, *Nano Lett.*, 2004, **4**, 1803–1807.

(225) G. Kresse and J. Furthmüller, *Phys. Rev. B*, 1996, **54**, 11169.

(226) G. Kresse and D. Joubert, *Phys. Rev.*, 1999, **59**, 1758–1775.

(227) J. P. Perdew and Y. Wang, *Phys. Rev. B*, 1986, **33**, 8800–8802.

(228) E. J. Baerends, T. Ziegler, A. J. Atkins and et al., *Atomistix Toolkit version 2016.4, Synopsys QuantumWise A/S, www.quantumwise.com*.

(229) M. Brandbyge, J. L. Mozos, P. Ordejón, J. Taylor and K. Stokbro, *Phys. Rev. B*, 2002, **65**, 165401.

(230) D. Stradi, U. Martinez, A. Blom, M. Brandbyge and K. Stokbro, *Phys. Rev. B*, 2016, **93**, 155302.

(231) S. Smidstrup, D. Stradi, J. Wellendorff, P. A. Khomyakov, U. G. Vej-Hansen, M. E. Lee, T. Ghosh, E. Jónsson, H. Jónsson and K. Stokbro, *Phys. Rev. B*, 2017, **96**, 195309.

(232) R. E. Schlier and H. E. Farnsworth, *J. Chem. Phys.*, 1959, **30**, 917–926.

(233) V. Y. Aristov, I. E. Batov and V. A. Grazhulis, *Surf. Sci.*, 1983, **132**, 73–81.

(234) D. Haneman, *Adv. Phys.*, 1982, **31**, 165–194.

(235) R. I. G. Uhrberg, G. V. Hansson, J. M. Nicholls and S. A. Flodström, *Phys. Rev. B*, 1981, **24**, 4684–4691.

(236) F. Houzay, G. M. Guichar, R. Pinchaux and Y. Petroff, *J. Vac. Sci. Technol.*, 1981, **18**, 860–865.

(237) S. Brennan, J. Stohr, R. Jaeger and J. E. Rowe, *Phys. Rev. Lett.*, 1980, **45**, 1414–1418.

(238) J. E. Northrup and M. L. Cohen, *Phys. Rev. Lett.*, 1982, **49**, 1349–1352.

(239) F. J. Himpsel, P. M. Marcus, R. Tromp and I. P. Batra, *Phys. Rev. B*, 1984, **30**, 2257–2259.

(240) R. M. Feenstra, W. A. Thompson and A. P. Fein, *Phys. Rev. Lett.*, 1986, **56**, 608–611.

(241) R. M. Feenstra, J. A. Stroscio and A. P. Fein, *Surf. Sci.*, 1987, **181**, 295–306.

(242) D. Haneman, *Rep. Prog. Phys.*, 1987, **50**, 1045–1086.

(243) G. Xu, B. C. Deng, Z. X. Yu, S. Y. Tong, M. A. van Hove, F. Jona and I. Zasada, *Phys. Rev. B*, 2004, **70**, 045307.

(244) J. J. Lander, G. W. Gobeli and J. Morrison, *J. Appl. Phys.*, 1963, **34**, 2298–2306.

(245) R. M. Feenstra and M. A. Lutz, *Surf. Sci.*, 1991, **243**, 151–165.

(246) K. Takayanagi, Y. Tanishiro, M. Takahashi and S. Takahashi, *J. Vac. Sci. Technol. A*, 1985, **3**, 1502–1506.

(247) J. M. Ricart, J. Rubio and F. Illas, *Phys. Rev. B*, 1990, **42**, 5212–5219.

(248) S. Datta, *Quantum Transport: Atom to Transistor*, Cambridge University Press, Cambridge, 2005.

List of Publications

The submitted version of the papers that have been published during my DPhil study at University of Oxford are listed and attached here.

- X. Jin, G. Espinoza-Quintero, B. Below, V. Arcisauskaite, J. M. Goicoechea and J. E. McGrady, *J. Organomet. Chem.*, 2015, **792**, 149-153.
- V. Arcisauskaite, X. Jin, J. M. Goicoechea and J. E. McGrady, in *Chemical Bond I: 100 Years Old and Getting Stronger*, ed. D. M. P. Mingos, Springer, New York, 2016, vol. 169, pp. 181–197.
- X. Jin, V. Arcisauskaite and J. E. McGrady, *Dalton Trans.*, 2017, **46**, 11636-11644.
- C. Liu, L. -J. Li, X. Jin, V. Arcisauskaite, J. E. McGrady and Z. -M. Sun, *Inorg. Chem.*, 2018, **57**, 3025-3034.